

**3D TEXTILE PMC DAMAGE EVOLUTION:
EFFECTS OF FIBER VOLUME FRACTION
AND MORPHOLOGY VARIATION**

Thesis

Submitted to

The School of Engineering of the
UNIVERSITY OF DAYTON

In Partial Fulfillment of the Requirements for

The Degree of
Master of Science in Mechanical Engineering

By

Solomon George Duning

UNIVERSITY OF DAYTON

Dayton, Ohio

May, 2016

**3D TEXTILE PMC DAMAGE EVOLUTION:
EFFECTS OF FIBER VOLUME FRACTION AND MORPHOLOGY VARIATION**

Name: Duning, Solomon George

APPROVED BY:

Margaret Pinnell, Ph.D.
Advisor Committee Chairman
Professor, Department of Mechanical
and Aerospace Engineering

David Mollenhauer, Ph.D.
Committee Member
Senior Materials Engineer, Air Force
Research Laboratory / RXCC

Tom Whitney, Ph.D., P.E.
Committee Member
Associate Professor, Department of Civil
and Environmental Engineering and
Engineering Mechanics

John G. Weber, Ph.D.
Associate Dean
School of Engineering

Eddy M. Rojas, Ph.D., M.A., P.E.
Dean, School of Engineering

© Copyright by

Solomon George Duning

All rights reserved

2016

ABSTRACT

3D TEXTILE PMC DAMAGE EVOLUTION: EFFECTS OF FIBER VOLUME FRACTION AND MORPHOLOGY VARIATION

Name: Duning, Solomon George
University of Dayton

Advisor: Dr. Margaret Pinnell

3D textile polymer matrix composites (PMC) exhibit geometric and material state variances due to differences in manufacturing processes and a variety of other factors. Developing a more thorough understanding of these strength and damage variations is a vital aspect of generating an accurate predictive model for the material response of a 3D textile PMC. This work entails both experimental and modeling efforts in order to gain a more thorough understanding of how tow level geometric variations relate to damage evolution in a 3D textile PMC. A 3D orthogonal weave textile is imaged utilizing an X-Ray micro-CT to examine the fiber volume fraction and fiber path distributions within the composite. Additionally, damage evolution is observed at different load steps and CT images are utilized for Digital Volume Correlation analysis. Modeling efforts are primarily focused on tow morphology simulations within the software package—Virtual Textile Morphology Suite (VTMS). Damage evolution analysis on the VTMS models are performed using an advanced Regularized eXtended Finite Element Method (RX-FEM) within the Air Force Research Laboratory developed B-Spline Analysis Method (BSAM) program. Local fiber volume fraction variation in the

specimens is examined through serially sectioned images obtained using Robo-Met 3D. Fiber volume fraction distributions are compared to VTMS predictions and VTMS predictions are modified to reflect experimental values. The effect of these local fiber volume fraction distributions on damage evolution in the composite are examined through experimentation and modeling efforts.

For my friends, family, and loved ones who have always supported me and all of my endeavors.

Thank you

ACKNOWLEDGMENTS

Thank you to all of those at AFRL/RXCC and the University of Dayton who have helped me and taught me so much throughout these past few years. In particular, I would like to give a special thank you to the following:

- Misha Braginsky
- Stephen Bricker
- John Camping
- Mark Flores
- Kevin Hoos
- Endel Iarve
- David Mollenhauer
- Brenna Nowacki
- Margaret Pinnell
- Craig Przybyla
- Bill Ragland
- Dan Rapking
- Art Safriet
- Sirina Safriet
- James Sands
- Paul Sinz
- Mike Uchic
- Eric Zhou

TABLE OF CONTENTS

ABSTRACT	iii
DEDICATION	v
ACKNOWLEDGMENTS	vi
LIST OF FIGURES	x
 I. BACKGROUND	1
1.1 Composites Overview	1
1.2 3D Textile Polymer Matrix Composites	2
1.3 Laminate Elastic Property and Volume Fraction Relations	4
1.4 Textile Modeling Methods	9
 II. BACKGROUND OF MODELS AND SOFTWARE USED IN STUDY	14
2.1 Multi-Chain Digital Element Analysis	14
2.2 The Independent Mesh Method	17
2.3 Expectation Maximization of the Maximization of Posterior Marginals	20
2.4 Hough Transform Feature Extraction	22
 III. EXPERIMENTAL METHODS	23
3.1 Specimen Fabrication	23
3.2 Micro-CT Imaging	25
3.3 Digital Volume Correlation	29
 IV. INITIAL SERIAL SECTIONING AND ANALYSIS METHODOLOGY DEVELOPMENT	31
4.1 Serial Sectioning Introduction	31
4.2 Preliminary Serial Sectioning of 3D Textile PMC Specimen	32

4.3	Image Fiber Volume Fraction Extraction	32
4.4	Binary Image Fiber Volume Fraction- Methodology	34
4.5	Binary Image Fiber Volume Fraction- Experimental	35
4.6	Individual Tow Cropping- Methodology	36
4.7	Binder Region Fiber Volume Extraction	38
4.8	Binary Image Fiber Volume Fraction Methodology Accuracy	41
V.	FINAL SERIAL SECTIONING	45
5.1	Sectioning Angle and Segmentation Considerations	45
5.2	Specimen Preparation	46
5.3	Resolution Determination and Segmentation Parameterization	49
5.4	Image Analysis and Preparation	53
VI.	VTMS METHODOLOGY	57
6.1	Textile Module	57
6.2	Relaxation Module- General Features	62
6.3	Relaxation Module- Orthogonal Weave Preform Generation	66
6.4	Tow Modification Module	68
6.5	Mesh Generator Module	71
6.6	BSAM Export Module	75
VII.	FIBER VOLUME FRACTION METHODS	78
7.1	Local Fiber Volume Fraction- VTMS Approach	78
7.2	Manchester Study	83
7.3	Direct Image to Model Relation Method	87
7.4	Hierarchical Weibull Fit Redistribution Method	89
VIII.	RESULTS AND DISCUSSION	93
8.1	Digital Volume Correlation Results	93
8.2	BSAM Tensile Test Results	97
8.3	Fiber Volume Fraction Distribution Tests	100
IX.	RECOMMENDATIONS AND CONCLUDING REMARKS	108
9.1	Recommended Research Plan	108
9.2	Conclusion	111
	BIBLIOGRAPHY	113

APPENDICES	117
A. Fiber Volume Fraction Tow Extraction	118
B. Fiber Volume Fraction Variation Map	121
C. Image Tow Cropper	123
D. Hierarchical Weibull Fit VTMS Redistribution	125

LIST OF FIGURES

1.1	Flowchart of Typical Composite Categories	2
1.2	Voigt Model of a Longitudinally Loaded Composite Laminate RVE	4
1.3	Reuss Model of a Transversely Loaded Composite Laminate RVE	5
1.4	Parallel-Series Model of a Transversely Loaded Composite Laminate RVE	7
1.5	Cross-Sectional Region of a Serially Sectioned 3D Textile PMC	8
3.1	3D Orthogonal Weave Textile Preform Utilized in Study	24
3.2	Technical Drawing of Waterjet Cut Dog-Bone Specimens	25
3.3	Example of a Final Waterjet Cut Dog-Bone Specimen	26
3.4	Three Dimensional Imaging of Dog-Bone Specimen Gage Section	27
3.5	Imaged Binders of Dog-Bone Specimen Gage Section	27
3.6	Micro-CT Image of Cross-Section at the Centerline of Specimen	28
3.7	Cross-Section from Micro-CT Imaging of Dog-Bone Specimen	29
4.1	Image Slice of Specimen from Robo-Met Serial Sectioning	33
4.2	Fiber Identification in a Segmented Image Using the Hough Transform Method . .	34
4.3	Binary Black and White Thresholded Image of Serial Section Slice	36
4.4	Fiber Volume Fraction Intensity Map for 100x100 Pixel Window Size	37

4.5	Tow Geometry Cropped from Original Serially Sectioned Image	38
4.6	Histogram and Gaussian Plot of Image of Binder Region	39
4.7	Segmentation of Binder Region	40
4.8	Accuracy of Binary Image Fiber Volume Fraction Methodology- Image Set 1 . . .	42
4.9	Accuracy of Binary Image Fiber Volume Fraction Methodology- Image Set 2 . . .	43
5.1	Specimen and Plug Mold for Serial Sectioning	47
5.2	Specimen and Guide Fixture for Diamond Saw Cutting	48
5.3	Plug Utilized for Serial Sectioning	48
5.4	High and Low Resolution Comparison	49
5.5	High and Low Resolution Comparison- Segmented Images	50
5.6	High and Low Resolution Comparison- Segmented Pixel Level Zoom	51
5.7	Segmented and Raw Image Overlay Comparison	52
5.8	High Resolution Cross-Section of Second Specimen	54
5.9	Seriously Sectioned Image Superimposed on Micro-CT Image	54
5.10	Fiber Makeup of Weft Tows	55
6.1	Fabric Parameters- VTMS Input	58
6.2	Specimen Preform Model with Idealized Tows	58
6.3	Scaled and Tessellated Preform Model	59
6.4	Digital Fiber Geometry and Packing Scheme	61
6.5	Idealized and Fiberized Tow Cross-Sections	63
6.6	Preform Model with Fiberized Tows	64

6.7	Depiction of a Mold Utilized in the Relaxation Module	66
6.8	Fully Relaxed Textile Preform Model	67
6.9	Relaxed Preform Cut to Size of the Dog-bone Specimen Gage Section	68
6.10	Regular Binder Tow Before and After Smoothing Application	69
6.11	Regions of Interpenetration Between Tows	70
6.12	Regular Tow Surface Mesh Model of Fabric Preform	71
6.13	Clipped Tow Surface Mesh Model of Fabric Preform	72
6.14	C3D8 Element Example	72
6.15	Swept Weft Tow and Corresponding Sweeping Plane	73
6.16	Regular vs. Clipped Binder Tow	74
6.17	Three Dimensional Meshes Used in the Fabric Preform Model	75
6.18	Composite Matrix Mesh of the Dog-bone Specimen	76
7.1	VTMS Fiber Volume Fraction Approximation Element Discretization	79
7.2	Local Element Fiber Volume Fraction of Binder Tows- VTMS Approach	80
7.3	Error in Tow Surface Area VTMS Approximation	81
7.4	Binder Tow Finite Element Mesh and Corresponding Fiber	81
7.5	Re-Sampling of Binder Fiber Volume Fraction	83
7.6	Compacted Carbon Fiber Plain Weave Pre-Form	84
7.7	Original VTMS Model of Plain Weave Compacted Preform	84
7.8	VTMS Model of Manchester Plain Weave Compacted Preform	86
7.9	VTMS Model Compared to Micro-CT Results	86

7.10	Direct Image to Model Fiber Volume Fraction Relation	88
7.11	Image Sampling to Model Coordinate System Transformation Error	89
7.12	VTMS FVF Approximation Based on Experimental Weibull Parameters	91
8.1	DVC- <i>w</i> Displacement Superimposed on Corresponding Image Slice	94
8.2	DVC- <i>u</i> Displacement	95
8.3	DVC- <i>v</i> Displacement	95
8.4	DVC- <i>w</i> Displacement	96
8.5	DVC- Stress	96
8.6	BSAM Tensile Test- Warp Direction Displacement	98
8.7	BSAM Tensile Test- Warp Direction Strain	99
8.8	BSAM Tensile Test- Warp Direction Stress	99
8.9	Image Slice Utilized for Distribution Tests	101
8.10	Tow 2- Cropped Tow and Fiber Volume Fraction Variation Histogram	102
8.11	Tow 2- Probability Plots for Common Distributions	103
8.12	Weibull Probability Plots for Tows 1, 3, 4, 5, 6, and 7	104
8.13	Weibull Probability Plots for Tows 1 and 3- Adjusted for Edge Effects	105
8.14	FVF Tows 1-7: Parameterized Weibull Distribution	106
9.1	Batch Cropped and Segmented Tow	109

CHAPTER I

BACKGROUND

1.1 Composites Overview

A composite material is any material in which two or more materials are combined on a macroscopic scale to form a useful material [1]. Composite materials are typically broken down into three main categories:

- **Fibrous Composites**- a material consisting of fiber reinforcements in a matrix
- **Laminated Composites**- a material consisting of layers of multiple materials
- **Particulate Composites**- a material consisting of particulate reinforcements in a matrix

A flowchart containing most of the different categories of composites is shown in Figure 1.1.

Composite materials have been utilized for centuries [2], but have only fairly recently been utilized in advanced material applications [3], [4], [5]. In particular, fiber-reinforced composite materials have shown increased use in the aerospace industry due to their high strength-to-weight ratio and stiffness properties.

Due to the microscopically heterogeneous and macroscopically homogeneous nature of composite materials, analysis of composites can be approached from both a micromechanics and macromechanics perspective [6]. Micromechanics is the study of material behavior where the interaction of constituent materials is examined on a microscopic scale. Conversely, macromechanics models the composite material as homogeneous and examines the material behavior where the effects of the

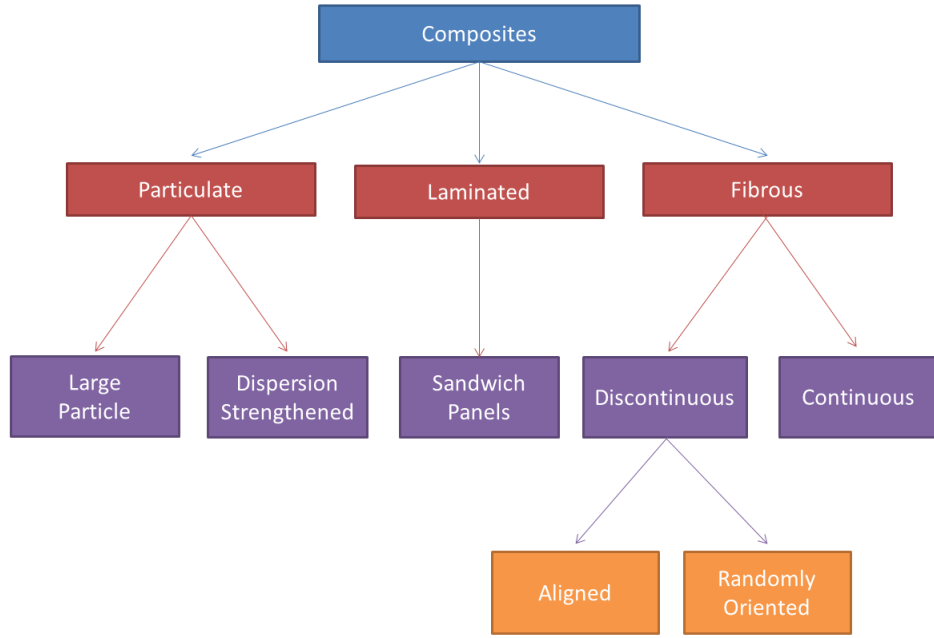


Figure 1.1: Flowchart of Typical Composite Categories

constituent materials are simply averaged properties. In general, macromechanics is utilized in the design of the composite structure, while micromechanics is utilized in the design of the material itself. For advanced applications such as in the aerospace industry, micromechanical models are vital to understanding material failure. In recent years, it has become increasingly apparent that discrete damage characterization is necessary for predicting and understanding material failure [7], [8].

1.2 3D Textile Polymer Matrix Composites

Polymer Matrix Composites (PMC) have shown increased use in advanced structures over recent years [9]. PMCs with a textile fiber architecture have been of particular interest due to their lower manufacturing costs, improved impact resistance, and drapeability. In industry, textile architectures typically consist of two dimensional fabric weaves; however, recently, the structures community has been focusing on the use of three dimensional fabric textile architectures. These 3D textiles exhibit

binding tows that are woven through the thickness of the weave. These tows bind the layers of the fabric together, therefore increasing their through thickness properties [10].

Geometry and fiber variations are induced in textiles due to a variety of manufacturing processes. Textiles are compacted by vacuum bags, platens, or rigid molds which creates localized areas of higher pressure. This compaction varies the geometry of the tows and can only be accounted for if the processes are somehow modeled explicitly. Most models do not consider the manufacturing processes utilized to create the composite, or simply utilize empirical data for their geometric description. Variation is further impacted by randomized nesting of 2D weave layers and human handling of the textile preforms.

Research regarding the effects on material properties of fiber volume fraction variation throughout three dimensional textiles is considerably limited. Most of the research pertaining to this issue has been performed on unidirectional laminates [11]. These studies suggest that fiber volume fraction variations have a significant effect on damage evolution in the material. Considering the variation inherent to 3D textiles, a comprehensive study on the effects of this variation on the mechanical response of 3D textiles is a worthwhile pursuit. Furthermore, a recent study on 3D polymer matrix textiles revealed that a higher variation exists in 3D textiles at the tow-geometry scale than at the fabric level scale [12]. That is, there is a higher variation in fiber volume from one tow to another as opposed to examining complete sections of fabric. The study however, does not address inter-tow variability; in other words, the local variation of fiber volume within the tow itself.

In another study, researchers examined the effects of tow shape and local fiber direction in 3D braided PMC textiles [13]. In general, the study concluded that the unidirectional tensile strengths of 3D four-directional braided composites decrease with an increase in the angle of twist of the braid yarn. This showed that the morphology of the tow or braid has a significant effect on the strength

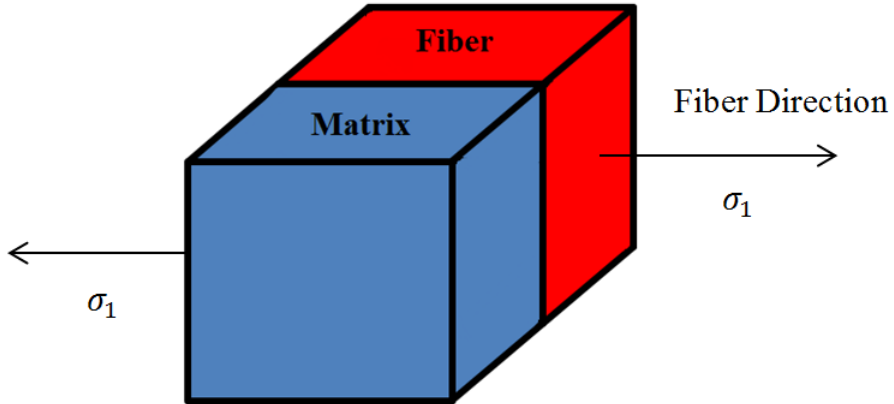


Figure 1.2: Voigt Model of a Longitudinally Loaded Composite Laminate RVE

properties of the composite. In addition, the researchers concluded that the inclusion of fiber volume in their model led to significant effects on the predicted composite stiffness and strength.

1.3 Laminate Elastic Property and Volume Fraction Relations

It is well-known that fiber volume fraction plays a significant role in determining the elastic properties of the overall composite [14], [15], [16]. Models however, relating fiber volume fraction to elastic properties typically only pertain to laminate composites since their fiber orientations are generally known. However, it is valuable to understand these laminate models before investigating how elastic properties may relate to volume fraction in composites with textile fabric architectures. The most common and simple formulation for determining the elastic modulus in the direction of the fibers is the rule of mixtures. Consider the simple representative volume element of a composite laminate shown in Figure 1.2. This model is typically referred to as the Voigt model. Utilizing the Voigt model, one can assume that the strain in the fibers and in the matrix are equal. With this assumption and neglecting Poisson effects, the rule of mixtures is obtained:

$$E_1 = V_f E_f + E_m V_m \quad (1.1)$$

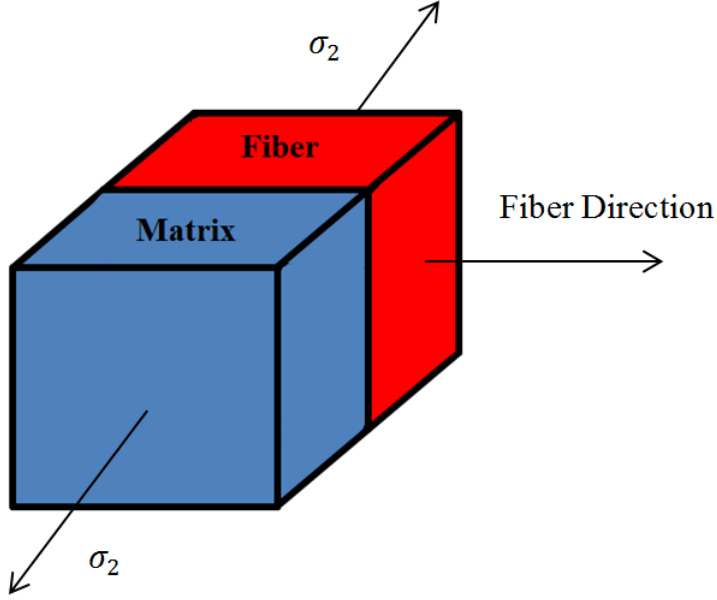


Figure 1.3: Reuss Model of a Transversely Loaded Composite Laminate RVE

where E_1 is the elastic modulus of the lamina, V_f is the fiber volume fraction of the lamina and E_f and E_m are the Young's moduli for the fibers and the matrix material, respectively [17]. The rule of mixtures is also commonly written as:

$$E_1 = V_f E_f + (1 - V_f) E_m \quad (1.2)$$

Surprisingly, this simple formulation has shown great success in accurately predicting the E_1 modulus for composite laminates [18]. In general, no modifications to the rule of mixtures are necessary to obtain an accurate E_1 modulus prediction in laminates.

However, for the determination of the Apparent Young's modulus, the elastic modulus in the direction transverse to the fibers or E_2 , there is no universally accepted formulation. Consider a transversely loaded RVE of a composite laminate with a series orientation between fiber and matrix. This model is referred to as the Reuss Model and is shown in Figure 1.3. Using the Reuss model to solve for the E_2 modulus, it is assumed that the same transverse stress is applied to both the fiber

and the matrix. With some simple algebraic manipulations, the obtained transverse elastic modulus is:

$$E_2 = \frac{E_{f2}E_m}{V_m E_{f2} + V_f E_m} \quad (1.3)$$

where E_{f2} is the transverse elastic modulus of the fibers (note that the matrix is assumed isotropic), and the other symbol definitions are the same as the rule of mixtures [17]. It is also frequently written in another form as:

$$\frac{1}{E_2} = \frac{v_m}{E_m} + \frac{v_f}{E_{f2}} \quad (1.4)$$

This formulation is also known as a component of the rule of mixtures (sometimes it is referred to as the inverse rule of mixtures), but is not as universally utilized as the E_1 formulation and is generally not suitable for design purposes [17]. It is primarily inaccurate due to the underlying assumption that there is equality of stress in the matrix and the fiber; in addition, this formulation also ignores the contribution of the fiber matrix interface to the material properties. Furthermore, the transverse modulus of the fibers can be difficult to accurately measure which will ultimately lead to varying results depending upon the measurement technique.

The Reuss model can be improved by simply adding a matrix volume parallel to the Reuss series model. This parallel-series model is shown in Figure 1.4. Adding this additional matrix volume increases the complexity of the model but more accurately predicts behavior. Using a square approximation of fiber packing, a more accurate equation for predicting the transverse elastic modulus can be obtained [19].

$$E_2 = (1 - \sqrt{v_f})E_m + \frac{\sqrt{v_f}E_mE_{f2}}{v_fE_m + \sqrt{v_f}(1 - \sqrt{v_f})E_{f2}} \quad (1.5)$$

A widely utilized formulation for the transverse elastic modulus is a modified rule of mixtures relation developed by Tsai and Hahn [20]. This modified equation utilizes the stress partitioning

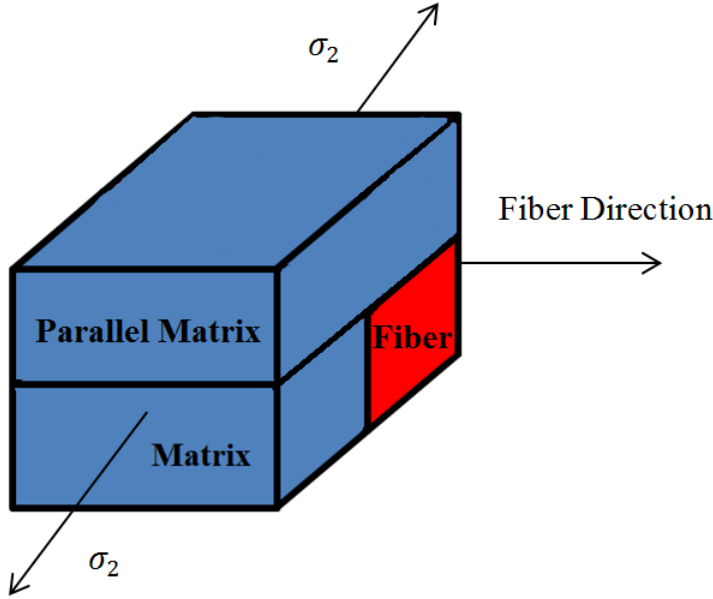


Figure 1.4: Parallel-Series Model of a Transversely Loaded Composite Laminate RVE

parameter- η , or the ratio of the average matrix to average fiber stresses.

$$\frac{1}{E_2} = \frac{1}{v_f + \eta * v_m} \left[\frac{v_f}{E_{f2}} + \frac{\eta * v_m}{E_m} \right] \quad (1.6)$$

As can be seen from Equation 1.6, when $\eta = 1$ then the Tsai Hahn equation is equivalent to the inverse rule of mixtures. By introducing the stress partitioning parameter, this semi-empirical equation attempts to take into account the difference in stress between the fiber and matrix.

The in-plane shear modulus of a lamina, G_{12} , can also be calculated by the mechanics of materials approach if the shearing stresses on the fiber and the matrix are assumed to be the same [17]. Doing so ignores the typical nonlinear shear stress and shear strain behavior of fiber reinforced composites. The formulation utilizing this approach is written as:

$$G_{12} = \frac{G_f G_m}{V_m G_f + V_f G_m} \quad (1.7)$$

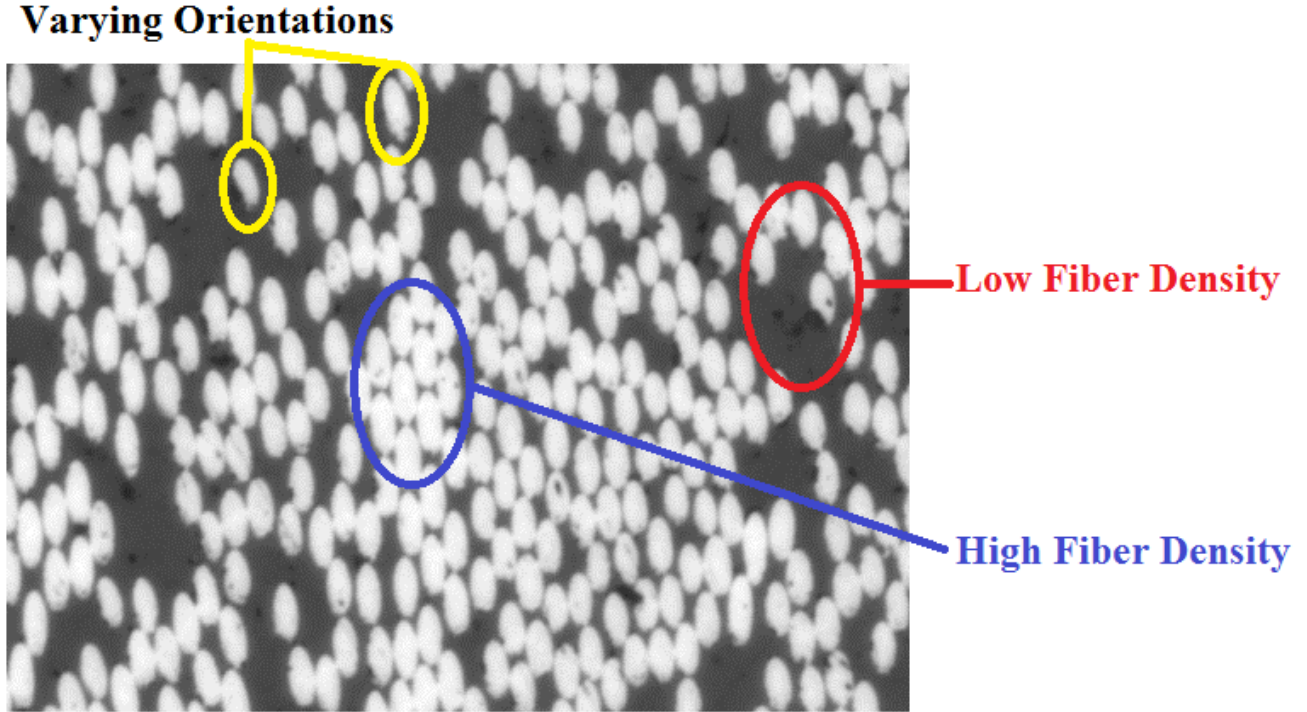


Figure 1.5: Cross-Sectional Region of a Serially Sectioned 3D Textile PMC

Equation 1.7 appears in the same form as the inverse rule of mixtures as can be seen in Equation 1.3. Under the same assumptions as the in-plane shear modulus, the Poisson's ratio can be obtained:

$$\nu_{12} = \nu_m v_m + \nu_f v_f \quad (1.8)$$

Although the equations presented provide an estimation of the relationship between the elastic modulus and fiber volume fraction for laminate composites, these relations are not typically utilized for textile composites. The difficulty in obtaining an elastic property and fiber volume relation for textile composites arises from the complex geometry of the architecture, the increased variability of fiber orientations, and inconsistent fiber volume fractions throughout the volume of the composite. For instance, consider Figure 1.5, a depiction of a small cross-section region in a serially sectioned 3D textile polymer matrix composite. In this image, the issues pertaining to the acquisition of a fiber volume and elastic property relation, as previously discussed, are readily apparent. The two

fibers highlighted in yellow show instances of fibers that have a different orientation than the rest of the fibers in the region. On average, these fibers may not drastically affect the properties; on a local basis however, these fibers could have a great effect on the properties of the local region. The region outlined with the red oval shows an area of low fiber volume fraction while the blue oval shows an area of high fiber volume fraction. These two regions will have drastically different elastic properties, despite the fact that they are relatively close in spatial proximity. Furthermore, Figure 1.5 represents a region of approximately 350 x 250 microns. Considering the relatively small area of the image, there is a very high degree of fiber variability. In addition, it is very difficult to predict where these extreme fiber volume fraction regions may occur within a textile composite, making it difficult to obtain an accurate fiber volume fraction and elastic property relation. Considering issues such as these, effective relations between fiber volume fraction and elastic properties in 3D polymer matrix composite textiles simply do not exist.

1.4 Textile Modeling Methods

The modeling of textiles is broken down into two distinct categories: the modeling of the morphology within the fabric weave and the prediction of stress and damage evolution of the overall composite. The modeling of morphology variation involves analyzing the various geometric changes that occur as the idealized fabric weave morphs from its original state to the final state that is observed in the composite architecture. In general, the design tools utilized in industry do not account for these variations within the weave architecture. The majority of these tools considers an idealized tow geometry and homogenize properties for large areas of the PMC. This methodology is suitable for an approximation of material stiffness for most simple textiles, but inadequate for general strength predictions and for textiles with complex architectures. Other academic modeling

programs are more advanced than the ones seen in industry, however most of these still only consider an idealized tow cross-section. In addition, these tools generally assume uniform properties within a tow which could drastically alter the property prediction of the overall composite.

One of the more advanced commercial and academic tools is WiseTex developed by Lomov et al [21]. In order to predict the compacted tow morphology, WisTex utilizes an analytical approach. WiseTex provides a description of the internal geometry of the fabric based on a relatively small set of input data consisting of:

- Geometry of the tow cross-section
- Tow spacing
- Overall fabric pattern
- Compression and bending properties
- Frictional and tensile behavior
- Fiber content

The shape of the tow is described using a parameterized function $z(x; h/p)$ where z and x are coordinates of the line going through the middle of the tow, h is the height of the crimp, and p is the tow spacing. Given these inputs, the function is calculated using the principal of minimum bending energy of the tow. The shape of the cross-section of the tow is assumed elliptical or lenticular. This cross-sectional shape doesn't change along the length of the tow; however, the dimensions or the shape can vary slightly based on contact zones between tows. In other words, this method assumes a constant cross-sectional shape and does not consider how tows can interact and elicit a change in the cross-sectional shape of neighboring tows. Furthermore, fiber volume calculations are assigned on a cross-sectional basis, not on an element by element basis. In addition, this calculation is only possible if the fibrous structure of the tows in their undeformed state is given. A separate tow micro-structural model must be developed in order to determine fiber volume fraction values for the tows in the fabric model. In some instances, it may be difficult to obtain an accurate tow micro-structure model which would lead to inaccuracies in the overall fabric model.

TexGen utilizes a numerical solution to model textile composites [22] [23] [24] [25]. With this method, tows are described using a centerline of the tow path and then a consistent cross-section is super imposed on this line. The shape and the size of the cross-sections change locally via a function for interference correction. These functions modify the textile geometry to avoid interpenetrations between fibers. As the cross-sections are modified, the fiber volume fraction within the tows are recalculated based on the new geometry of the corresponding cross-section. Automated routines are also used to discretize the model and to assign material orientations and properties to elements. Although this numerical technique is effective in generating a high fidelity model, it fails to take into account the independence of individual fibers within the tows. In other words, morphology variation may be inaccurate due to the fact that the tows are modeled as a singular entity instead of a collection of fibers.

These tools extract a two dimensional ideal cross-section along calculated tow paths. Neither tool has the ability to modify tow cross-sections based on interactions between tows. Furthermore, the packages assume uniform material properties for each cross-section in the finite element mesh. A significantly more advanced method, is the multi-chain digital element analysis technique developed by Zhou, Sun, and Wang [26]. This methodology was utilized during the course of the study and will be thoroughly discussed in Section 2.1.

Composite textiles provide a difficult challenge for most modeling software due to their complex architecture. Various methodologies to predict the stress and failure in these composites exist, but most fail to effectively model damage explicitly. For stress analysis and damage predictions, most methodologies focus on the use of the finite element method. While utilizing the finite element approach, properties are typically degraded as damage evolves in the material. The typical degradation of properties utilizes Continuum Damage Mechanics (CDM) principles. Although this

methodology can be utilized somewhat effectively as a stress predictor in composite materials, CDM methods fail to model damage explicitly [27].

There are two main categories of finite element methods utilized for composite materials: voxel methods and explicitly meshed methods. The voxel method generates a mesh of uniform finite elements that spans the entire fabric. Each individual voxel element is then assigned a material property: matrix, fiber (fiber directions are also assigned for these elements), or a mix of matrix and fiber properties [28] [29]. Since material definitions are assigned on a voxel element basis, the element size in the mesh must be significantly smaller than the features of the morphology. Because of the relatively small size of the elements, this method is very computationally intensive. However, voxel methods are generally unable to capture local interface details.

Explicitly meshed finite element methods mesh each tow independently and then fill in the remaining space with a matrix mesh. [30] [31]. For idealized fabric geometries, direct finite element discretization has proven to be an effective means of damage prediction [32]. Direct finite element discretization requires matching of adjacent element nodes and surfaces throughout the entire fabric model. Obtaining this is viable for an idealized fabric where tow paths and geometries are consistent throughout the entire model; but for a robust model that accounts for this variation, auto-meshing approaches fall drastically short in obtaining a usable model. The difficulty in this approach lies within the matching of surfaces and nodes of elements in a tow to the corresponding elements in the matrix or adjacent tows. Automatic meshing techniques simply cannot capture the complex geometries of matrix and tows while matching nodes of two separate entities.

Advanced methodologies have been developed to avoid the issues inherent to the voxel method and explicitly meshed methods. The binary model developed by Cox et al. in 1994 sought to find a simplistic methodology to model textile composites [33]. Firstly, the model discretized the tows as two-noded line elements with only axial rigidity. The tow elements did not include any shear

or bending resistance. Cox defines the matrix region as the effective medium and divides this into homogeneous and isotropic solid elements. Tows are then coupled to the effective medium via adjacent nodes; no two reinforcing tows are directly coupled. Essentially, the binary method effectively eliminates the geometrical complexity of the tow cross-sections by modeling them as two-noded rod line elements with a consistent cross-section. Doing this makes many material property calculations less cumbersome, but is too idealized to use to examine fiber volume fraction and morphology variations.

Another advanced methodology is the mesh superposition method developed by Hallett and Jiang [34] [35]. This methodology utilizes what is known as a Domain Superposition Technique (DST). Instead of modeling tows and resin pockets explicitly, the DST models the tow domain and the global domain. When meshing a composite, explicitly meshing the tows isn't as difficult as explicitly meshing the resin pocket spaces in between the tows. The DST avoids this by defining a global domain which is essentially an easily meshed rectangular prism. A negative matrix phase domain is meshed to subtract from the global domain and then the tow domain completely fills the spaces created. Coupling equations between the tow domain and the global domain are established to ensure that the coincident points between the two domains have the same displacement. Currently, there is an issue with the deformation field across the material phase boundaries which creates local error bands in these regions. This leads to a slightly higher prediction for macroscopic elastic moduli than is typically seen in finite element methods. Despite this issue, this method is one of the more effective methodologies available at this time.

The Independent Mesh Method develop by Larve et al [36] was the methodology utilized throughout this study. This method is a combination of both voxel and direct finite element meshing in that the fiber tows are discretized directly and independently. The IMM will be explained in greater detail in Section 2.2

CHAPTER II

BACKGROUND OF MODELS AND SOFTWARE USED IN STUDY

2.1 Multi-Chain Digital Element Analysis

The generation of tow morphologies for this study was accomplished through the utilization of the Multi-Chain Digital Element Method developed by Zhou et al. This section provides a brief outline of this method; for more information on the Multi-Chain Digital Element Method the reader is referred to *Multi-chain Digital Element Analysis in Textile Mechanics* [26].

The Digital Element Method for textile modeling was developed by Wang and Sun [37]. This method involves modeling each tow as a digital chain of rod elements defined as digital elements. The digital elements are connected by frictionless pins or “nodes” and contact between elements is modeled with separate contact elements. A finite element approach is then used to determine changes in digital chain morphology due to both the textile fabrication process and other means of fabric deformation. Although this single-chain digital element method is relatively effective for modeling the morphology of the textile on a fabric-scale, the method is unable to accurately capture the geometry of individual tows. This method models tows as having a constant, usually circular, cross-section, when in reality there is a significant degree of variability in tow geometries.

The Multi-Chain Digital Element Method builds upon the methodology utilized in the single-chain method by simply modeling tows as a collection of digital element chains as opposed to modeling them as a single chain. By utilizing this multiple-chain method, a single digital element

chain now represents a fiber in a tow and the collection of the digital element chains represents the tow as a whole. Doing this allows for geometrical variation along the length of a tow.

In the multi-chain digital element method, digital elements are made such that the digital chain is flexible. As the length of the rod-elements approaches zero, the flexibility of the chain increases. This is due to the frictionless nature of the connecting nodes; therefore the mesh must be well refined to preserve chain flexibility. In order to model the morphology and variation in the fabric tows, a finite element approach is used. The stiffness matrix of the digital elements is the same as rod elements used in finite element analysis [38] and can be seen below in Equation (2.1).

$$[K] = \frac{EA}{L} \begin{bmatrix} 1 & 0 & 0 & -1 & 0 & 0 \\ 0 & \Delta & 0 & 0 & -\Delta & 0 \\ 0 & 0 & \Delta & 0 & 0 & -\Delta \\ -1 & 0 & 0 & 1 & 0 & 0 \\ 0 & -\Delta & 0 & 0 & \Delta & 0 \\ 0 & 0 & -\Delta & 0 & 0 & \Delta \end{bmatrix} \quad (2.1)$$

where K is the stiffness matrix of the digital element, E is the elastic modulus of the material, A is the cross-sectional area of the element, L is the length of the element, and Δ is a small value to prevent the singularity of the matrix. During analysis, if the distance between two nodes is smaller than the diameter of the digital chain, then the analysis generates a contact element. These contact elements have their own stiffness represented in Equation (2.2)

$$\begin{bmatrix} k_n & 0 & 0 & -k_n & 0 & 0 \\ 0 & -k_s & 0 & 0 & k_s & 0 \\ 0 & 0 & -k_s & 0 & 0 & k_s \\ -k_n & 0 & 0 & k_n & 0 & 0 \\ 0 & k_s & 0 & 0 & -k_s & 0 \\ 0 & 0 & k_s & 0 & 0 & -k_s \end{bmatrix} \quad (2.2)$$

where k_n represents the compression stiffness coefficient and k_s represents the lateral stiffness coefficient. When a contact element is generated, the algorithm then determines whether or not the two digital chains are slipping or sticking. If the product of the friction coefficient and the compressive force is greater than the shear force between the two chains, then the two elements are considered to

be sticking. The nodal displacements for the two nodes will henceforth be equivalent and the stiffness coefficients for the contact element, k_n and k_s , are set to an arbitrarily large penalty number. Conversely, if the two tows are considered slipping then the lateral stiffness, k_s , is set to zero. This sticking or slipping determination serves two purposes: first, to more closely model physical reality and second, in the case of sticking, to remove a degree of freedom from the model to increase the speed of the algorithm.

In order to improve the computational efficiency of the model, the Multi-Chain Digital Element method was modified such that the model converged to a solution in 2% of the time required by the original procedure. These modifications will now be discussed; for a more in-depth explanation of the improvements to the methodology see *Mechanics of Textile Composites: Micro-geometry* [39].

In the original model, contact between digital chains is modeled as contact between nodes. Contact elements are therefore modeled as the distance between nodes in contact. Doing this is problematic when the element mesh is too coarse; the compressive force is assumed to align with the compressive force between them, which is only true if the element length approaches zero. Thus, when the mesh is too coarse a lateral component of the compressive force is generated which acts as artificial friction. This friction prevents sliding motion between digital chains. To resolve this, the contact between digital chains was modified such that contact is modeled as the node to element distance instead. With this change and slight modifications to how compressive forces are calculated, the aforementioned artificial friction is eliminated. Ten percent of the computing power necessary to solve the original problem is needed to solve this modified problem.

The original methodology proved to be effective in the simulation of textiles, however it was determined that the step by step nature of the finite element solution was too time consuming to be utilized in the simulation. To solve this, a static relaxation approach was developed consisting of three steps:

- An initial idealized fabric topology “guess”
- Tow discretization
- Static relaxation

In the first step, tows are modeled as a single digital element chain with a consistent circular cross-section. The tows are oriented in an idealized fashion such that they represent the structure of the desired fabric. In the second step, the tows are discretized or “fiberized” into multiple digital chains as defined by the user. The relaxation step consists of assuming a pre-tensile strain (or stress) for each digital chain. This imitates the tension applied to tows during the weaving of the textile preform. Adding this pre-tensile strain generates forces in the nodes and the fabric and then deforms the digital chains until a new equilibrium state is reached. So for each loading step, an incremental pre-tensile strain is assumed, nodal forces are calculated, and then a global stiffness matrix $[K]$ is created. The nodal displacements are then solved by Equation 2.3

$$[K]\{U\} = \{F\} \quad (2.3)$$

where $\{U\}$ is the nodal displacement array and $\{F\}$ is the calculated nodal force array. Next, the new nodal positions are calculated and then the process is repeated until the nodal force is smaller than the user-defined allowable error. Once this is completed, digital chain and tow tensions are calculated and the simulation continues until the targeted tow tensions are met.

2.2 The Independent Mesh Method

The computational stress analysis of the completed composite model for this study was performed utilizing the Independent Mesh Method (IMM) developed by Iarve, Mollenhauer, Zhou, Breitzman, and Whitney. The following section will provide a brief overview of this modeling methodology. For a more in depth explanation of this method see *Independent Mesh Method-based Prediction of Local and Volume Average Fields in Textile Composites* [36].

The Independent Mesh Method is a mixture of both voxel and direct finite element meshing methods. In the IMM, fiber tows are discretized directly and independently. The matrix region is then treated as a global specimen volume that is typically subdivided uniformly. To handle connections between tows and neighboring tows as well as between the tows and the matrix regions, shape functions from the matrix displacement approximation are reduced from the global volume shape functions. All functions entirely covered by tows are excluded and then the integration domain of regions partially covered by tows is modified. All connections between neighboring tows and between tows and matrix are made using the penalty function method. A detailed explanation of the IMM is outlined in the following paragraphs.

The basis for boundary value problems in the IMM is spline approximation. The fiber tow displacement approximation in unit coordinates for an elementary volume $[0, 1]^3$, is written as

$$\mathbf{u}(\xi) = \sum_{i \in \Omega} X_i(\xi) \mathbf{U}_i, \quad (2.4)$$

where $X_i(\xi)$ represents the three dimensional shape functions, \mathbf{U}_i are the displacement approximation coefficients, and Ω is the set of the total number of approximation functions. The B-spline basis allows one to build a system of basis functions where the displacements at the end nodes are the coefficients of the spline functions. This allows one to impose boundary conditions by assigning spline function coefficients similar to how one would impose boundary conditions in a traditional finite element approximation (generally displacements in internal nodes are not explicitly equal to the coefficients of the spline, but are a close approximation). Equation 2.4 is then transformed from unit coordinates to global xyz coordinates, giving

$$\mathbf{u}(\mathbf{x}(\xi)) = \sum_{i \in \Omega} X_i(\xi) \mathbf{U}_i, \quad \xi \in [0, 1]^3 \quad (2.5)$$

where $\mathbf{u}(\mathbf{x}(\xi))$ is the displacement of the nodes in the fiber tows with x_1, x_2 , and x_3 referring to the x, y , and z directions respectively. The transformation function $\mathbf{x}(\xi)$ is written as

$$\mathbf{x}(\xi) = \sum_{i \in \Omega} X_i(\xi) \mathbf{C}_i, \quad \xi \in [0, 1]^3 \quad (2.6)$$

where \mathbf{C}_i are the coefficients of the 3D spline approximation which is based on the Bezier surface definitions generated by VTMS. Coordinates of ξ_1 are always defined in the direction of the tow such that fiber direction can be automatically assigned. Next, the constitutive relation in the global coordinate system is written as

$$\sigma = \mathbf{C}(\mathbf{x})(\epsilon - \mathbf{e}(\mathbf{x})) \quad (2.7)$$

where σ and ϵ are the stress and strain tensors, respectively, and $\mathbf{C}(\mathbf{x})$ and $\mathbf{e}(\mathbf{x})$ are the stiffness matrix and non-mechanical strain coefficients. Finally, from Equation 2.7, it follows that the strain energy variation for the i th fiber is

$$\delta W_i = \int_{v_j} \mathbf{C}(\mathbf{x})(\epsilon - \mathbf{e}(\mathbf{x})) \delta \epsilon dV \quad (2.8)$$

The displacement approximation in the matrix is in the same form as Equation 2.5, except the domain is no longer a unit cube. With this change in domain the $\mathbf{x}(\xi)$ transformation becomes

$$x_1 = L\xi^1, \quad x_2 = W\xi^2, \quad x_3 = H\xi^3 \quad (2.9)$$

The integration domain is then determined by taking the unit domain and then subtracting the volumes occupied by the individual tows. The strain energy in the matrix phase is written as

$$\delta W_M = \int_{v/UV_i} \mathbf{C}_M(\epsilon - \mathbf{e}_M) \delta \epsilon dV \quad (2.10)$$

where the M subscript denotes the matrix phase and the v/UV_i shows the modified volume by use of integration cubes.

The IMM allows for tow morphologies to be modeled independently and at a high fidelity. Iarve et al. were able to capture sharp variations of the strain components in triaxially-braided composites.

This method verification will not be discussed here; for additional information, the reader is once again referred to [36].

It is worth noting that the variation of fiber volume is currently not taken into account for the stress and strain calculations. Upon completion of this study, fiber volume fraction variation will ideally be implemented in the IMM formulation. However, the means of this implementation are outside the scope of this study and will not be discussed further.

2.3 Expectation Maximization of the Maximization of Posterior Marginals

The Expectation Maximization of the Maximization of Posterior Marginals (EM/MPM) is a program designed for segmentation of high fidelity images [41] [42] [43]. The purpose of segmentation is to classify fibers and matrix into distinct pixel classes; doing this will make it easier to analyze the image as opposed to attempting to analyze a three dimensional uint8 image matrix. An image is typically composed of a three dimensional matrix of pixel values of data type uint8. Each pixel consists of three values: a red intensity value, a green intensity value, and a blue intensity value. These intensity values are then mixed together to generate the color of the specific pixel. This structure type is good for outputting various colors on a computer screen, but inherently difficult to analyze. This is why it is important to perform image processing techniques such as segmentation or thresholding. These techniques present the image in a more simplistic manner so that it is easier to analyze the image.

In addition, image segmentation can be used to diminish Poisson noise— random pixel intensities that generate noise in the image. EM/MPM is a modification of the MPM algorithm which uses a Mote Carlo algorithm that classifies pixels according to the best fit of the smoothness of the current segmentation as well as the collective image intensity at the pixel. A segmented image can typically be modeled with a Poisson distribution, but for simplicity EM/MPM models this with

a Gaussian distribution. Each Gaussian distribution has a mean and standard deviation that are calculated automatically with the expectation maximization part of the algorithm.

EM/MPM can generally generate an accurately segmented image with only three input parameters: exchange energy, mean pixel intensity values for each pixel class, and standard deviation from the mean intensity for each pixel class. Exchange energy is generally a value between zero and one and refers to the amount of “energy” there is for pixels to overtake pixels of an opposing class. For instance, take a pixel that is classified as a white pixel, but is completely surrounded by black pixels. If the exchange value is high (a value greater than 0.5), then there is a higher likelihood that the black region of pixels will overtake the white pixel. This white pixel would then be classified as a black pixel for the following segmentation loops in the algorithm. In other words, regions of a particular class may overtake lone pixels of an opposing class. Essentially, having a higher exchange energy can be used to eliminate possible noise in the image but can also lead to pixel misclassification if not used properly.

The other two main parameters utilized in EM/MPM relate to pixel class definitions. The mean is a value between 0 and 255 and refers to the average pixel intensity of the class. Likewise, the standard deviation is the pixel class’s standard deviation from the mean pixel intensity. EM/MPM has the ability to assign these parameters automatically based on the number of classes chosen and the intensity values of the original image. However, for images where one pixel class intensity is very close to another, manual initialization will most likely need to be utilized.

Because of the multiple parameters within EM/MPM, all of which have an effect on one another, there is no one clear solution for the segmentation of an image. For smaller image sizes, segmentation of a single image takes an insignificant amount of time. Therefore, the parameterization of pixel classes and exchange energy is primarily a trial-by-error process. The EM/MPM parameterization technique used for this study will be summarized in Section 4.7.

2.4 Hough Transform Feature Extraction

The Hough transform feature extraction method developed by Przybyla et al [40] is a means of detecting fibers in an image of a composite material. Developed for use in ceramic matrix composites, this methodology first involves the utilization of EM/MPM for segmentation purposes. For fiber detection purposes, a class of algorithms known as generalized Hough transforms are used to find geometric parameters to describe imperfect geometric shapes [44] [45]. For instance, two circles may appear conjoined in an image; a Hough transform would then be utilized to identify both circles. For an image where fibers are not in the same plane as the sectioning plane, fibers will appear as an elliptical shape due to the angled sectioning of the composite. For identification of ellipses, five parameters are necessary:

- the x and y coordinates of the center of the ellipse (x_0, y_0)
- the major axis a
- the minor axis b
- the orientation of the ellipse θ

The method developed by Przbyla et al. first defines the edges of the fiber candidates. At this point, most fibers appear as a clustered grouping object and are not elliptical in shape. The algorithm then defines the centers of the candidate ellipses within clusters and attempts to find ellipse parameters of individual fibers. Parameterized ellipses are defined as fibers and then output statistics for the image are generated.

For the purposes of this study, an attempt was made to use the Hough transform feature extraction method which will be discussed in Section 4.3.

CHAPTER III

EXPERIMENTAL METHODS

3.1 Specimen Fabrication

A 3TEX 3D orthogonal textile weave was utilized for this study (preforms were courtesy of Army Research Laboratory- Dr. James Sands). Fiber tow specifications were as follows:

- Warp: IM7 12k
- Weft: IM7 6k, AS4C 3k
- Binder: S-1250 Glass

The fabric preform consisted of 7 warp tows and 8 weft tows through the thickness of the fabric. Measured approximate average tow diameters were 1.5 mm for binder tows and 1.7 mm for both warp and weft tows respectively. The average thickness of the preform was 3.175 millimeters. The fabric preform utilized for this study can be seen in Figure 3.1.

For the generation of the composite specimens, all processes were conducted in-house at AFRL in order to quickly obtain usable specimens. Epon 828 polymer resin was first mixed with D230 cure agent by hand until the mixture exhibited a consistent and homogeneous texture. The resin was then poured into a large aluminum pan and then inserted into a Ladd Vacuum Evaporator. The evaporator was used as a vacuum chamber to debulk the resin; in other words, it was used to eliminate any air pockets or bubbles that were introduced to the resin during mixing. In addition, utilizing the evaporator removed any unwanted moisture from the resin. The resin was left in the

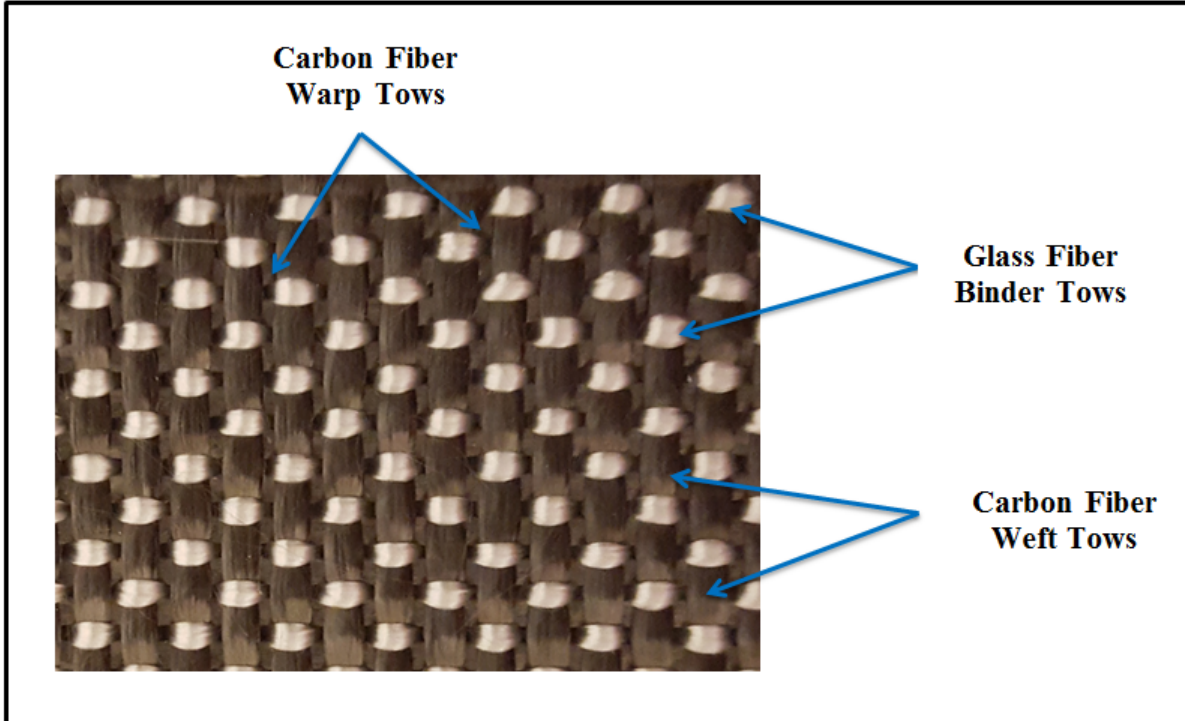


Figure 3.1: 3D Orthogonal Weave Textile Preform Utilized in Study

vacuum chamber at approximately zero atmospheres of pressure until all visible air bubbles were eliminated from the resin. After the resin was debulked, the resin was poured evenly over the fabric preform. The fabric was carefully flattened by hand during pouring to ensure that the resin infiltrated all areas of the preform. The infiltrated preform was then placed between two platens loaded at approximately fifteen pounds of force and was left to cure for three days. After the third day, the platens were removed and the preform was placed in a Thelco Laboratory Precision Oven at 32 degrees Celsius for 24 hours.

Imaging of the material was conducted using a Zeiss XRM-520 X-ray CT and loaded in-situ using a Deben load frame while CT images were being taken. Doing this allowed for the examination of micro-level damage evolution for the 3D textile specimens loaded in tension. In order to fit in the Deben fixture, the 3D textile composite had to be cut into dog-bone specimens with the

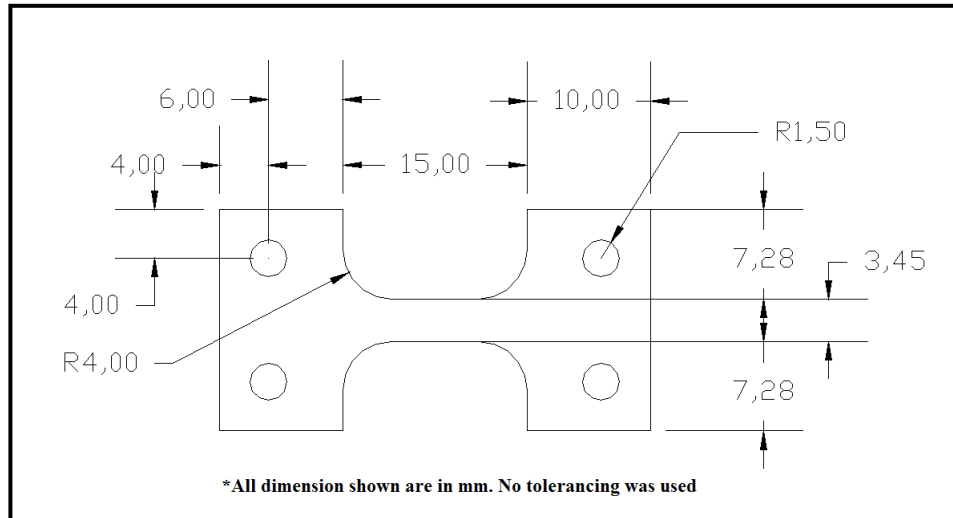


Figure 3.2: Technical Drawing of Waterjet Cut Dog-Bone Specimens

dimensions shown in Figure 3.2. Tolerancing was not utilized during the cut; instead the specimens were cut such that the edge of the gage section aligned with the edge of the binder tow boundaries. This allowed for high resolution X-ray CT imaging of binder tow variability. With the exception of the holes, the dog-bone specimens were cut to specifications with a waterjet at Kerf Waterjet in Dayton, Ohio. The holes were drilled by hand with a tabletop drill to ensure that no damage was introduced into the composite specimens prior to testing.

In total, ten specimens were cut; five specimens with gage sections that included three binder tows and five specimens with gage sections that included two binder tows. Figure 3.3 shows one of the dog-bone specimens prior to imaging and loading.

3.2 Micro-CT Imaging

Specimens were fastened to the Deben load frame by inserting pins through the holes in the dog-bone specimens. After being secured in the Deben load frame, the specimens were inserted into a Zeiss XRM-520 CT. The chosen voxel size was 1.34 microns to capture the largest area of specimen

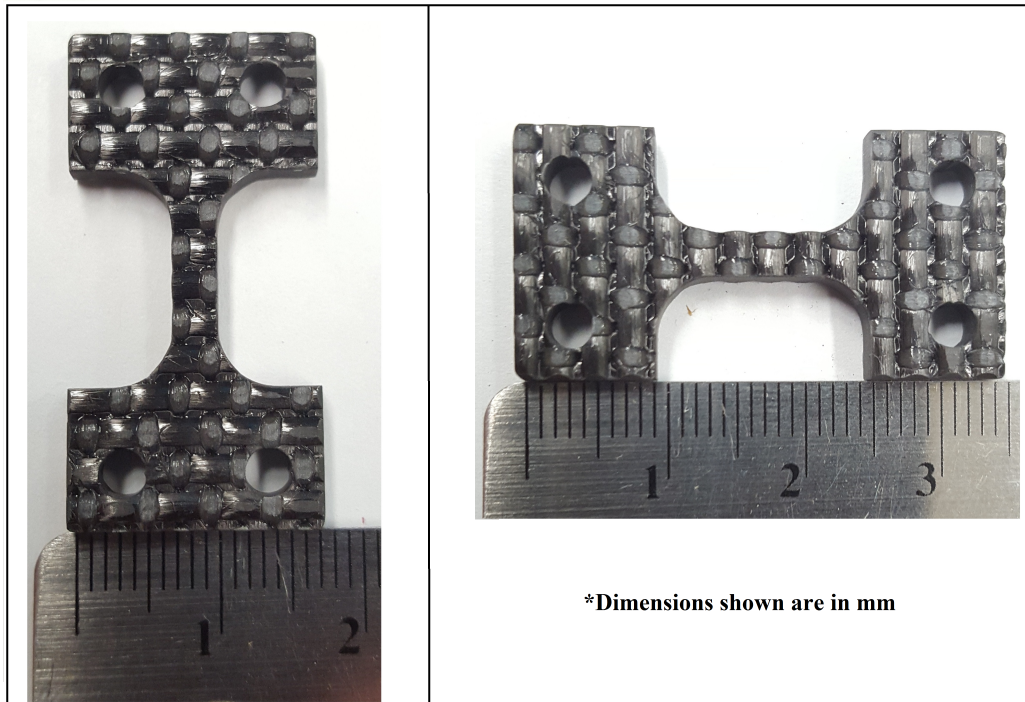


Figure 3.3: Example of a Final Waterjet Cut Dog-Bone Specimen

possible without greatly sacrificing image resolution. The scan time for imaging of samples with this voxel size was approximately 19 hours. First, a specimen was imaged at an in-situ load of 100 Newtons. This low load was applied to obtain baseline imaging data for the specimen.

Figure 3.4 shows the fully imaged specimen and Figure 3.5 shows the specimen's binder tows with all other regions masked. Both of these baseline images were vital to understanding how to properly model the specimens. The degree of geometry variation was relatively high for the binder tows considering the small size of the sampled region. The binder tows "flanged out" towards the top and bottom of the specimen where the level of pressure on the fibers induced by the warp and weft tows were likely the smallest. For clarity, Figure 3.6 depicts the cross-section at the centerline of the specimen. Figure 3.6 shows how the binder tows were woven through the thickness of the weave. Furthermore, there was a significant geometry variation observed in the weft tows. The weft

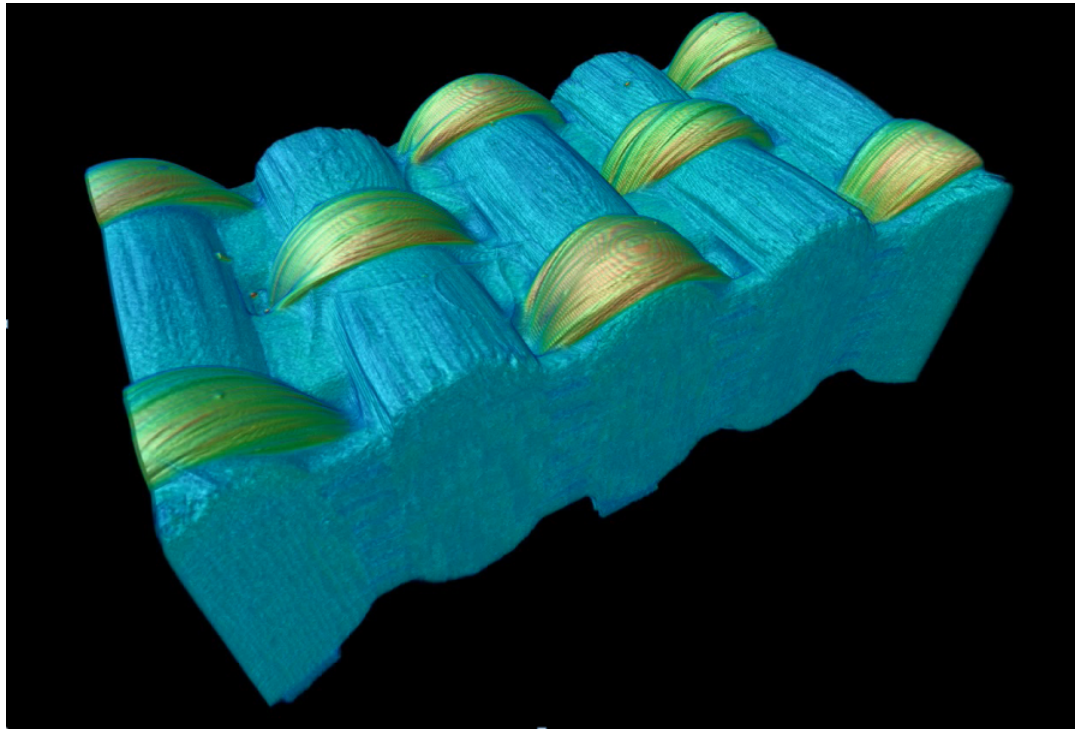


Figure 3.4: Three Dimensional Imaging of Dog-Bone Specimen Gage Section

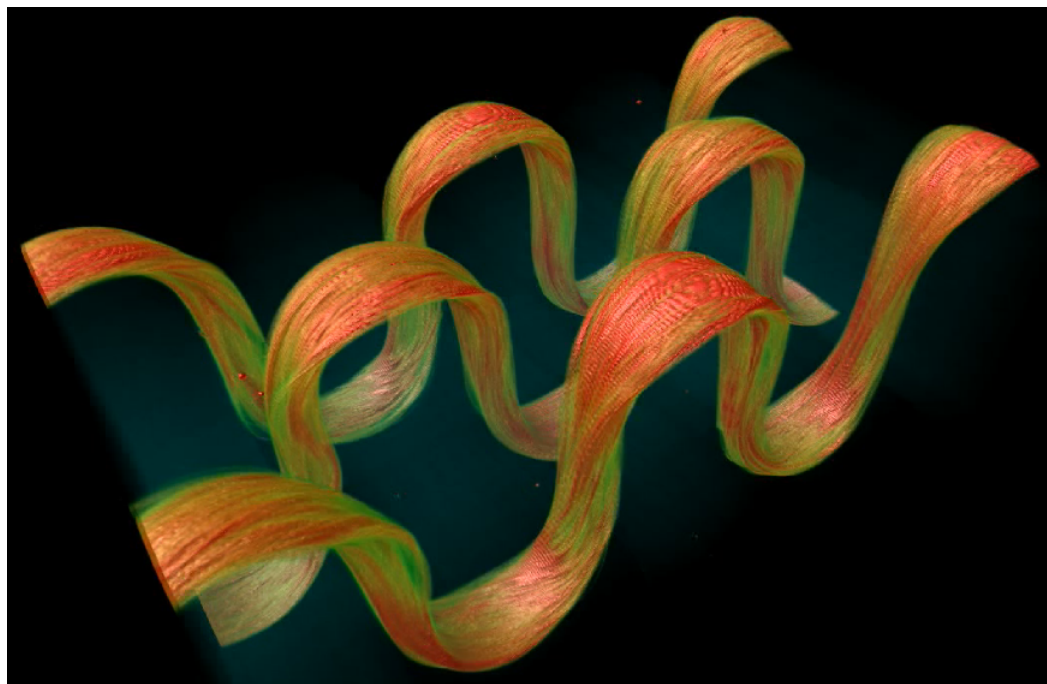


Figure 3.5: Imaged Binders of Dog-Bone Specimen Gage Section

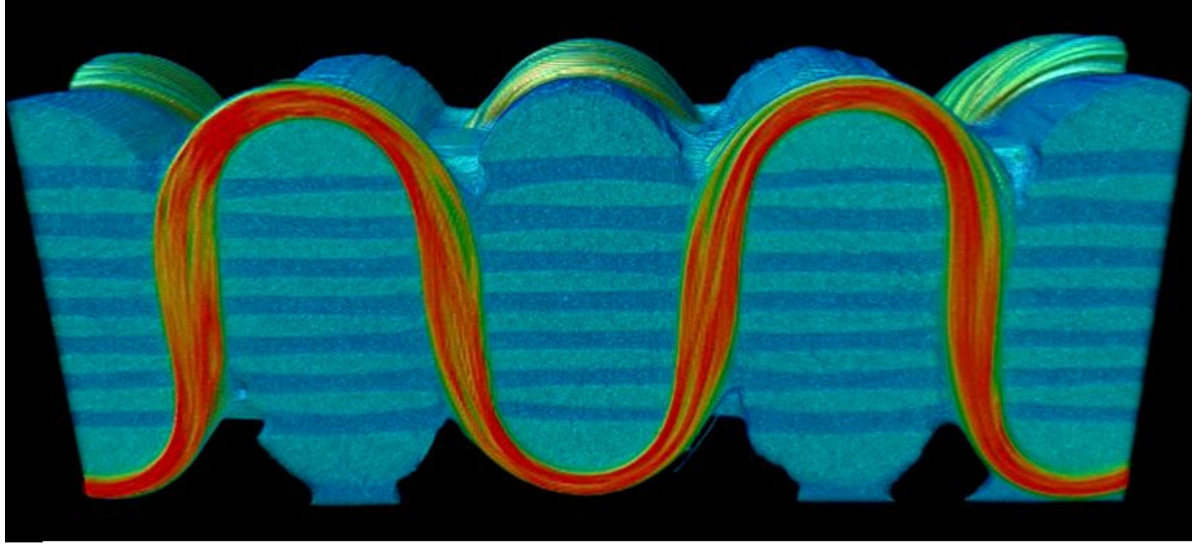


Figure 3.6: Micro-CT Image of Cross-Section at the Centerline of Specimen

tows on the top and the bottom of each weft stack exhibited a more hemi-cylindrical shape while the inner weft tows appeared rectangular. This variation was most likely due to a higher degree of pressure exhibited in the inner weft tows. This data was invaluable in terms of improving the geometric accuracy of the finite element model discussed in Chapter VI.

After baseline imaging was taken, specimens were imaged under four different in-situ loading conditions- 1000N, 2000N, 3000N, and 4950N. Figure 3.7 shows a cross-section of the sample obtained through micro-CT imaging. Although this imaging technique was useful for obtaining an accurate geometric description of the sample, it fell drastically short in obtaining any useful information as it pertains to fiber volume fraction variation. Although some fibers were distinguishable, especially in the lower fiber density binder tows, in general the fibers could not be detected separately from the matrix. After this, it was clear that micro-CT did not provide the resolution required for describing local fiber volume fraction variation throughout the specimens.

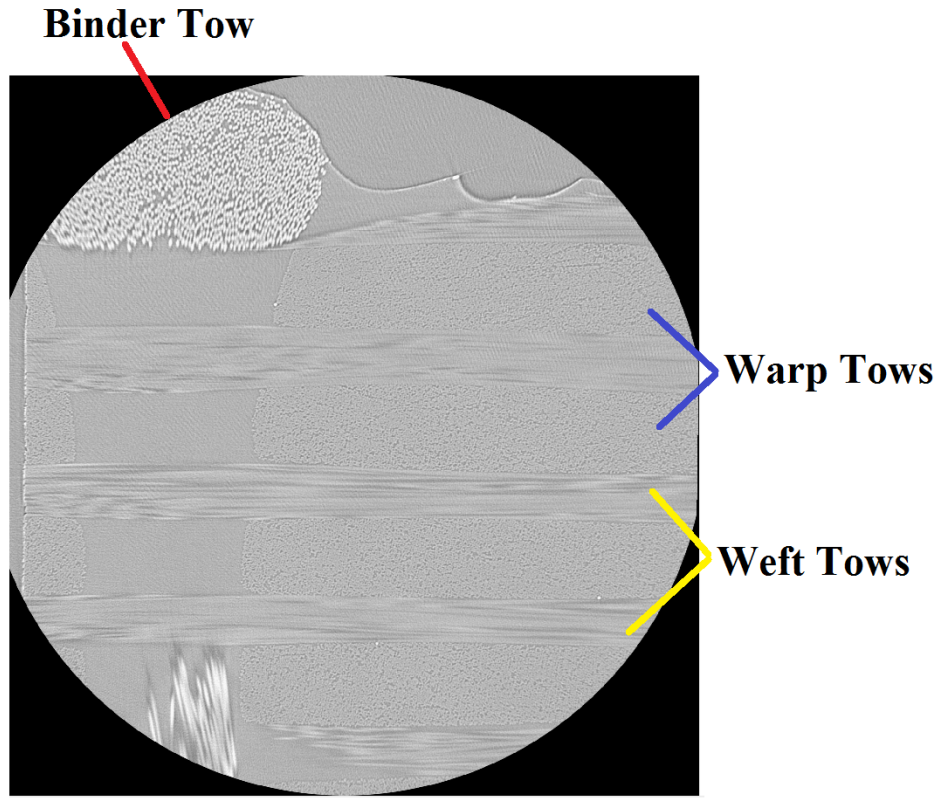


Figure 3.7: Cross-Section from Micro-CT Imaging of Dog-Bone Specimen

3.3 Digital Volume Correlation

Utilizing the images from the micro-CT scans, digital volume correlation was performed on the specimens. In general, digital volume correlation examines a volume region of interest throughout a loading cycle. By determining the differences in a voxel over multiple loading steps, stresses, strains, and displacements for that voxel can be calculated. Because the glass tows exhibited such a high degree of geometric variability, it would have been difficult to obtain accurate calculations of stresses, displacements, and strains. Because of this, the region of interest was chosen such that only the carbon fiber regions were incorporated. Furthermore, resin pockets were difficult to correlate considering they are similar in coloration to air and their lack of distinguishing features. These resin regions were therefore also avoided. Digital volume correlation was performed utilizing Correlated

Solutions, Inc. *VIC Volume* software. The volume size in plane was 1654 x 1739 voxels and the total number of slices was 1239. The orientation of the image was such that the x direction was the through-thickness direction of the composite, y was the direction of the weft tows, and z was the direction of the warp and binder tows. Displacements in the x , y , and z directions were represented by u , v , and w , respectively. Results from this test are discussed in Section 8.1.

CHAPTER IV

INITIAL SERIAL SECTIONING AND ANALYSIS METHODOLOGY DEVELOPMENT

4.1 Serial Sectioning Introduction

Upon completion of digital volume correlation and all other lab tasks, an effort was made to obtain high fidelity imaging of the composite specimens such that individual fibers in the composite could be detected. For this purpose, the specimens were serially sectioned utilizing the Robo-Met 3D system. Serial sectioning on Robo-Met 3D automatically polishes samples and provides imaging capabilities with a fidelity as high as 0.25 microns per pixel [46], [47], [48]. All serial sectioning was conducted at AFRL, courtesy of Dr. Mike Uchic (AFRL/RXCM).

Serial sectioning, by nature, is a destructive process; therefore, sectioning was only performed after all other lab tasks had been completed. In addition, serial sectioning is also a very time intensive process; for high fidelity images, obtaining one image slice can take nearly two and a half hours. Because of this time constraint, it was determined that only two specimens would be imaged utilizing Robo-Met 3D. The first specimen was used to test the feasibility of gathering fiber volume fraction variation data for the 3D PMC textile composite. Imaging of this specimen was to consist of one high resolution image and then 24 lower resolution images that covered a small volume of the material. If obtaining a FVF variation was determined to be feasible, then a second specimen would be imaged. The imaging of the second specimen would cover a much larger volume than the

first specimen, and would be a much more time intensive imaging process. Ideally, the fiber volume fraction data from this second specimen could then be implemented within the VTMS model.

This chapter will discuss the preliminary imaging of the first serially sectioned specimen and discuss the subsequent image analysis methodology development. The imaging of the second specimen will be outlined in Chapter V.

4.2 Preliminary Serial Sectioning of 3D Textile PMC Specimen

As stated previously, the primary goal of serially sectioning the first specimen was to test the feasibility of gathering fiber volume fraction variation data from the specimen. Additionally, it was desired to obtain this FVF data for all three different tow types: warp, weft, and binder. To this end, the specimen had to be sectioned at an angle such that fibers for all tows appeared as ellipses in the field of view for each image slice. The specimen was imaged at approximately 45 degrees in all x , y , z planes (since this was merely a preliminary feasibility analysis, an exact angle was not required). An image slice from the serial sectioning of the first composite specimen is provided in Figure 4.1.

4.3 Image Fiber Volume Fraction Extraction

With the images obtained from serial sectioning, methodologies were tested to quickly determine fiber volume fraction variation in the images. First, an attempt was made to utilize a high-end imaging processing software, VG Studio Max. VG Studio Max has the capability to visualize image slices as a 3D volume and then extract certain features from the represented volume. Surface extraction was attempted utilizing this software with the hopes of defining all the fibers in the image stack as a surface. However, due to the design of the surface extraction algorithm, it was noted that the software tended to extract fibers that were within close proximity to each other as one surface. In other words, the software systematically eliminated a significant amount of resin that was present in



Figure 4.1: Image Slice of Specimen from Robo-Met Serial Sectioning

between individual fibers. This process was therefore determined to not be suitable for the purposes of the study.

After VG Studio Max proved to be unsuccessful at detecting fibers in the image, the Hough transform feature extraction method discussed in Section 2.4 was used. Although this methodology was promising, it was also unsuccessful for the images obtained from the samples in this study. Figure 4.2 depicts the use of the Hough transform method to identify fibers in a portion of the image obtained from serial sectioning. The red ellipses in the figure indicate a region in which the algorithm had detected a fiber. Although the algorithm detected some fibers, there were still a large amount of fibers that were not detected. This was particularly true for regions of closely packed fibers; these regions appeared as a conjoined surface rather than as an identifiable ellipse. Furthermore, some closely packed regions also led to a large ellipse being generated, indicating that the algorithm believed that this region was a large fiber. Considering all of this, Figure 4.2 is indicative of an inaccurate result.

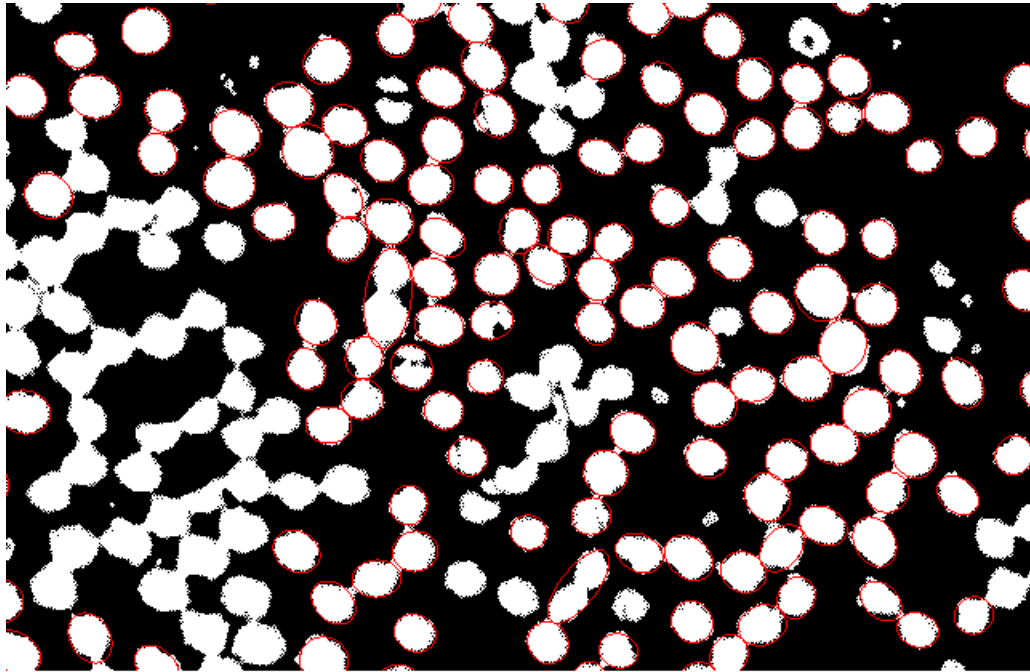


Figure 4.2: Fiber Identification in a Segmented Image Using the Hough Transform Method

The issues observed were possibly due to the fact that the Hough transform method had only been used successfully for ceramic matrix composite samples. For CMCs, fibers generally appear more well-defined due to the high optical contrast between the fibers and the matrix. In addition, usually CMCs have more well defined fiber coatings which can be used to make fiber detection an easier process. Given these difficulties, it was determined that the Hough transform feature detection method would not be suitable for this study. In further works, it may be useful to revisit this methodology.

4.4 Binary Image Fiber Volume Fraction- Methodology

After the difficulties with the aforementioned methodologies, it was determined that a methodology should be specifically developed for this study. The objective of this analysis was to simply extract an accurate fiber volume fraction variation for both the fabric as a whole and for individual

tows. Therefore, the first priority was to develop an accurate method for obtaining a fiber volume fraction variation for any given image. The Hough transform method attempted to accomplish this by detecting individual fibers in the image. Once a fiber was detected, the pixels within that fiber would then contribute to the total fiber area. The difficulty with this method was detecting the fibers given the close compaction of the fibers. However, for the purposes of this study, it is not important to detect individual fibers or their shape. Because of this, it was determined that the new methodology should simply bypass the fiber detection step all together.

The developed method processes the images into two distinct pixel classes—fiber and matrix. A standard MATLAB gray-scale thresholding command, *graythresh*, is utilized in this method, and then the gray-scale image is converted to a binary black and white image. A value of one corresponds to a white fiber pixel, while a zero corresponds to a black matrix pixel. A window size is defined and the image is then divided into a grid with each cell's dimensions equal to the window size defined. Within each cell of the grid, the white and black pixel amounts are totaled and then the ratio of the number of white pixels to black pixels is calculated. This ratio is the approximation for the fiber volume fraction of the cell. This method consists of two scripts shown in Appendices A and B.

4.5 Binary Image Fiber Volume Fraction- Experimental

Using the binary image fiber volume fraction technique, the serially sectioned image was converted to a black and white binary image shown in Figure 4.3. As shown in this figure, the binary image closely resembled the original serially sectioned image. However, the binder fibers in the upper middle area of the image were classified incorrectly as a matrix/void region. An additional step was necessary for binder fiber classification which will be described in Section 4.7.

After thresholding the image, a window size of 100x100 pixels was selected and the fiber volume fraction variation was calculated. For visualization purposes, the fiber volume fraction was

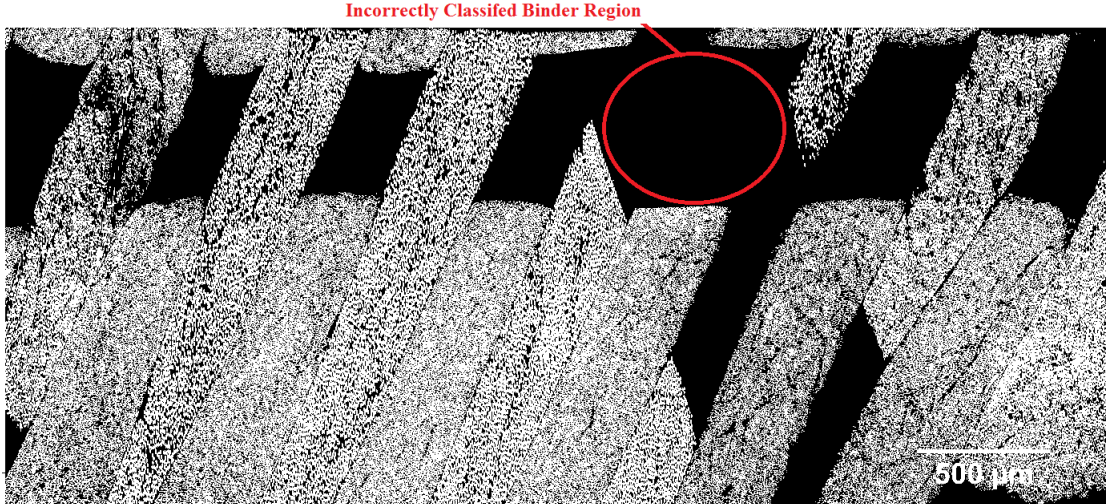


Figure 4.3: Binary Black and White Thresholded Image of Serial Section Slice

imaged as an intensity map shown in Figure 4.4. The intensity map of fiber volume fraction closely resembled the original serially sectioned image. However, many fiber volume fraction values were unrealistically high. This was due to too small of a window size; this window size was therefore increased to 200x200 pixels which generated much more realistic fiber volume fraction values.

4.6 Individual Tow Cropping- Methodology

After creating a methodology for a fiber volume fraction approximation, the next challenge was to determine a method for relating fiber volume fraction values to individual tows. For this problem, a separate code was developed to crop out tows from the original image. In this method, the number of tows in the image is defined by the user. The image is then loaded into MATLAB's graphical user interface and the user defines polygons that surround the tows using the *impoly* command. After the initial tow boundaries are defined for the first image, the script then pauses until the user approves all the bounding polygons in the image. The locations of all the vertices of the polygons are then saved and the next image is then automatically loaded into the MATLAB GUI. The polygons from

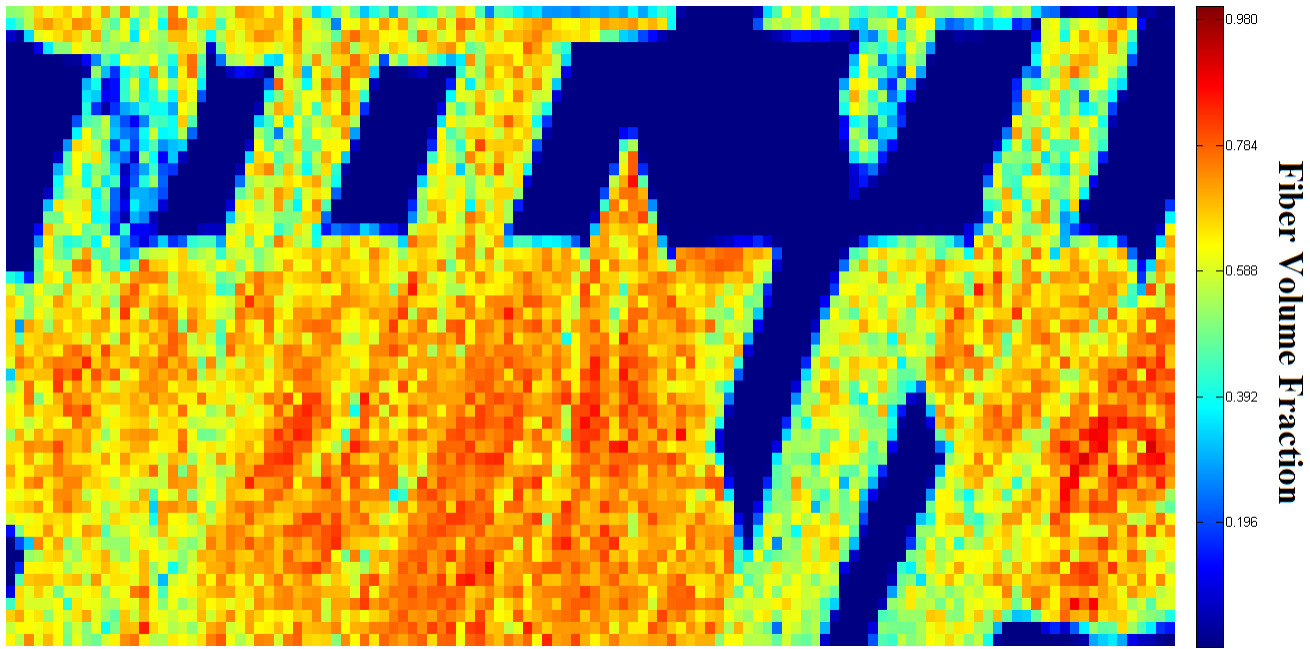


Figure 4.4: Fiber Volume Fraction Intensity Map for 100x100 Pixel Window Size

the previous image are automatically drawn on the new image and the script is once again paused until the user accepts the result. This allows for the user to make the micro-adjustments necessary for each image slice without having to manually re-draw the polygons each and every time. The coordinates of the polygons are saved within a MATLAB structure variable and are sent to the fiber volume fraction calculation script. This script then masks out all portions of the image that lie outside of the bounding polygon and calculates the fiber volume for all cells within the tow. This is performed for each individual tow in the image and the data is saved to another MATLAB structure variable for future use. Utilizing this approach, it takes an average of approximately thirty seconds to define bounding polygons on an image slice. This speed was deemed acceptable and viable for the purposes of this study. The script described is given in Appendix C.

An example of a tow geometry cropped from the original serially sectioned image is depicted in Figure 4.5. The tow in this figure appears as a stitch of the individual cells that lie within the tow

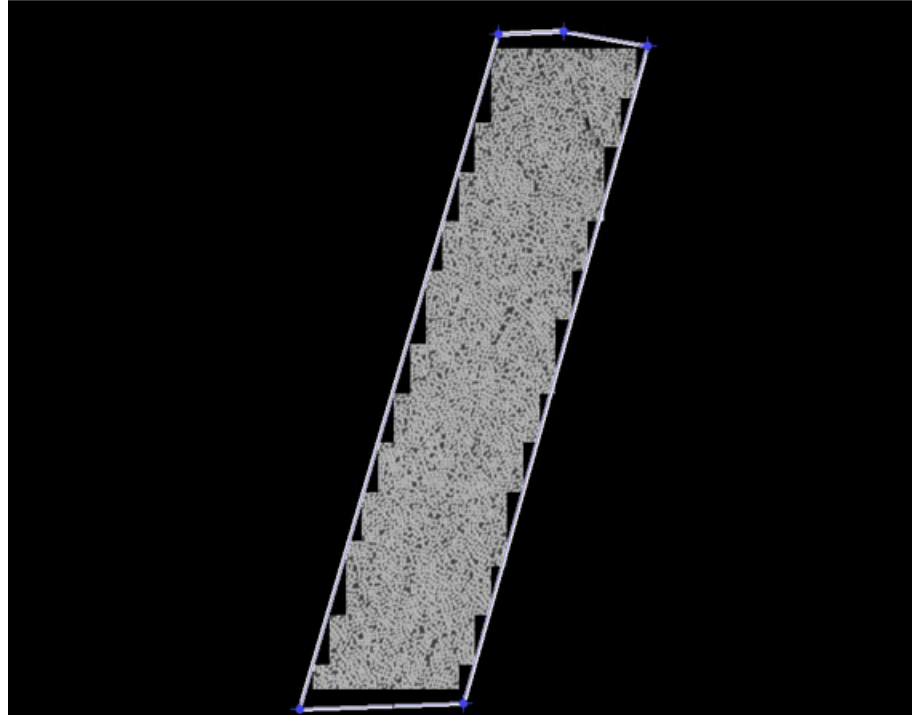


Figure 4.5: Tow Geometry Cropped from Original Serially Sectioned Image

bounding polygon. Although the stitch does not fully capture all parts of the tow, enough data can be extracted to obtain an accurate fiber volume distribution.

4.7 Binder Region Fiber Volume Extraction

As mentioned earlier, the thresholding technique utilized for the warp and weft tows was not capable of identifying fibers in the binder tow region. The reason for this was that the binder fibers in the image were considerably darker than the fibers in the warp and weft tows (likely due to the nature of glass fibers). To solve this issue, image segmentation was performed on the binder region using the EM/MPM software described in Section 2.3.

The serially sectioned image was first uploaded into the EM/MPM software. The histogram and Gaussian plot shown in Figure 4.6 was then analyzed. The blue line in this figure refers to

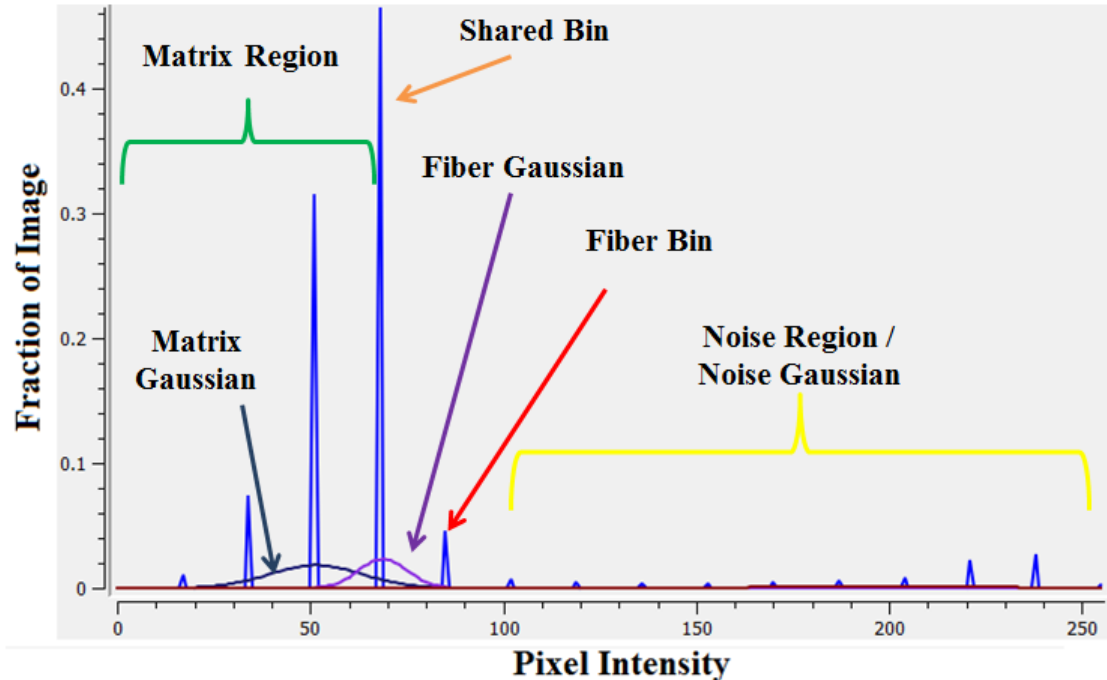


Figure 4.6: Histogram and Gaussian Plot of Image of Binder Region

the histogram of the input image, depicting the intensities of the input image. The other colored lines show the Gaussian pixel classifications of the image segmentation. Since the goal for this segmentation was to accurately classify fibers in the image, three pixel classes were defined: fiber class, matrix class, and noise class (for the purposes of this segmentation, warp and weft fibers were considered noise class). The histogram shown in Figure 4.6 shows that the binder fibers generally fell between an intensity value of 65 and 90. Furthermore, the matrix region was very close in intensity to the fiber bins, meaning that matrix and fiber classes probably had a shared bin centered at an intensity of 68. This was why this bin almost incorporated 50% of all pixel intensities in the image. The truly distinct fiber region was likely centered about an intensity of 85 on the histogram plot, and was therefore set as the mean for this pixel class. Since the fiber region covered a very small portion of the histogram plot, the standard deviation was set to a lower value than the other two classes. The chosen pixel class parameters were as follows:

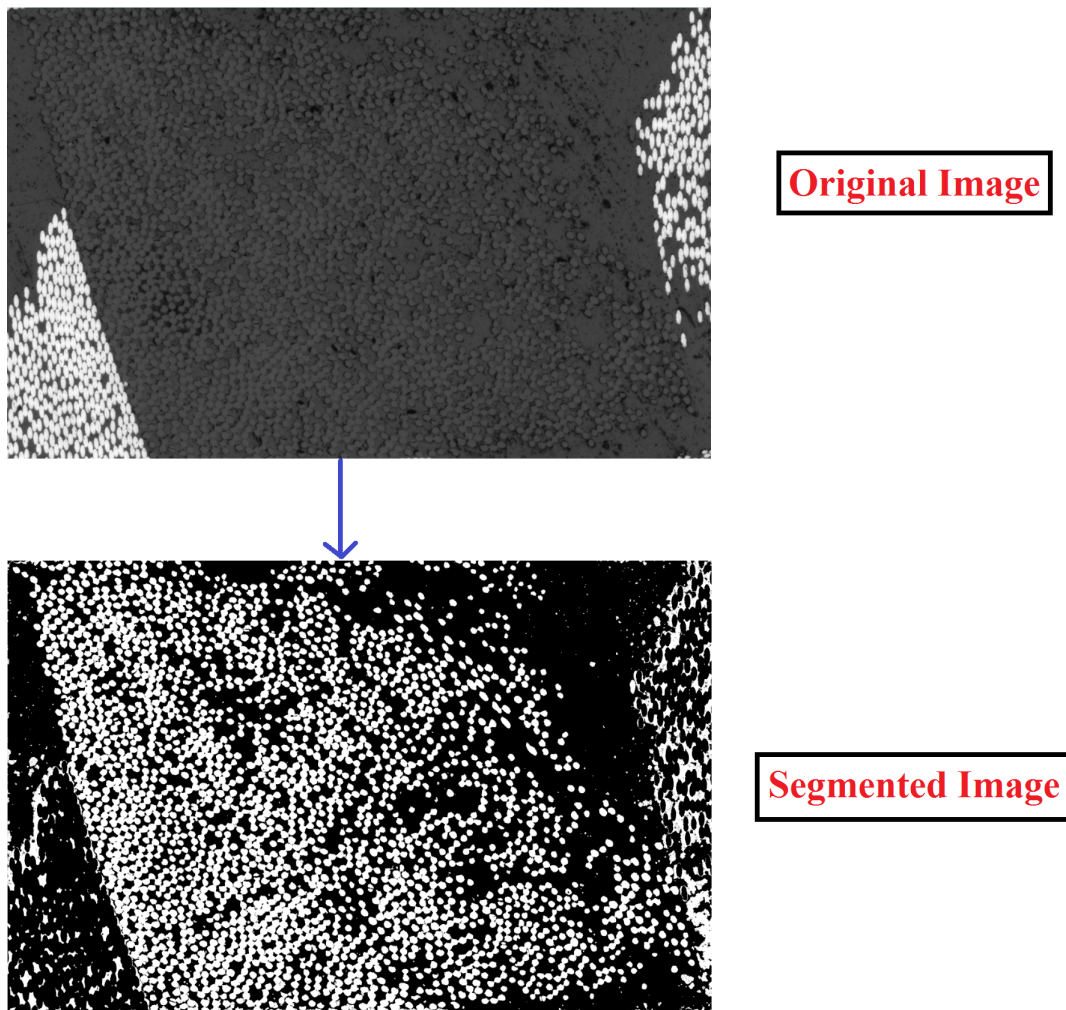


Figure 4.7: Segmentation of Binder Region

- Class 0 (Matrix Class)- Mean 40, Std Dev 20
- Class 1 (Fiber Class)- Mean 85, Std Dev 8
- Class 2 (Noise Class)- Mean 175, Std Dev 75

Figure 4.7 shows the original image of the binder region and the successful segmentation using the defined parameters.

4.8 Binary Image Fiber Volume Fraction Methodology Accuracy

To test the accuracy of the methodology, areas of the image were randomly selected with the stipulation that only areas with full fiber ellipses were considered. The total fiber volume fraction was then calculated by simply adding all the ellipse areas together in the image and then dividing it by the total image size. Figures 4.8 and 4.9 show two different image sets where this accuracy test was carried out. Figure 4.8 shows that the methodology consistently overestimated the fiber volume fraction of the given images. This was to be expected since there were likely random areas of white pixels outside of the fiber region. In addition, areas surrounding the fiber likely had too high of a white pixel intensity which may have led to their misclassification.

This intensity issue was particularly true for areas in-between two closely packed fibers. The residual white intensity of the two fibers created an area between the fibers that had too high of a white pixel intensity to be classified as matrix. As seen in the third image of Figure 4.8, the two fibers appeared to be joined together in this middle region. Despite this issue, there was only an approximate 3.5% difference between the pixel counting methodology and the original image fiber volume fraction approximation for the third image of Figure 4.8. It was determined that this difference was acceptable for the purposes of this study.

Examining the second image set in Figure 4.9, the first two images show the accuracy of the methodology when the window contained multiple fibers. The second image contained the most fibers of any of the images tested, and was shown to be the most accurate image. The methodology for this image was only approximately 0.25% lower than the control approximation. This finding suggests that the fiber volume fraction calculation for the entire image was likely more accurate than the other images. In other words, variations in accuracy for individual fibers (some fiber volumes are under-predicted while others are over-predicted) ultimately canceled each other out. Finally, the last image shows the accuracy of the methodology utilized for the binder region. Since the binder

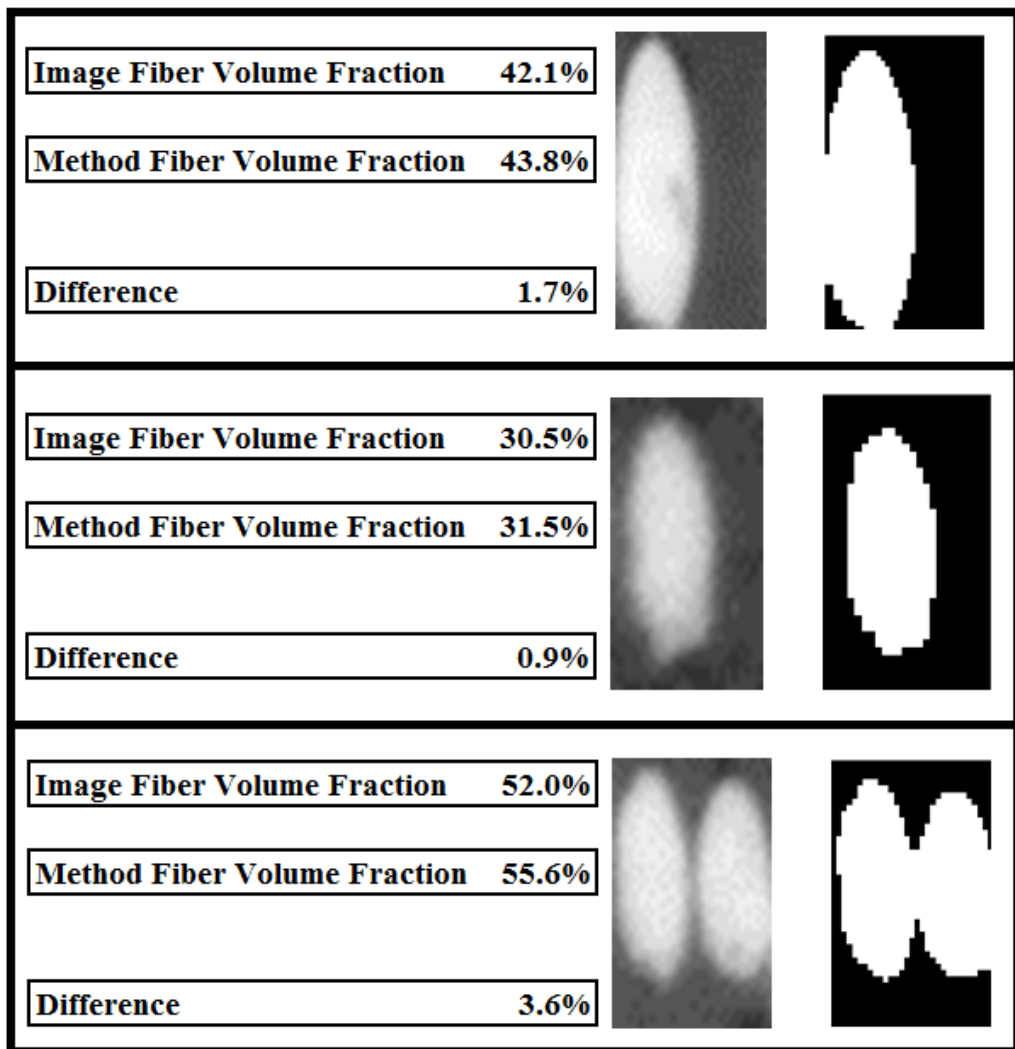


Figure 4.8: Accuracy of Binary Image Fiber Volume Fraction Methodology- Image Set 1

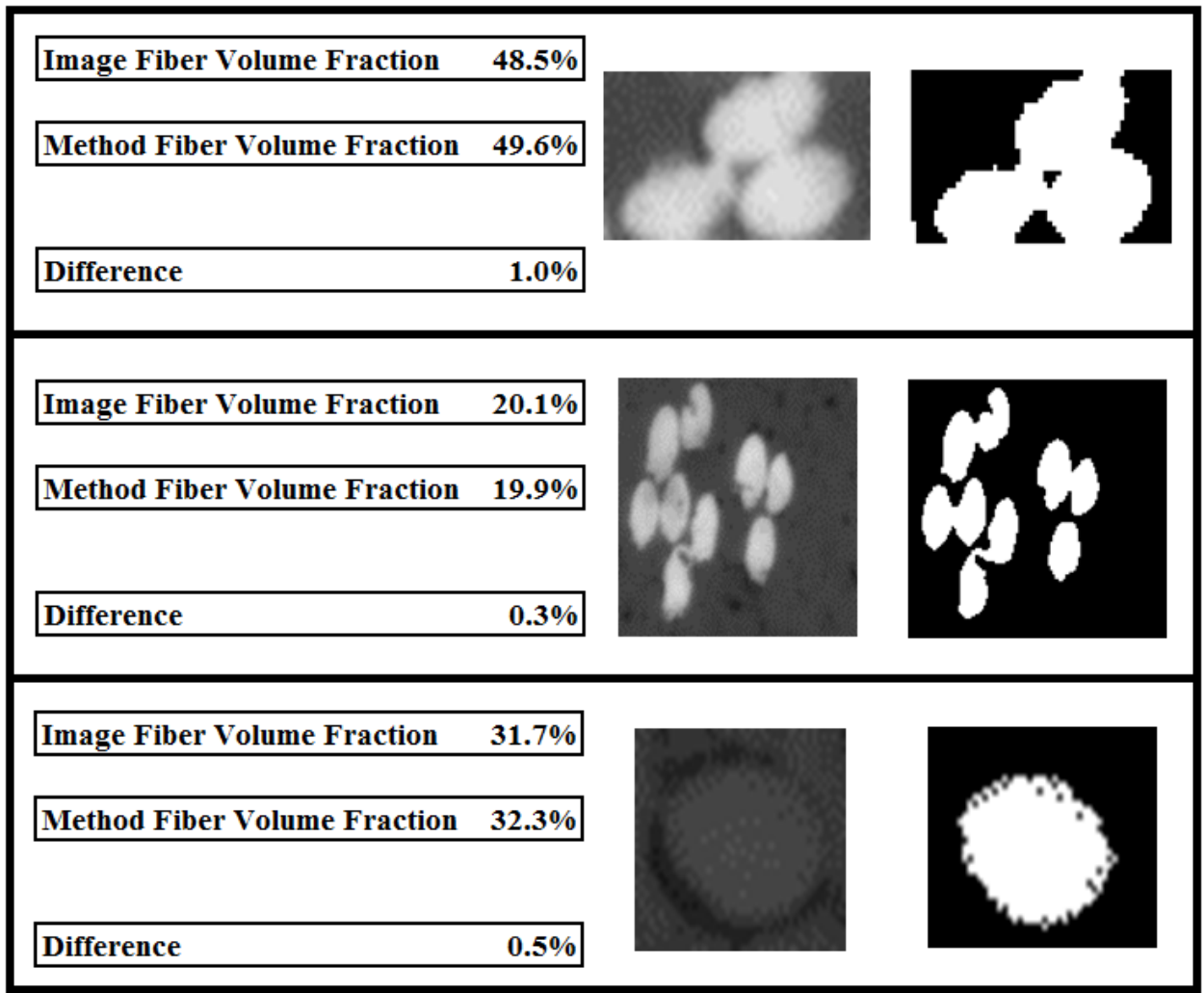


Figure 4.9: Accuracy of Binary Image Fiber Volume Fraction Methodology- Image Set 2

region underwent an additional segmentation process, there was a concern that the segmentation would lead to inaccurate results. However, this image shows that with a proper segmentation of the binder region, a very accurate approximation of the fiber volume fraction was obtained.

CHAPTER V

FINAL SERIAL SECTIONING

5.1 Sectioning Angle and Segmentation Considerations

Upon completion of the serial sectioning of the first specimen, it was ultimately determined that the fiber volume fraction variation methodology was feasible for the warp and weft tows. However, at this point, it was determined that the FVF in binder tows would no longer be investigated in this study. Given the scope and the time constraints of the study, it was too difficult to accurately and effectively implement fiber volume fraction variation in the binder tows of the computational model.

The primary issue with capturing the FVF variation in the binder tows was caused due to the complex angle of the original serial sectioning. Since the orientation and geometry of the binder tows substantially changed throughout the length of the tow, the cross-sectional shape of the tows and the orientation of their respective fibers changed in each successive image slice. This then made it difficult to implement fiber volume fraction variation data in the model of the binder tows. Cross-sectional depictions of the binder tows differed greatly from the model's cross-sections both in shape and relative location. Furthermore, determining the physical point in the specimen that the image of the binder tow was depicting was no simple task; though the sectioning plane was known, the physical orientation and geometry of the tow that the corresponding image was depicting was not. The orientation could have been theoretically estimated by investigating the shape and orientation of

the fibers within the binder tows or through micro-CT imaging data, but this was ultimately deemed outside the scope of this study. Furthermore, the complex angle at which the original specimen was sectioned made the analysis of the warp and weft tows more difficult. In these images it was difficult to understand which tow in the specimen one was looking at. In addition, there were more complications involving physical specimen coordinates as they related to their image representations (though these were easier to determine than with binder tows). Considering all of these factors, it was determined that the study would focus on accurately capturing fiber volume fraction variation data in only the warp and weft tows from this point forward.

After the methodology development discussed in Chapter IV, it was determined that the images obtained from the serial sectioning of the second specimen would be segmented with the EM/MPM algorithm instead of thresholding. The Poisson noise for these high resolution images were apparent in the images, which would lead to inaccurate results if simple thresholding was utilized. Although segmentation would be much more time consuming than thresholding, it was determined to be necessary for accurate results.

5.2 Specimen Preparation

The serial sectioning of the second dog-bone specimen was performed at a 45 degree angle in the plane of the composite. Utilizing this angle allowed for the identification of individual fibers for both warp and weft tows in each image slice. Furthermore, this angle was simple enough to effectively relate the image coordinates to their corresponding physical locations in the specimen.

To prepare the sample for serial sectioning, the sample was set in place inside a resin plug. The sample next to the plug mold for serial sectioning is shown in Figure 5.1. For this serial sectioning, the dog-bone sample was cut such that the gage section was at the bottom of the resin plug. This allowed the Robo-Met 3D system to directly image the gage section without having to remove excess sample. For the imaging of this second specimen, the angle of the sectioning was much



Figure 5.1: Specimen and Plug Mold for Serial Sectioning

more precise than the preliminary serial sectioning. To accomplish this precision, an aluminum guide was fashioned—courtesy of Arthur Safriet (AFRL/RXAN), so that the sample could easily be cut on an IsoMet diamond blade saw. The sample and guide fixture are shown in Figure 5.2

After the specimen was cut, the specimen was placed in a clip such that the now-angled gage section laid flush against the cap of the plug mold. The angle of the specimen was measured again to ensure an angle of 45 degrees was obtained. The mold was then covered with a release agent so that the resin plug could easily be removed from the plug after the resin had solidified. The sample was super glued to the mold so that the sample stayed at the proper angle during resin infusion. After the super glue had set, resin was poured into the plug mold and left at room temperature to cure over night. The plug was then removed from the mold after the resin had fully cured. The plug utilized for serial sectioning imaging is shown in Figure 5.3.

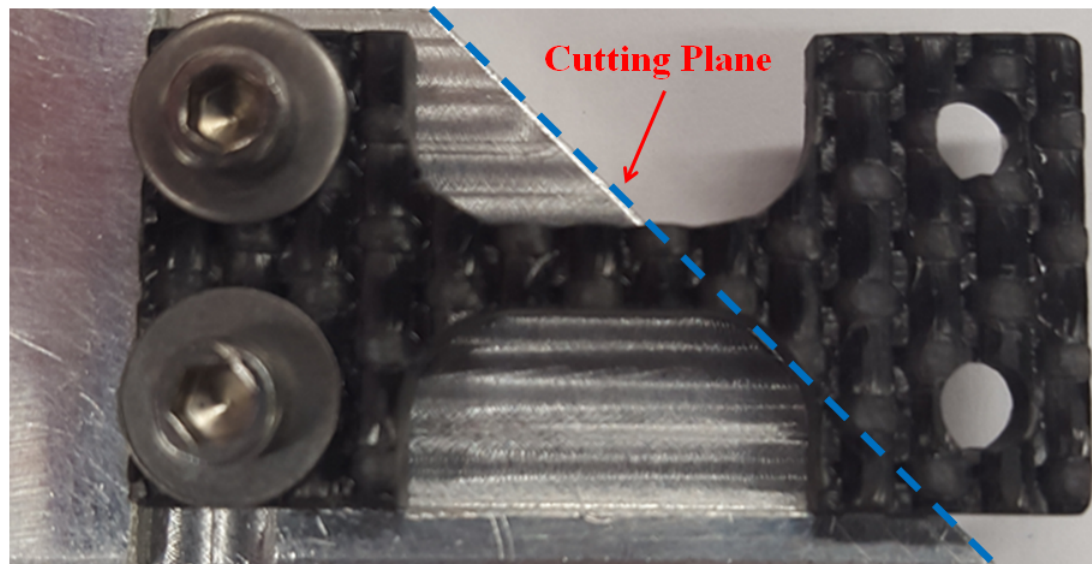
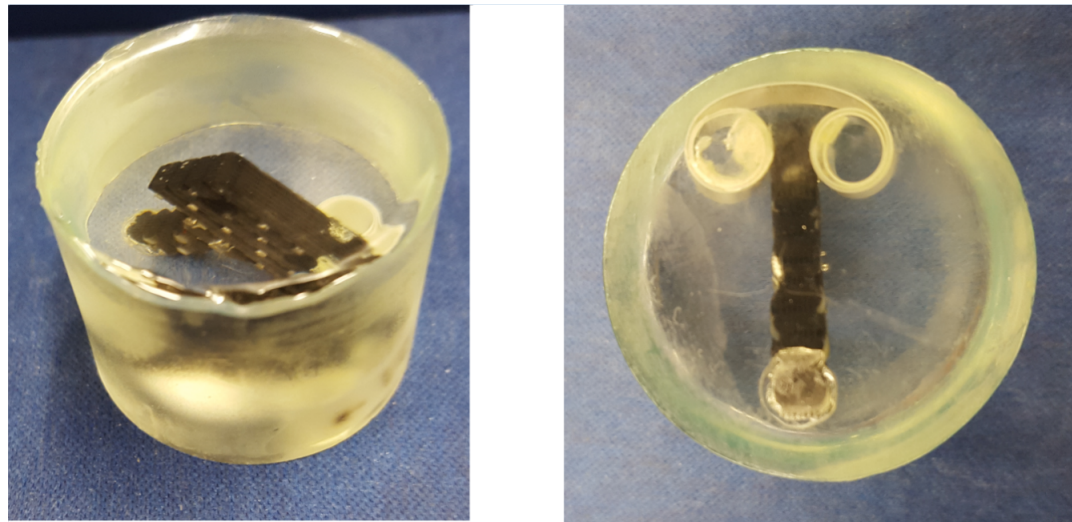


Figure 5.2: Specimen and Guide Fixture for Diamond Saw Cutting



Side View

Top View

Figure 5.3: Plug Utilized for Serial Sectioning

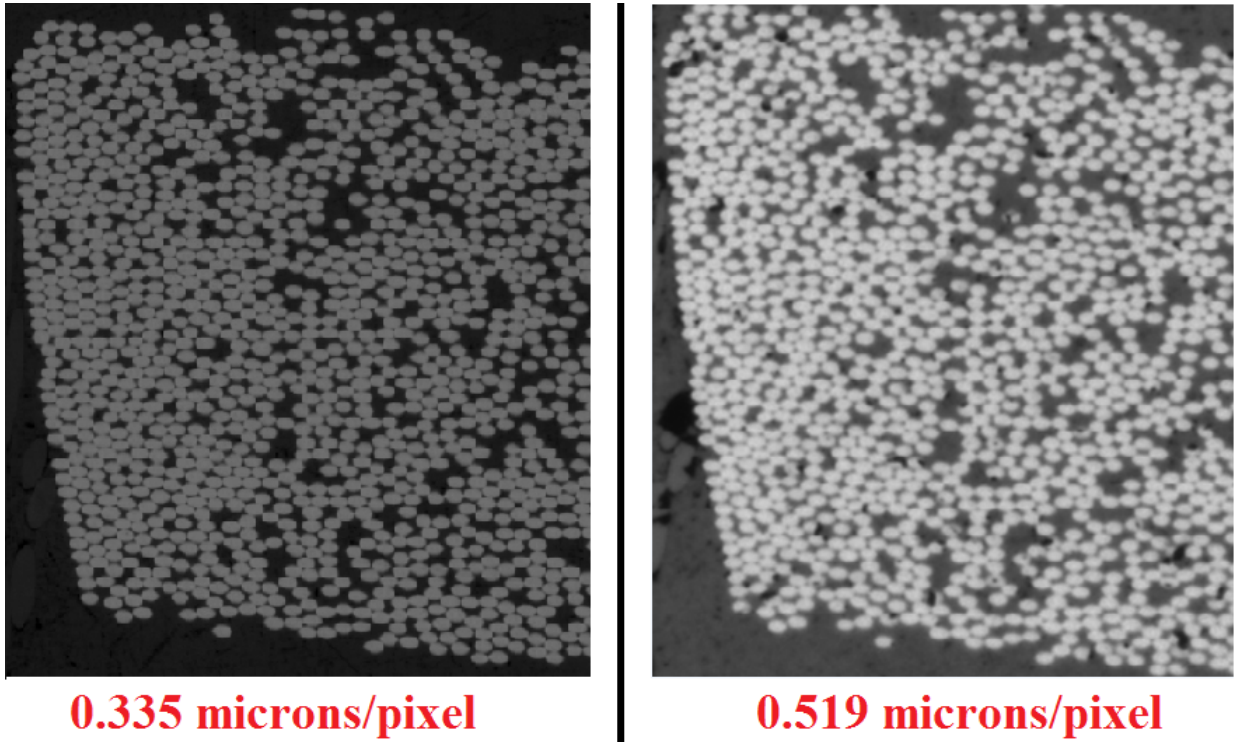


Figure 5.4: High and Low Resolution Comparison

5.3 Resolution Determination and Segmentation Parameterization

Preliminary imaging was performed on the specimen to determine a proper resolution for the imaging of the specimen. Two resolutions were tested: 0.335 microns per pixel (the highest resolution that could conceivably/feasibly be taken) and 0.519 microns per pixel. Images were taken at a very small image slice step size (approximately 1.79 microns per image slice) so that relatively similar points in the material could be compared. A comparison of these image resolution test images is shown in Figure 5.4. This figure indicates that the higher resolution provided a much better definition of individual fibers. This was due, not only to the fact that the resolution was higher, but also due to a difference in the lenses utilized for the images. The higher resolution image was captured by utilizing a higher quality lens that more accurately resolved features of the specimen.

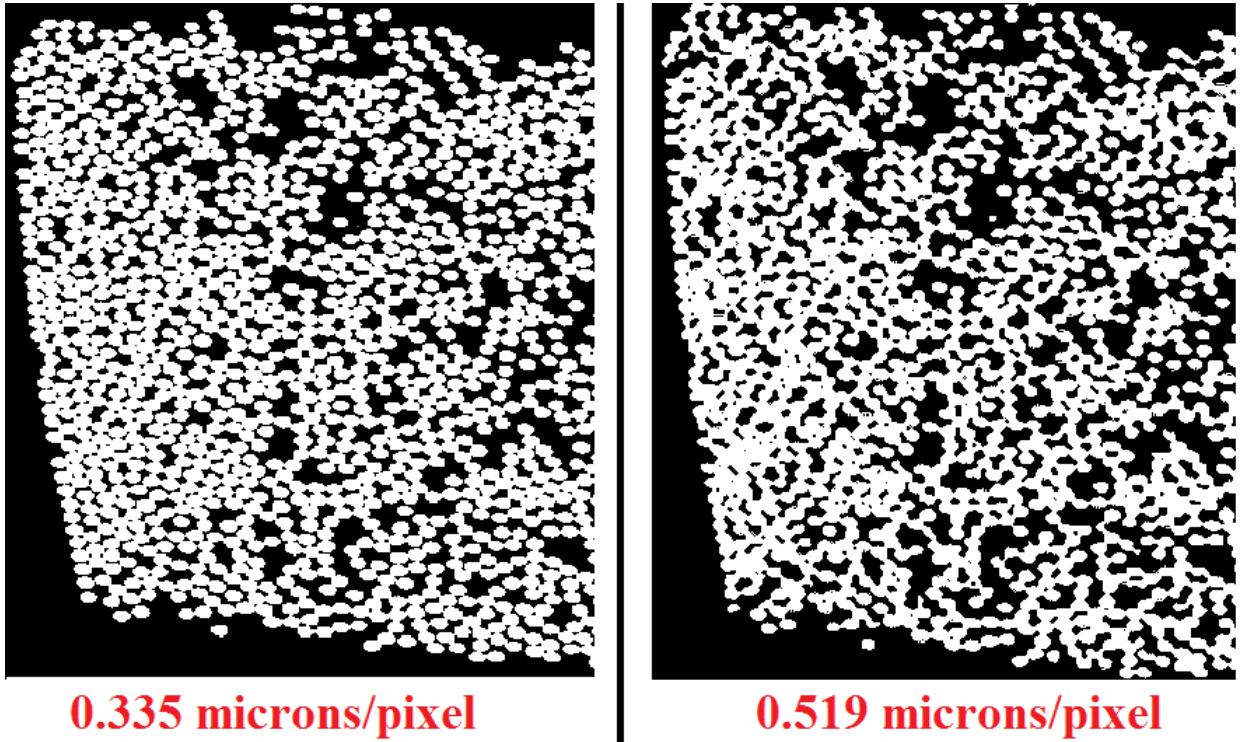


Figure 5.5: High and Low Resolution Comparison- Segmented Images

In other words, the high quality lens did a better job of determining whether a pixel was fiber or matrix (or something else entirely), and then assigning a color appropriately. However, from this comparison alone, it was difficult to determine if the lower resolution was significantly worse than the higher resolution image.

To investigate the differences between the resolutions further, the two images were segmented with the EM/MPM. The results of this comparison test are shown in Figure 5.5. From this figure, it is clear that the lower resolution led to a segmentation that did not adequately classify matrix and fiber regions. This was especially true when analyzing areas with high fiber densities; these regions appeared as nearly continuous fiber regions instead of individual fibers. This problem became more inherently obvious when analyzed at the pixel level as shown in Figure 5.6. The 0.335 micron per pixel image clearly showed well defined fibers, while the 0.519 micron per pixel image failed to

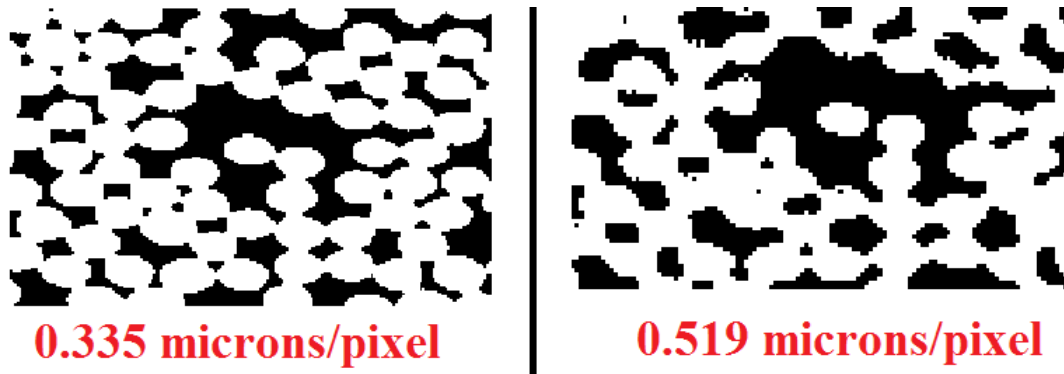


Figure 5.6: High and Low Resolution Comparison- Segmented Pixel Level Zoom

depict the features typical of a carbon fiber tow. The low resolution image incorrectly classified more pixels than the high resolution image. Once again, this was most prevalent in areas of high fiber densities. Judging from this analysis, it was clear that it was necessary to collect images at the higher resolution of 0.335 microns/pixel.

After the resolution was chosen, it was then necessary to define the specific parameters to be utilized in the EM/MPM segmentation algorithm. This was mostly a trial-and-error process; however it was known that the exchange energy between the white and black pixel classifications should be low to minimize the possibility of white fiber pixel regions incorrectly growing and overtaking the black matrix regions. After proper calibration of the segmentation, the parameters were determined to be as follows:

- **Exchange Energy-** 0.01
- **Histogram Loops-** 15
- **Segmentation Loops-** 15
- **Simulated Annealing-** On
- **Gradient Penalty-** Beta E = 1.00

For an in depth explanation of these parameters, see Comer et al [41, 42, 43].

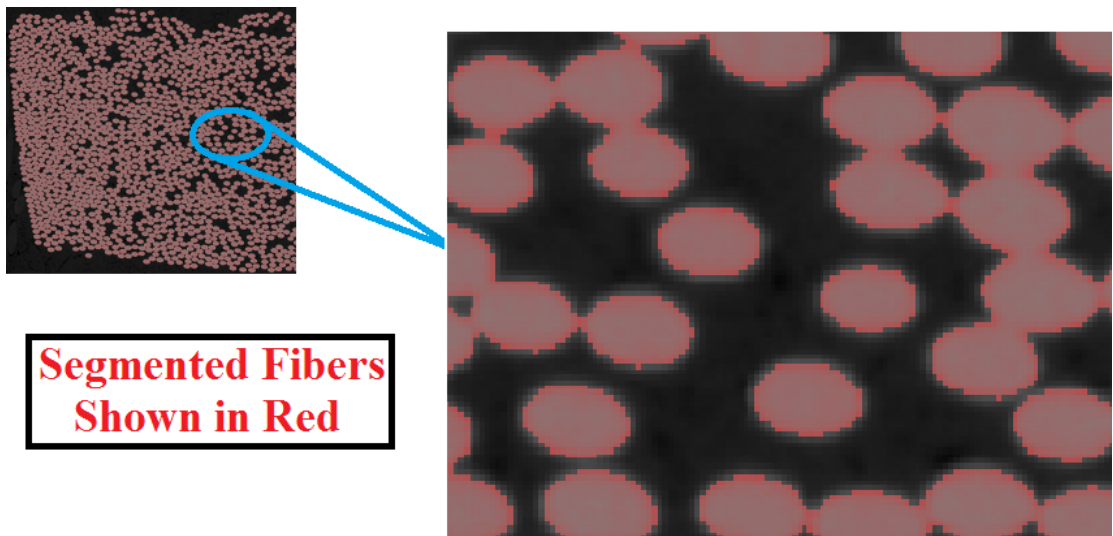


Figure 5.7: Segmented and Raw Image Overlay Comparison

The result of utilizing these parameters was a segmentation that classified matrix and fiber regions with adequate accuracy. An overlay of the segmented image and the original raw image data is shown in Figure 5.7. In this figure, an exclusion overlay algorithm was utilized to showcase the differences between the original image and the segmented image. The color of the fibers in the segmented image was set to a shade of red to better highlight the differences between the segmented fibers and the gray fibers of the original image. As can be seen in Figure 5.7, the segmented fibers almost perfectly aligned with the original image fibers. There appeared to be a small amount of excess gray area around the edge of the fibers; these areas could have been fiber areas, or they could have been due to a lighting effect in the image. In addition, there was still some bridging seen between the segmented fibers which led to incorrect fiber pixel classification. These areas were relatively small, however, and did not seem to drastically affect results. When considering this as well as the fact that the segmented fiber regions were possibly smaller than their true value, these two effects may have theoretically canceled each other out. All things considered, the segmentation was

shown to accurately represent the original image and was deemed viable for fiber volume fraction variation analysis.

5.4 Image Analysis and Preparation

Considering that the higher resolution was necessary for serial sectioning, the amount of specimen volume that could be examined was drastically limited. It was determined that the distance between image slices should be fifty microns (this is considered relatively large by Robo-Met standards), meaning that five millimeters in depth of the material would be examined. Considering the angle of cut of the specimen and the required polishing, this meant roughly the entire gage section would be analyzed. This was determined to be a large enough volume to be indicative of the fiber volume fraction variation throughout the entirety of the specimen. However, two and a half hours were needed to obtain one image at 0.335 micron/pixel resolution and 100 images were desired. This delayed obtaining high resolution data since the technician had to set aside approximately one week for serial sectioning for this study.

Figure 5.8 depicts the first image obtained from the serial sectioning of the second specimen (note that this picture has been considerably compressed in order to be properly imaged on the page). This image clearly shows an angled cross-section of the composite specimen. For clarity, the serially sectioned image has been superimposed on top of a micro-CT image in Figure 5.9. With this serial section methodology, it was much easier to determine what portion of the specimen was under examination. Furthermore, the serially sectioned image matches what had been observed during CT imaging, showcasing the viability of the technique.

Figure 5.10 depicts the fiber makeup of the upper weft tows in the composite. Note, that the bottom weft tows were symmetric in fiber makeup about the fourth weft tow. The bottom tows therefore are not shown in detail, but were named weft tows numbers five, six, seven, and eight, respectively. By examining the first tow in Figure 5.10, it appeared that the fibers in this tow were the

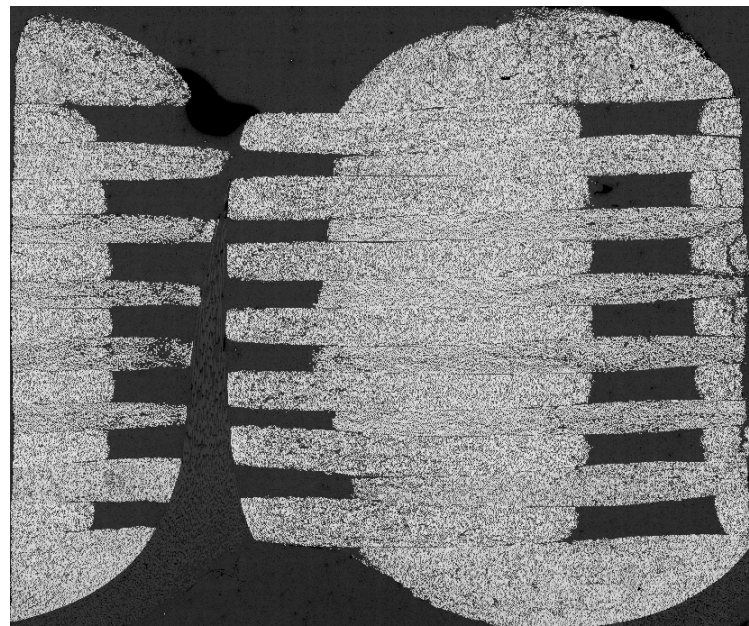


Figure 5.8: High Resolution Cross-Section of Second Specimen

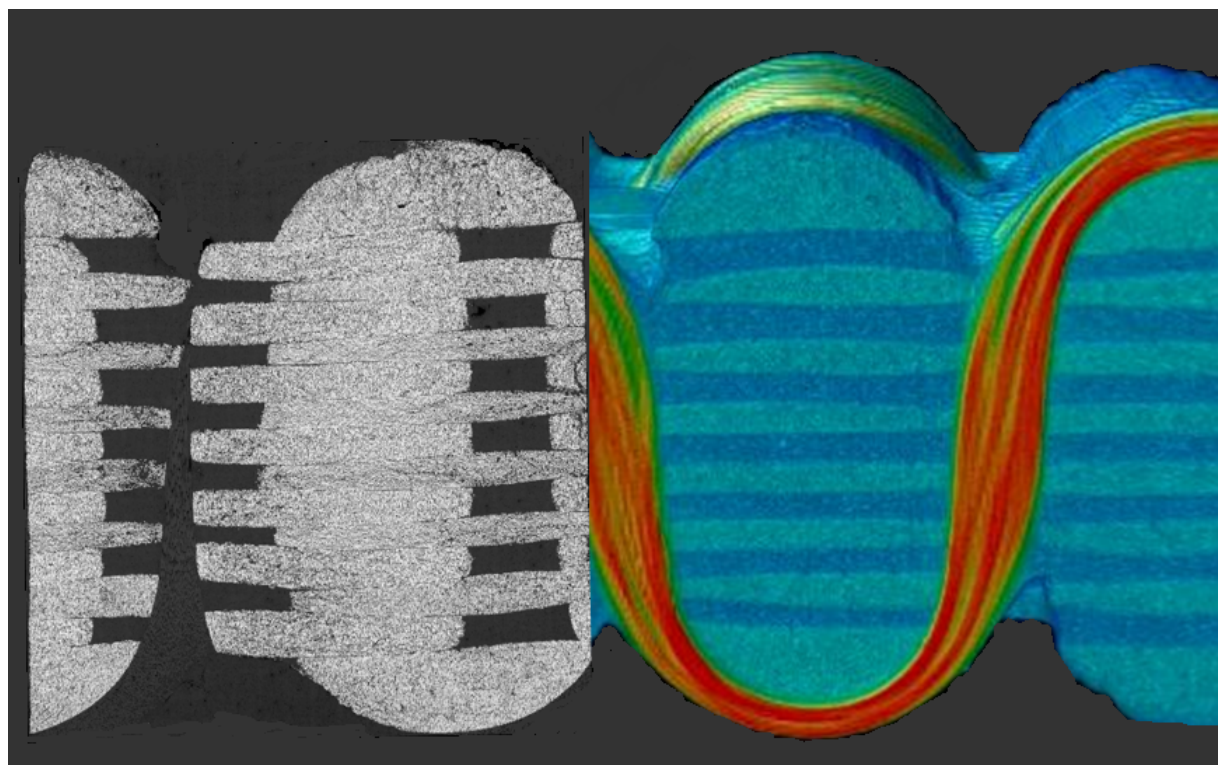


Figure 5.9: Serially Sectioned Image Superimposed on Micro-CT Image

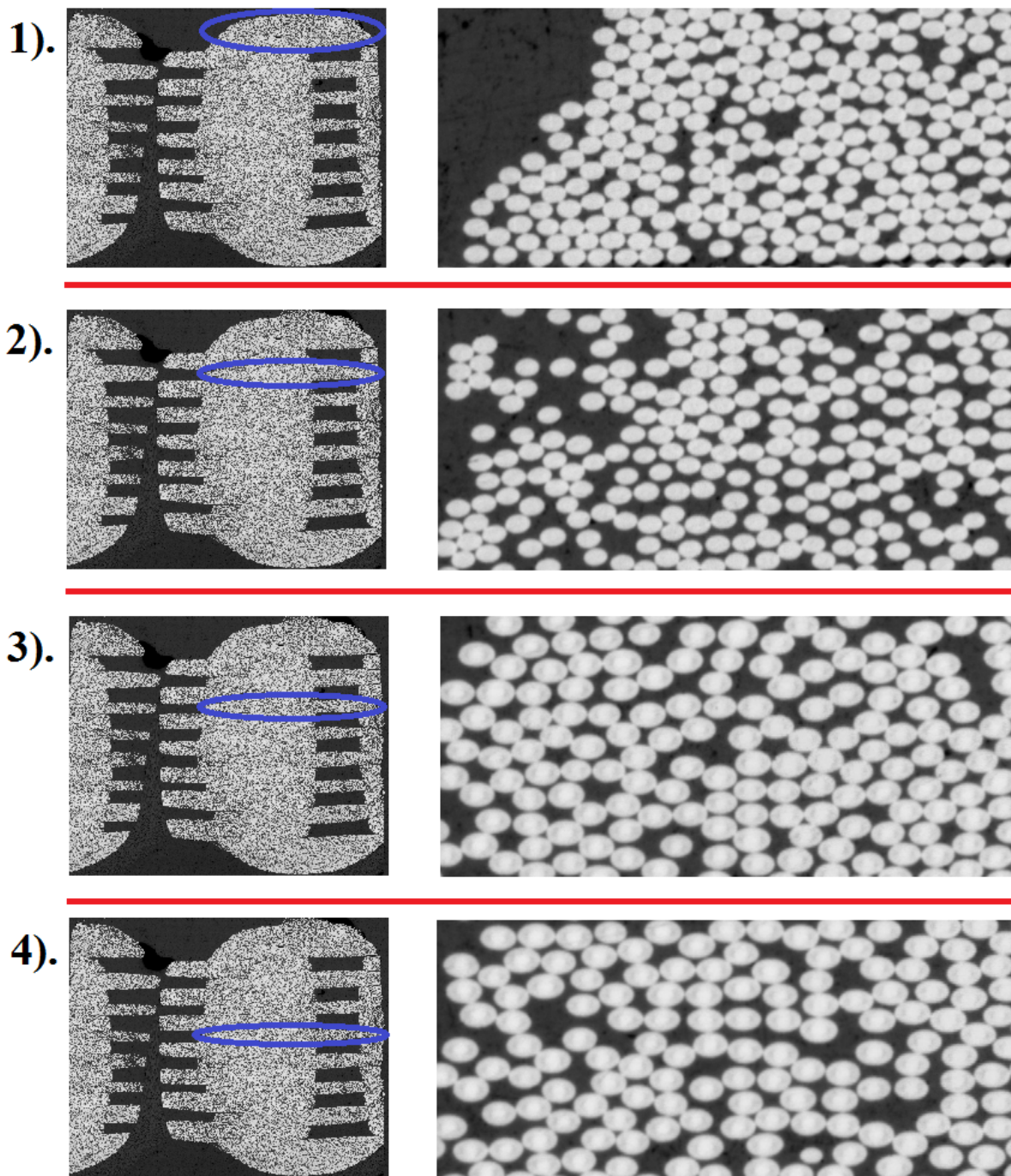


Figure 5.10: Fiber Makeup of Weft Tows

same size as the fibers in the second weft tow. This observation indicated that the hemi-cylindrical shape of the top and bottom tows was not due to the fiber makeup of the tows. This geometrical difference was likely due to a difference in pressure between the inner and outer tows. When examining the third and fourth weft tows, it was clear that these tows were made of considerably larger fibers than the fibers seen in the first and second weft tows. This was somewhat surprising considering the third and fourth tows were geometrically similar to the second weft tow. In this instance, the fibers within the tow did not have a great effect on the overall geometry of the tow. From these images and what was known from data provided by the manufacturer, it was determined that the tow makeup was as follows:

- Weft Tows 1, 2, 7, and 8- IM7 6k
- Weft Tows 3, 4, 5, and 6- AS4C 3k
- Warp Tows- IM7 12k

The width of the warp and weft tows and the dimensions of the fibers within the respective tows were measured to approximate the true angle of the imaging of the specimen. Due to the high variability of the height of the tows throughout the specimen, an average height value was not measured. The average widths of the weft and warp tows were 2.60 and 2.25 mm, respectively. Considering the original measured width of the tows was approximately 1.7 mm for both warp and weft tows (although the methodology for obtaining these measurements was likely fairly inaccurate), it was clear that the angle of the cut/imaging was not perfectly 45 degrees. If the cut was truly 45 degrees, then the warp and weft tows would have theoretically appeared to have the same width.

After the lengths of the warp and weft tows were measured, individual fiber dimensions within the tows were measured and recorded. Assuming that the orientation of the fibers was such that they were approximately the same orientation as the tows they were within, the angle of the cut was determined to be approximately 48 degrees.

CHAPTER VI

VTMS METHODOLOGY

The Virtual Textile Morphology Suite (VTMS) was the primary software package utilized to model the 3D textile weaves. VTMS consists of five modules:

- Textile Module
- Relaxation Module
- Tow Modification Module
- Mesh Generator Module
- BSAM Export Module

This chapter is devoted to explaining how each of these modules was utilized to obtain a finite element model that was usable in BSAM. This chapter outlines the general process used to generate the preliminary model of the 3D textile PMC specimens used in this study.

6.1 Textile Module

The Textile Module of VTMS was utilized to obtain an approximate model of the textile fabric weave prior to variability induced by manufacturing effects. To obtain this model, first the correct orthogonal weave pattern was chosen. VTMS then generated an idealized orthogonal weave preform model with the specified dimensions shown in Figure 6.1. At this point, the model was idealized in the sense that tows were modeled as a chain of rod elements with a consistent circular cross-section. A depiction of the idealized fabric model output from VTMS is shown in Figure 6.2.

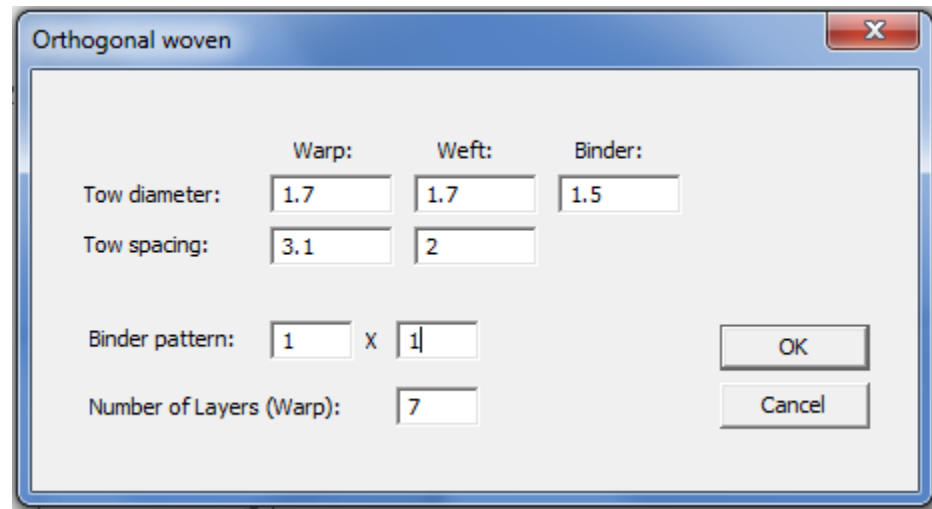


Figure 6.1: Fabric Parameters- VTMS Input

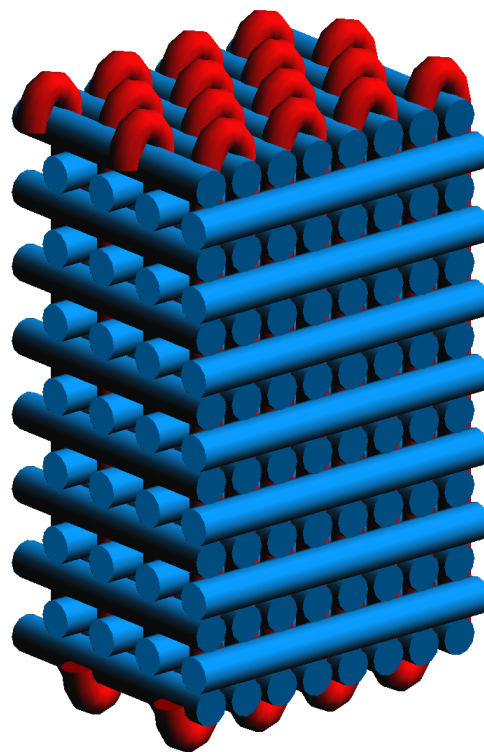


Figure 6.2: Specimen Preform Model with Idealized Tows

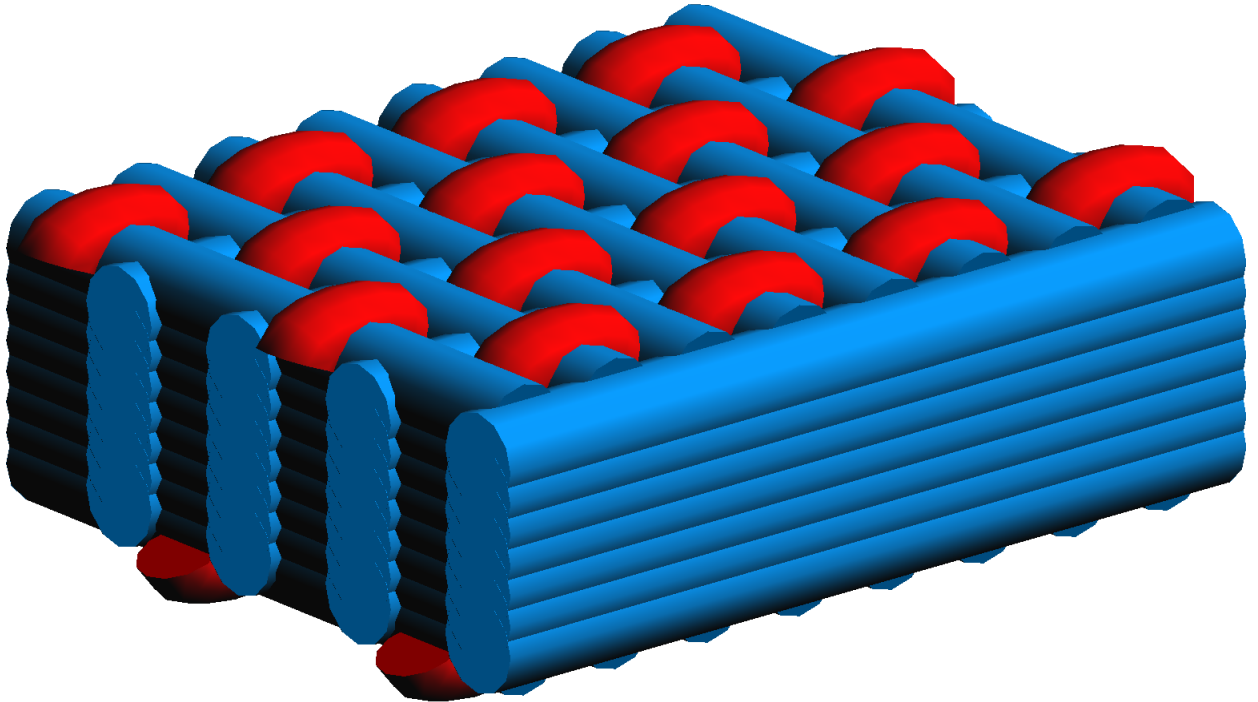


Figure 6.3: Scaled and Tessellated Preform Model

After obtaining the idealized Representative Volume Element (RVE), the RVE was tessellated four times in the x -direction and twice in the z -direction. After tessellation, it was noted that the model was approximately 29 mm thick; this thickness was significantly larger than the measured fabric preform thickness of 3.175 mm. To resolve this issue, the model had to be scaled to a smaller size in the y -direction to approximately match the measured thickness. The warp and weft direction tows were scaled by a factor of 0.16, while the binder tows were scaled by 0.18. The binder tows were scaled by a slightly larger factor than the warp and weft tows to avoid interpenetration created by the scaling function. The result of this scaling and tessellating is shown in Figure 6.3.

After the idealized tows were properly defined, each of the tows was fiberized. Fiberizing is a convention created by VTMS that takes idealized tows and converts them into a bundle of fibrils (also referred to as digital fibers). Each fibril is composed of 1D rod elements to create a wireframe

model that follows the path of the tow. Fibrils represent fibers in a physical tow and allow for variation in the model tow geometry within the Relaxation Module. When fiberization is used, the tows keep their original diameter and the algorithm assigns that value as the overall tow width. Individual digital fiber size then scales based on the number of defined fibrils in the tow. Although the width of the tow remains the same, the height of the tows is dependent upon how many fibril layers the user defines. For the dog-bone specimen model, the warp and weft tows were fiberized such that there were ten fibers in the 0 degree direction (width) and two fibers in the 90 degree direction (height). Since the original tow diameter was 1.7 mm for warp and weft tows, the new tows kept this width parameter. The diameter of the fibrils was therefore the original diameter (1.7 mm), divided by the number of fibrils in the width (10 mm); the diameter of the fibrils was 0.17 mm. VTMS assumes an idealized hexagonally packing sequence for fibers in a tow such that each layer away from the centerline of the tow has one less fiber in the row. Since the warp and weft tows had two layers with ten fibrils in the centerline, there was a row above it with only nine fibrils; the total number of fibrils in each warp and weft tow was 19.

Due to the packing structure, the new tow height was more difficult to obtain. Furthermore, upon close inspection of the digital fibers, the fibers were not perfectly circular. Instead they were visualized as regular dodecagons with the packing scheme shown in Figure 6.4. Considering this, simple trigonometric principles were manipulated to determine an adjusted fiber height– the fibril height that contributes to the overall height of the tow. Additionally both an inner and outer fibril height was defined; the outer fibril height was defined as:

$$radius + radius * \cos(2\pi/12)$$

and the inner fibril height as:

$$2 * radius * \cos(2\pi/12)$$

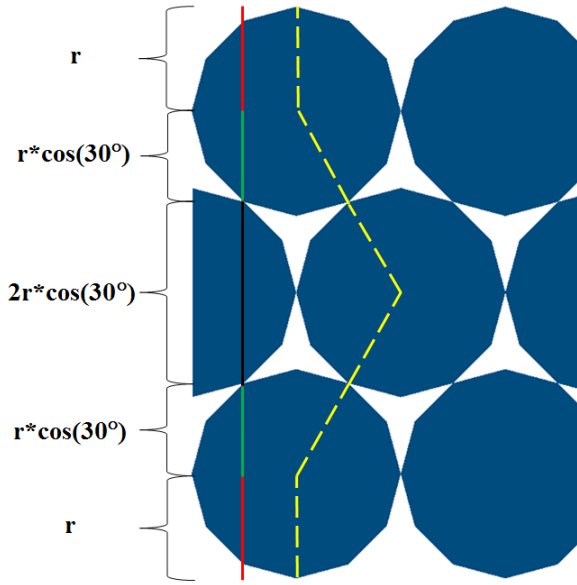


Figure 6.4: Digital Fiber Geometry and Packing Scheme

These warp and weft tows only had outer fibrils which were calculated by:

$$\frac{0.17}{2} * \left(1 + \cos\left(\frac{2\pi}{12}\right)\right) = 0.1586$$

Then by simply multiplying this by the number of outer fibrils in the tow, the new height of the tow was obtained:

$$0.1586 * 2 = 0.3172$$

Fiberization in the binder tows consisted of twelve fibrils in the 0 degree direction and four fibrils in the 90 degree direction. The new parameters were calculated in the same manner as was conducted for the warp and weft tows. Firstly, the diameter of the fibrils was defined as 0.125 mm. There were two inner fibrils and two outer fibrils in the binder tows with adjusted heights of 0.1166 mm and 0.1083 mm, respectively. This led to a tow height of 0.4498 mm for binder tows. Because there were four layers in the binder tow and twelve fibrils in the centerline of the tow, there were

$12 + 11 + 11 + 10 = 44$ fibrils in each binder tow. A depiction of the idealized and fiberized tow cross-sections is shown in Figure 6.5

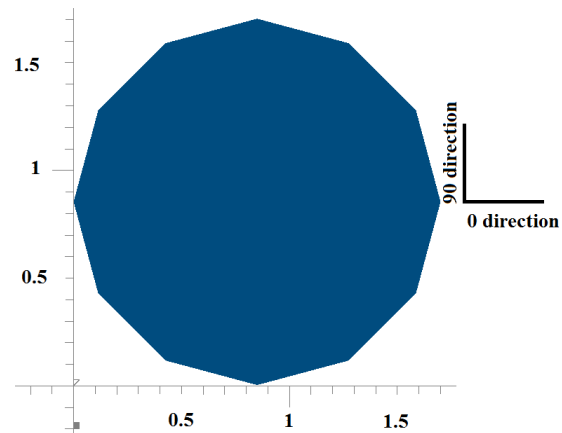
After the tows were fiberized, the mesh of the tows was refined based on the size of the new fibrils. The original mesh density was relatively coarse since it was based on the original large tow, and if this density was kept, the fibrils would have interpenetrated each other when they underwent dynamic relaxation. The mesh was therefore refined such that the ratio of the length divided by the diameter of the fibrils was equal to 0.5. After fiberization and mesh refinement was complete, the fabric model was a collection of tows made up of rod element fibrils, which is depicted in Figure 6.6.

6.2 Relaxation Module- General Features

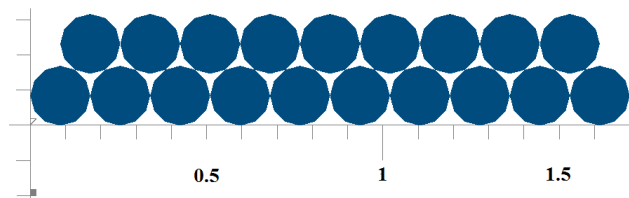
The Relaxation Module uses a one dimensional rod finite element method that is used to induce variability in the fabric model. This section describes various features of the Relaxation Module and the typical techniques utilized to generate a relaxed preform model. Creating a relaxed fabric preform model in the Relaxation Module can be completed in a variety of different ways and often takes many relaxation cycles. Therefore, the specific steps used to generate the relaxed preform model of the dog-bone specimen gage section are not discussed; instead a very brief outline of the process that was used is provided in Section 6.3.

For a general model, a fiberized fabric is brought into the Relaxation Module and boundary conditions are applied to individual fibrils. Generally, boundary conditions are set on a tow basis where every fibril in the tow exhibits the same boundary conditions; however, varying boundary conditions can be applied to individual fibrils within a tow if necessary. With the boundary conditions set, the fabric can now be “relaxed”— the designated term for running the finite element model in the Relaxation Module. Relaxing the textile runs an algorithm that seeks to minimize the energy within individual fibrils to the point where the fibrils reach a steady state. In addition to boundary

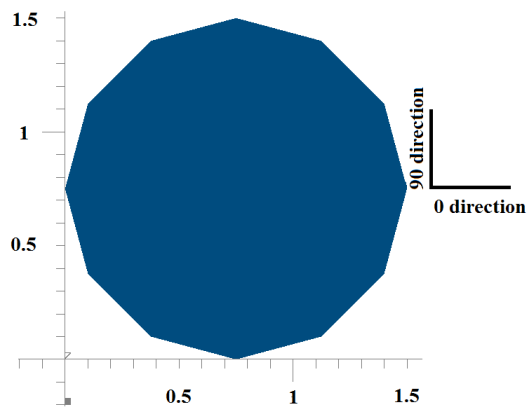
Original Warp or Weft Tow



Fiberized Warp or Weft Tow



Original Binder Tow



Fiberized Binder Tow

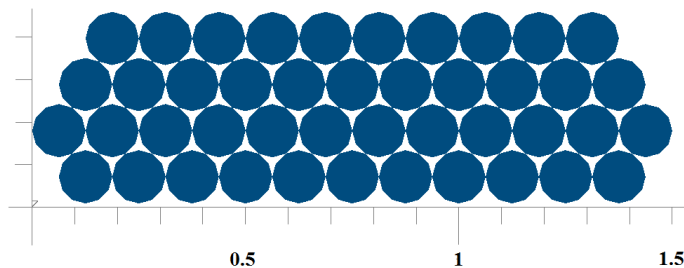


Figure 6.5: Idealized and Fiberized Tow Cross-Sections

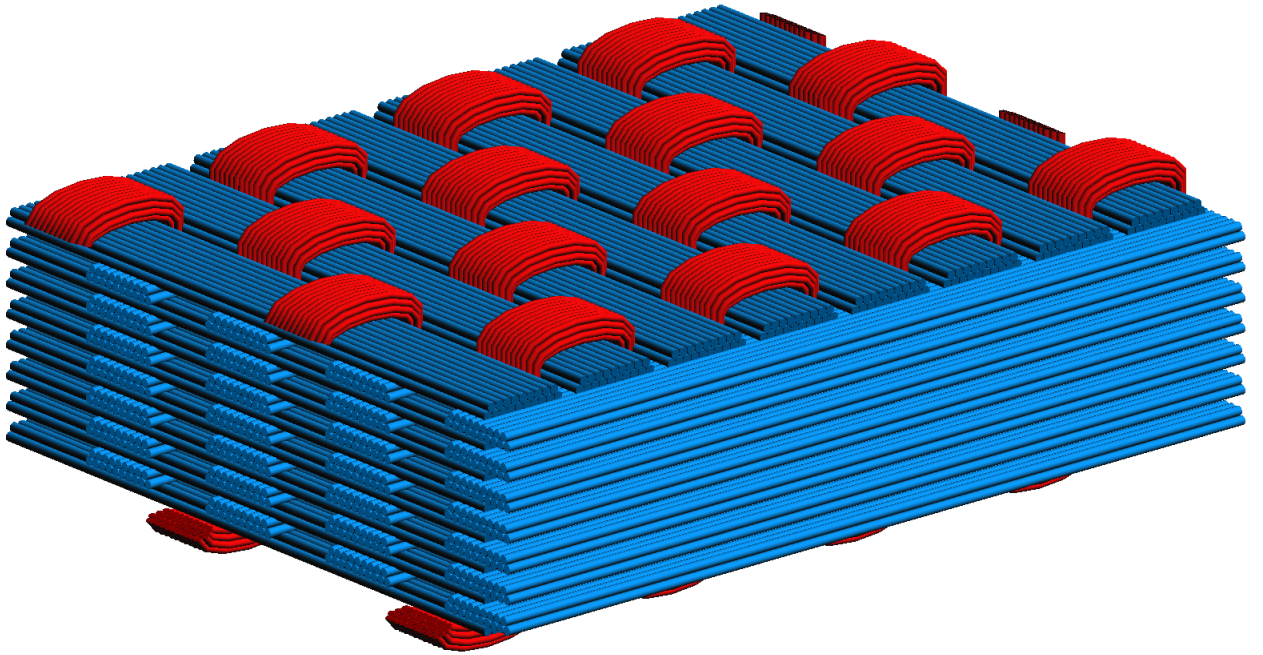


Figure 6.6: Preform Model with Fiberized Tows

conditions, the algorithm applies two important conditions to the fibers: material stiffness and tension. Both of these are relative conditions in the sense that they are not physical properties, but are simply utilized to modify the way fibrils interact with one another within the algorithm. The material stiffness determines the relative flexibility of the rod elements; the higher the stiffness of the fibril, the less it will move due to loading and force from other fibrils. Tension on the other hand, applies loads to the ends of the digital fibril chain such that the fibril is pulled towards a straight state. A high tensile force can be used to smooth wrinkles developing along the fibril chain or can also be used as another means of preventing deformation due to loading or other fibrils.

The relaxation algorithm must solve a fairly complicated problem considering fibrils have to interact with each other so they do not pass through one another. To overcome this issue, the Relaxation Module utilizes two methods: damping and contact elements. Damping is a way of slowing down the algorithm such that the fibrils do not immediately go to a state where fibrils have

already passed through one another. Because of this, a textile is often relaxed multiple times before a desired textile model is produced. For the initial relaxation, damping is usually set to an arbitrarily high value. The model is at its most volatile state before the first relaxation, since at this point no contact elements have been created meaning that the algorithm has no way of knowing whether or not fibrils are touching each other. As more contact elements are created and as the fabric moves closer to a converged state, the damping value can be decreased. Most fabrics require well over 20 relaxation cycles before a desired model is obtained.

The second aspect of the Relaxation Module that prevents fibril interpenetration is the creation of contact elements. Contact elements are essentially elements that are added to the model that connects a node from one fibril to a node in another. When the position of a node of a fibril comes within a user defined tolerance of a node in another fibril, a contact element is created. This element is a small rod element that restricts the motion of the two nodes such that the nodes move together. As more contact elements are created, the degrees of freedom in the model decrease, therefore increasing the speed of the model. Since nodes connected by a contact element cannot interpenetrate, the degree of damping can be decreased after more cycles are completed. It should be noted that contact elements are only added to the model for use in the Relaxation Model. In other words, the contact elements are not included in the model that is exported to other modules within VTMS.

Another unique aspect of the Relaxation Module is the ability to add virtual molds to the model. A mold is simply a mesh of 1D rod elements connected together to form a rectangular plane, an example of which can be seen in Figure 6.7. Boundary conditions can then be set accordingly in order to simulate the type of mold that was utilized in the manufacturing process of the composite. To model a flat plate or platen, the user simply restricts the nodes of the molds in the in-plane directions. An out of plane displacement boundary condition can then be applied to the nodes which

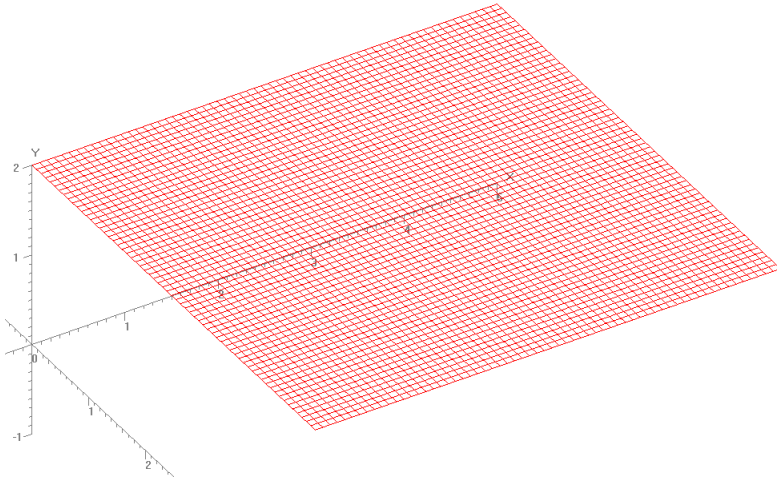


Figure 6.7: Depiction of a Mold Utilized in the Relaxation Module

creates a rigid mold where the fibrils are pushed downwards by the force of the mold. Likewise, to model a vacuum bag process, the user simply does not apply boundary conditions in the in-plane directions, creating a flexible mold that can contour to the geometry of the fibers. The material stiffness of this type of mold is usually set to be higher than the stiffness of the fibers in order to prevent the mold from deforming more than the fibers. Molds can be effective in flattening fabrics to a specified height, but the overuse of this can cause interpenetration between the fibrils.

6.3 Relaxation Module- Orthogonal Weave Preform Generation

The fiberized model of the orthogonal weave preform was imported into the Relaxation Module. Rigid molds were also imported into the module and were set above and below the fabric preform model. These two molds were used to compress the preform similar to the platen process used in the experimental methodology described in Section 3.1. Warp, weft, and binder tows were all held fixed in their respective fiber directions. In addition, boundary conditions were applied to the warp tows such that they were moved towards the binder tows. Doing this induced variability in the binder tows. Finally, arbitrarily large tensions were applied to both warp and weft tows to ensure that their

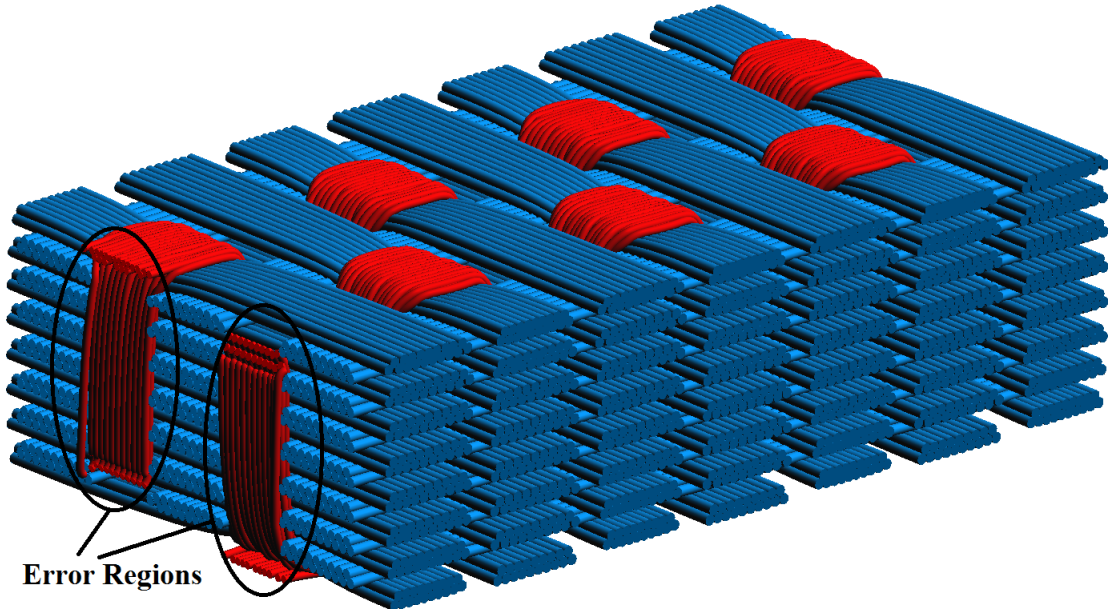


Figure 6.8: Fully Relaxed Textile Preform Model

geometric variability was less than the binder tows. The fully relaxed preform generated from this process is shown in Figure 6.8.

Notice that this relaxed preform had a much higher degree of inter-tow variability compared to the preform shown in Figure 6.6. Furthermore, the binder tows were more closely wrapped around the top layer of weft tows and created some compaction around the areas where the binder tows and weft tows met. In addition, both the warp and weft tows had a greater amount of spacing between digital fibers, but they had generally maintained their original geometry shown in Figure 6.6. However, there was a high degree of error in the model at the edge of the tows. This is a fairly typical result from the Relaxation Module and is due to the interaction between the compression of the preform, the varying tension in the digital fibers, and the relaxation of the fibrils. It was therefore necessary to start with a preform that was larger than the desired final model. The preform was cut to the desired size of the final model so that it matched the size of the dog-bone specimen gage section. This cut and fully relaxed preform is shown in Figure 6.9

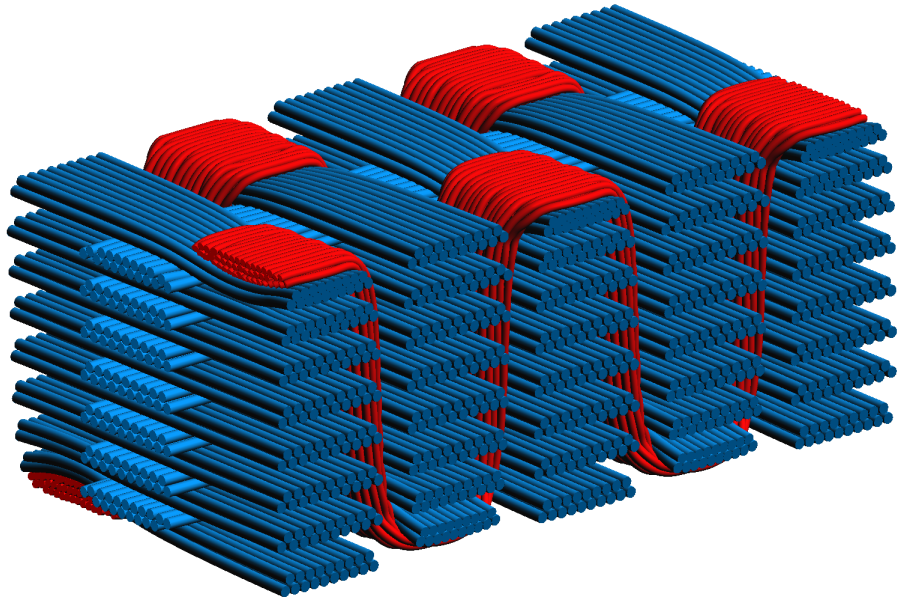


Figure 6.9: Relaxed Preform Cut to Size of the Dog-bone Specimen Gage Section

6.4 Tow Modification Module

After the preform model of the dog-bone specimen had been made, the next step was to convert this to a finite element model. In order to accomplish this, a surface mesh was needed prior to generating a three-dimensional mesh. The Tow Modification Module in VTMS was utilized to generate surface meshes of individual tows. Since BSAM uses the Independent Mesh Method, a mesh had to be generated for each individual tow in the fabric model.

First, “regular” tows were generated. To obtain regular tows, two parameters had to be defined: slices and stacks. Slices are the nodes on the boundary surrounding the cross-sections of the tow, while stacks are simply the cross-sections along the length of the tow. The defined parameters for regular tow generation were as follows:

- Warp- 64 slices and 119 stacks
- Weft- 64 slices and 61 stacks
- Binder- 32 slices and 160 stacks

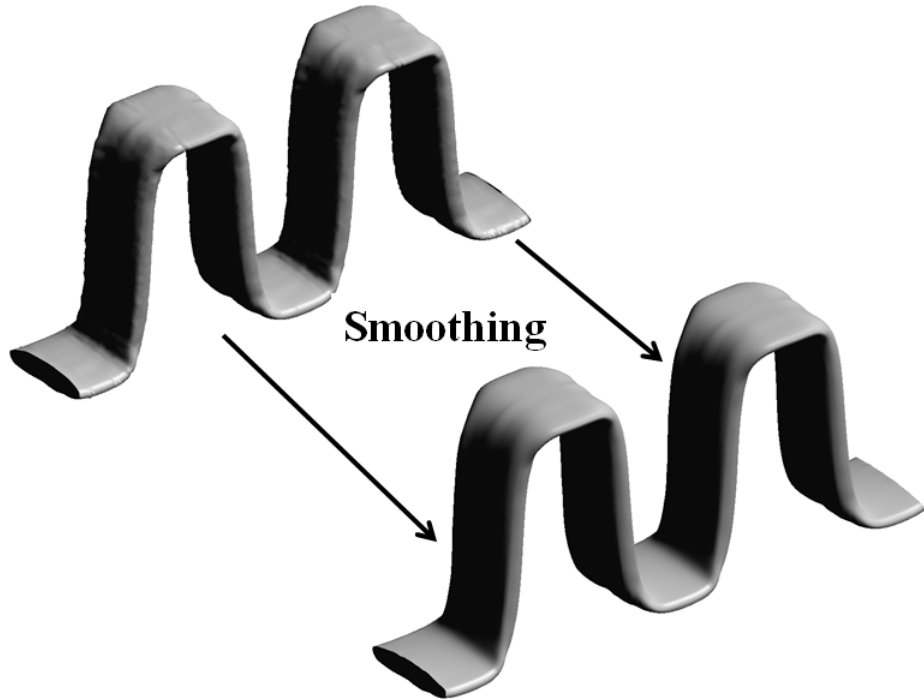


Figure 6.10: Regular Binder Tow Before and After Smoothing Application

After the regular tows were generated, the tows were smoothed in order to remove the wrinkles within the tows. Even though this smoothing made the mesh coarser and therefore less accurate, doing this was necessary in order to generate a 3D mesh in the Mesh Generator Module. Without smoothing, it would have been extremely difficult to generate elements in small wrinkled areas. This issue was due to the high quality hexahedral elements that were desired for the RX-FEM method utilized by BSAM. Smoothing eliminated the wrinkled areas, therefore making hexahedral meshing possible. Figure 6.10 shows a binder tow from the preform model before and after smoothing was applied.

After the preform model was smoothed, interpenetrations between meshes were removed. Since meshes were imported into BSAM on an individual basis, it was vital that elements in a tow did not

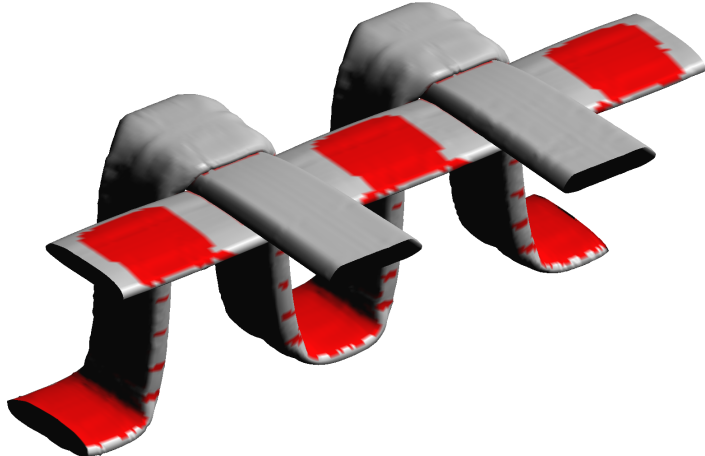


Figure 6.11: Regions of Interpenetration Between Tows

share any space with elements in other tows. Figure 6.11 depicts some of the areas of interpenetration between tows in the preform model. The areas highlighted in red are areas where interpenetration had been detected. These regions primarily appeared where adjacent tows were touching and areas where a higher degree of pressure had been applied to the tow. To remove these inter penetrations, the Tow Modification Module checked for areas where tow paths crossed each other. Next, the surface nodes in the areas of interpenetration were moved by small increments until tow paths no longer crossed. Like the smoothing algorithm, doing this decreased the accuracy of the model, but was ultimately necessary in order to obtain a usable result. Figure 6.12 depicts the regular tow surface meshes of the preform model after smoothing was applied and interpenetrations were eliminated.

After the generation of the regular tows and the desired degree of smoothing was applied, clipped tows were generated. Clipped tows are another type of surface mesh, but instead of defining the mesh by slices and stacks, the mesh is entirely composed of triangular polygons. Generating clipped tows allowed for the tows to be more easily modified in the Mesh Generator Model and also



Figure 6.12: Regular Tow Surface Mesh Model of Fabric Preform

allowed the tows to be cut at varying angles. Figure 6.13 depicts the clipped tow surfaces meshes of the fabric preform model.

6.5 Mesh Generator Module

After generation of the tow surface meshes, a three dimensional volumetric mesh of each of the tows had to be created. For this, the Mesh Generator Module, a module specifically designed to create tow meshes consisting of high quality hexahedral elements, was used. The Mesh Generator Module creates 8-noded hexahedral C3D8 elements, the only elements currently readable by BSAM, an example of which is shown in Figure 6.14.

For the fabric preform model, two mesh generation methodologies had to be utilized. For the warp and weft tows, the clipped tow surface meshes were imported into the module. A longitudinal mesh density, the number of cross-sections generated along the length of the tow, was set for each of the tows. For weft tows, the longitudinal mesh density was 25 slices and for warp tows it was



Figure 6.13: Clipped Tow Surface Mesh Model of Fabric Preform

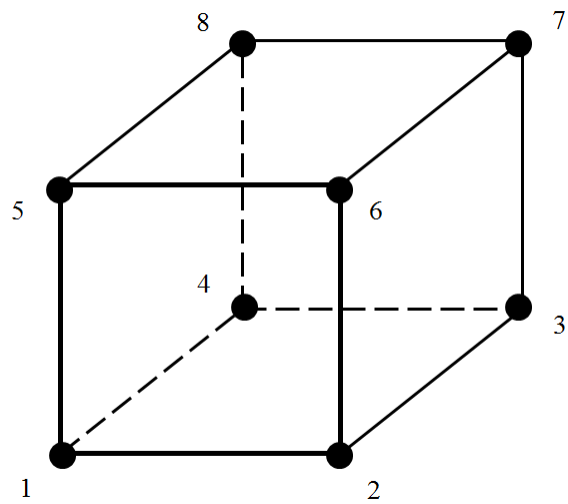


Figure 6.14: C3D8 Element Example

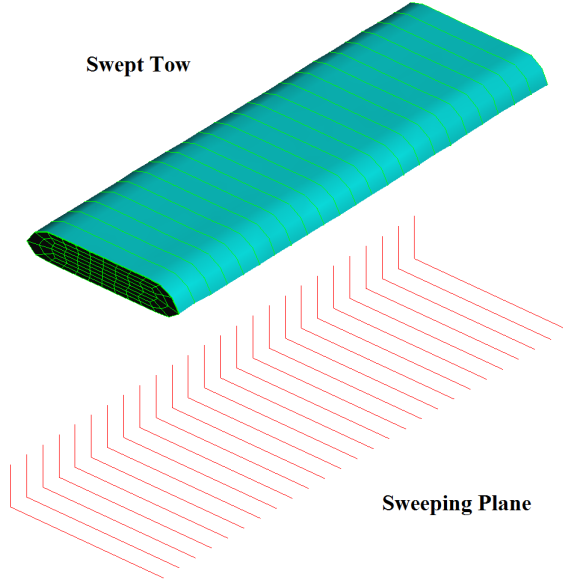


Figure 6.15: Swept Weft Tow and Corresponding Sweeping Plane

75 slices. These densities were chosen since the warp tows were approximately three times larger than the weft tows. After these parameters were set, the module then utilized a simple sweeping algorithm to generate a three dimensional mesh for each tow. A swept weft tow from the preform model and its corresponding sweeping plane can be seen in Figure 6.15.

After sweeping the clipped tows, the module was used to generate a hexahedral mesh for each of the tows. This process varied greatly from tow to tow, so only general steps of the process used will be discussed here. First, for each tow, the module assumed that the geometry of each cross-section was approximately equal and therefore generated the same 2D rectangular mesh on each cross-section face. The module then reported on the element quality of the mesh and determined whether or not elements in the mesh were of adequate quality for BSAM analysis. If an element was deemed to be, what the module defines as “bad”, then the tow had to be re-meshed until all bad elements were completely removed. To remove the bad elements from the mesh, the three element quality control sliders were used. These sliders incrementally moved elements within the mesh in

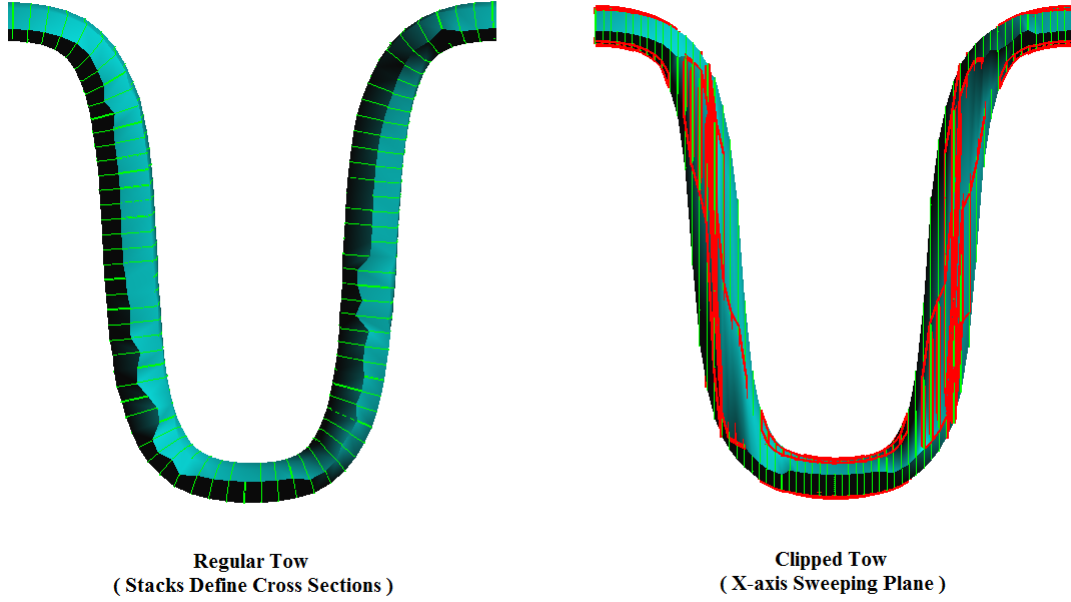


Figure 6.16: Regular vs. Clipped Binder Tow

order to fix elements with inadequate Jacobians and poor aspect ratios. This process was used for all warp and weft tows until all of the three dimensional meshes had been generated.

For the creation of the binder tows, a different three dimensional mesh generation technique was used. Instead of importing the clipped tow surface meshes of the binder tows, the regular tow meshes were imported. For regular tows, the module predefines the longitudinal mesh density based on the number of stacks in the regular tow. Since the cross sections in regular tows are defined by the number of stacks, the cross-sections follow the path of the tow instead of being defined by sweeping about an axis. Because of this, the use of regular tows was necessary to model the large undulation in the binder tows. Figure 6.16 shows why regular tows had to be used to model the binder tows in the fabric preform model. In this figure, the cross-sections of the regular tow vary based on the geometry of the tow. For the clipped tow however, the sweeping plane is held fixed on the x-axis

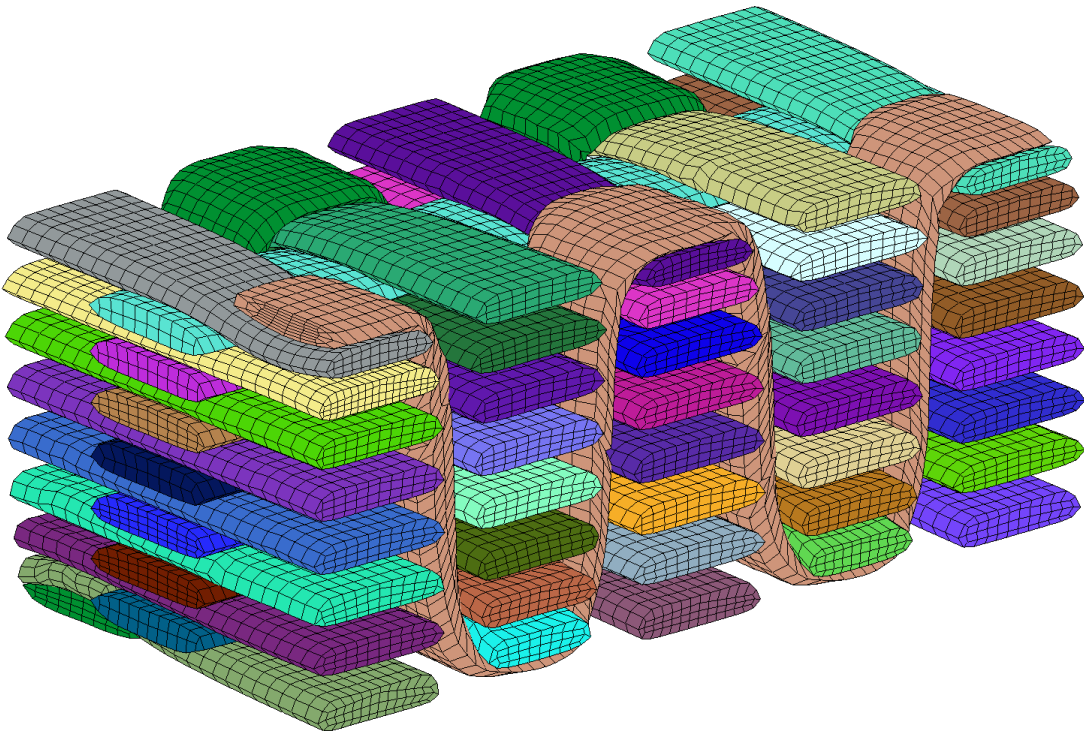


Figure 6.17: Three Dimensional Meshes Used in the Fabric Preform Model

which leads to the generation of irreparably bad elements (shown in red). As with the clipped tows, the element quality control sliders were used to eliminate all of the bad elements in the binder tows.

After mesh generation of the binder tows, the fabric preform model had been completed. The three dimensional mesh of the fabric model is shown in Figure 6.17.

6.6 BSAM Export Module

After completion of the three dimensional meshes, the fabric preform model was imported into the BSAM Export Module. The BSAM Export Module serves both to prepare the model for BSAM analysis and as a post-processor of results. All analyses of the dog-bone model were performed within the BSAM Export Module.

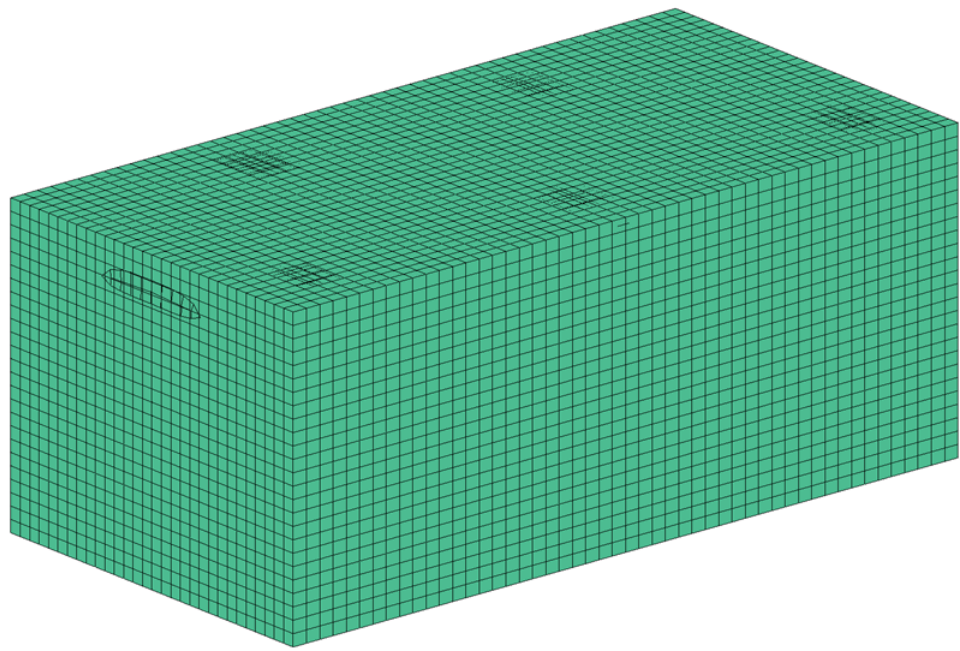


Figure 6.18: Composite Matrix Mesh of the Dog-bone Specimen

The three-dimensional meshes of the fabric preform model were first imported into the module. Next, a mesh for the matrix material of the composite had to be made. A rectangular prism mesh consisting of uniform homogeneous elements was generated with the following dimensions:

- x direction- 9.76 mm discretized into 50 elements
- y direction- 4.04 mm discretized into 25 elements
- z direction- 4.94 mm discretized into 30 elements

Before this mesh could be used, interpenetrations between the matrix and the tows had to be eliminated. For this purpose, the module has a volume subtraction feature that subtracts a defined volume from a mesh such that no two meshes share the same space. The mesh that is being subtracted from has the necessary elements deleted, moves nodes to the new boundary, and then reorients the nodes to obtain quality elements. The volume of all 48 tows was therefore subtracted from the matrix mesh as shown in Figure 6.18. Note that the subtracted volume was internal to the matrix mesh and

therefore cannot be seen by examining the outer surfaces of the mesh.

After all of the meshes were properly generated, connections between tows and the matrix were made. Since tows and the matrix were meshed independently, connections had to be made between them such that they behaved properly as a composite material. Connections were made based on a simple proximity tolerance of $1E^{-8}$; if elements from separate entities were within this tolerance, then the elements were deemed connected and would behave as a connected unit during analysis.

After the initial model set up had been completed, a simple tensile test was performed on the model of the gage section. This test was conducted primarily to showcase the viability of BSAM as an analysis tool and to obtain results for a model with no fiber volume fraction property variation implemented. A displacement boundary condition of 0.2 mm over twenty loading cycles was applied in the warp direction of the composite. Results from this test are shown in Section 8.2.

CHAPTER VII

FIBER VOLUME FRACTION METHODS

7.1 Local Fiber Volume Fraction- VTMS Approach

Initial Fiber Volume Fraction calculations were performed by utilizing an element by element approach within the BSAM Export Module of VTMS. Finite element meshes of fabric tows are imported into the module along with the corresponding fiber files used to generate the respective meshes. The fiber files are superimposed on top of the meshes and a local fiber volume fraction is then calculated. A fiber volume fraction is obtained for each individual element in the mesh based on the volume of fiber within the volume of each element. To obtain this element level fiber volume fraction, each individual element is discretized into a mesh of sufficiently small three dimensional elements. An algorithm checks these small elements for fiber areas greater or less than 50% of the element. If the micro-element has a FVF greater than 50%, then the entire micro-element receives a FVF of 100%. Conversely, if the FVF is under 50%, then the entire micro-element receives an FVF of 0%. These micro-element values are then averaged to determine the fiber volume fraction for the overall element. An example of this discretized element fiber volume fraction can be seen in Figure 7.1. For the element slice shown in Figure 7.1, there are a total of 32 micro-elements within the larger element. Twelve of those micro-elements receive a FVF value of 100% while the other twenty micro-elements receive an FVF of 0%. The total fiber volume fraction for this element slice is therefore 37.5%.

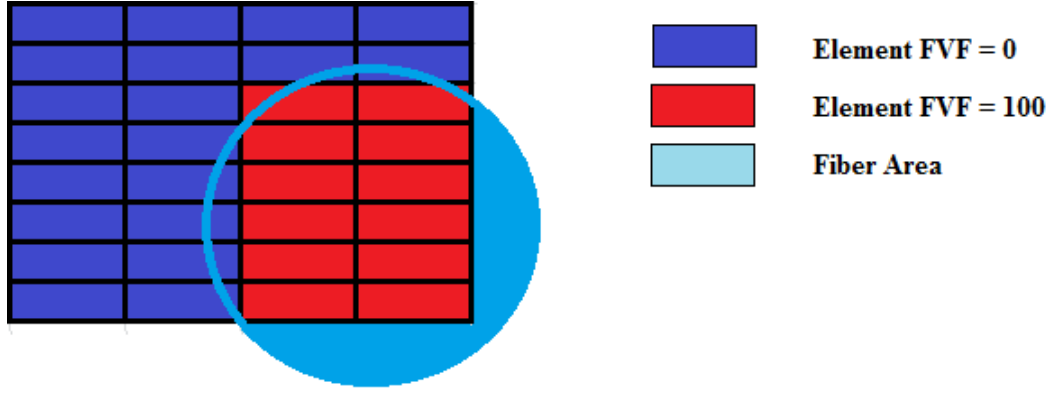


Figure 7.1: VTMS Fiber Volume Fraction Approximation Element Discretization

Although this methodology induces some error by its nature, this approach allows for inter-element fiber volume fraction variation to be obtained. This variability is valuable because it limits possible inaccuracies due to coarse meshes. For instance, a relatively large element from a coarse mesh is likely representative of a large portion of the physical specimen, which may have a large degree of variability within that region. This large element can still represent some of the variability by utilizing the micro-element discretization method. Once each element fiber volume fraction is obtained, FVF values are interpolated to each element node. This additional step is necessary since BSAM reads in data on a node by node basis rather than an element basis. Furthermore, assigning FVF values to the nodes allows for BSAM to read and understand the respective FVF values. Local element fiber volume fraction of binder tows obtained from VTMS can be seen in Figure 7.2.

A complication with this approach is that there are fibers that fall outside of the meshed area that are not accounted for. Although the finite element mesh is generated based on a surface area approximation of the tow, the mesh does not capture the full area of the actual tow. This primarily occurs due to the initial surface area approximation of the tow. Figure 7.3 depicts a binder tow (represented by the blue fibrils) and its corresponding surface area approximation (grey area). As

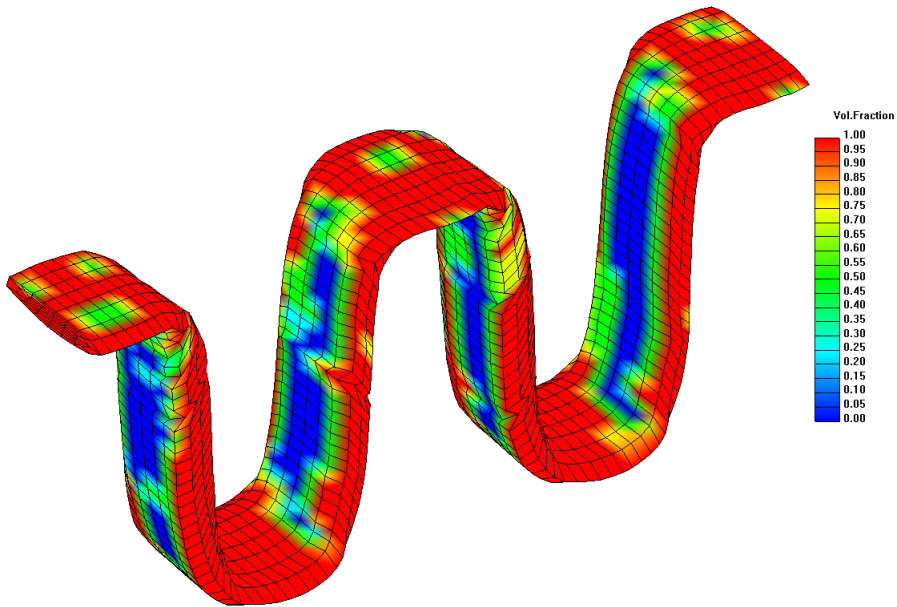


Figure 7.2: Local Element Fiber Volume Fraction of Binder Tows- VTMS Approach

can be seen in this figure, a significant amount of fiber is outside of tow surface area approximation. This is particularly true for binder tows and for areas in tows where a high level of pressure or compaction is observed. This issue is further exacerbated by the fact that the tow finite element mesh is generated from the surface tow geometry. In addition, the surface tow geometry is often smoothed to a great degree, increasing geometric inaccuracies in the model. Due to element quality and computational efficiency constraints, the tow finite element mesh often covers an even smaller volume than the volume covered by the surface area approximation. To clarify, the mesh generator in VTMS completely inscribes the tow finite element mesh within the tow surface area approximation. A mesh that is refined at cross-sectional faces will better represent the boundaries of the surface approximation. However, the finite element mesh will always be smaller than the surface area approximation to some degree and greatly refining the mesh at cross-sectional faces is often not computationally feasible. Figure 7.4 depicts the same binder tow as seen in Figure 7.3 and its corresponding finite element mesh approximation. It can clearly be seen that multiple fibers lie

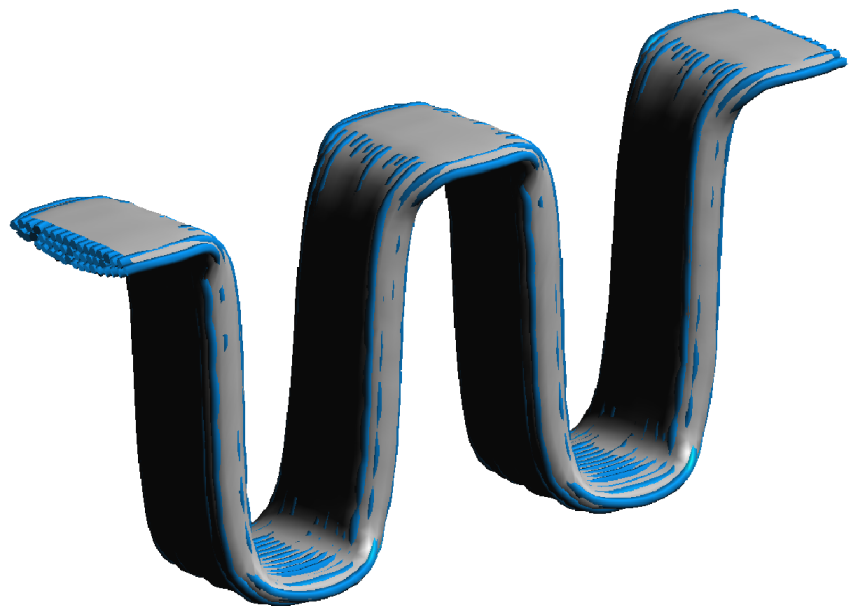


Figure 7.3: Error in Tow Surface Area VTMS Approximation

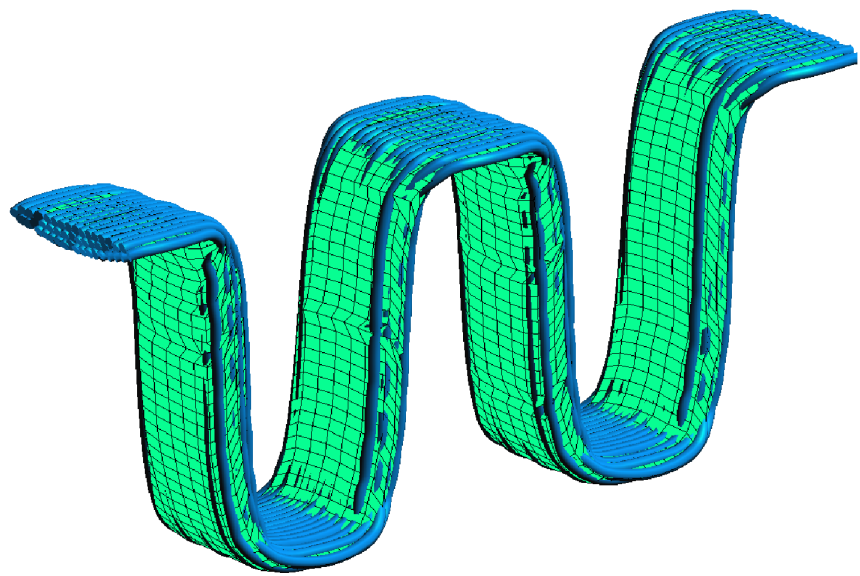


Figure 7.4: Binder Tow Finite Element Mesh and Corresponding Fiber

outside of the finite element mesh. Furthermore, there are clearly more fibers outside of the mesh than there were with the surface area approximation. In addition, there are areas and elements where no fiber is present, which will lead to a local fiber volume fraction of zero for those respective elements. In reality, there are rarely local areas of zero fiber volume fraction, highlighting another weakness of the approach.

To absolve some of these aforementioned issues, the BSAM Export Module has the ability to re-sample the fiber volume fraction approximation in two different ways. Firstly, the finite element approximation can simply assign new fiber volume fraction values to the nodes to reach a target average tow fiber volume fraction. With this approach, the node-to-node FVF ratios of the original approximation are kept and then an offset is applied to the nodes to reach the target fiber volume fraction. Another means of modifying the approximation is to re-sample the fiber volume fraction through window smoothing. In this method, a window size is defined, and then node by node the algorithm generates a virtual spherical window based on the defined diameter. The algorithm then averages all the fiber volume fraction values for a given window and assigns this new value to the node. With this methodology, the average fiber volume fraction for the tow remains the same, but the node-to-node FVF variability is damped/smoothed. This can be a valuable resource to eliminate areas where extreme fiber volume fraction approximations (low or high) are prevalent. Figure 7.5 shows how the tow shown in Figure 7.2 can be re-sampled to obtain a more realistic approximation for the fiber volume fraction variation within the tow. The original binder tow had a fiber volume fraction of approximately 0.90 and regions of extreme fiber volume fraction values. First, the extreme regions were smoothed by re-sampling with a window size of 0.2. The new approximation was then re-sampled to a target fiber volume fraction of 0.60, which is a much more realistic approximation.

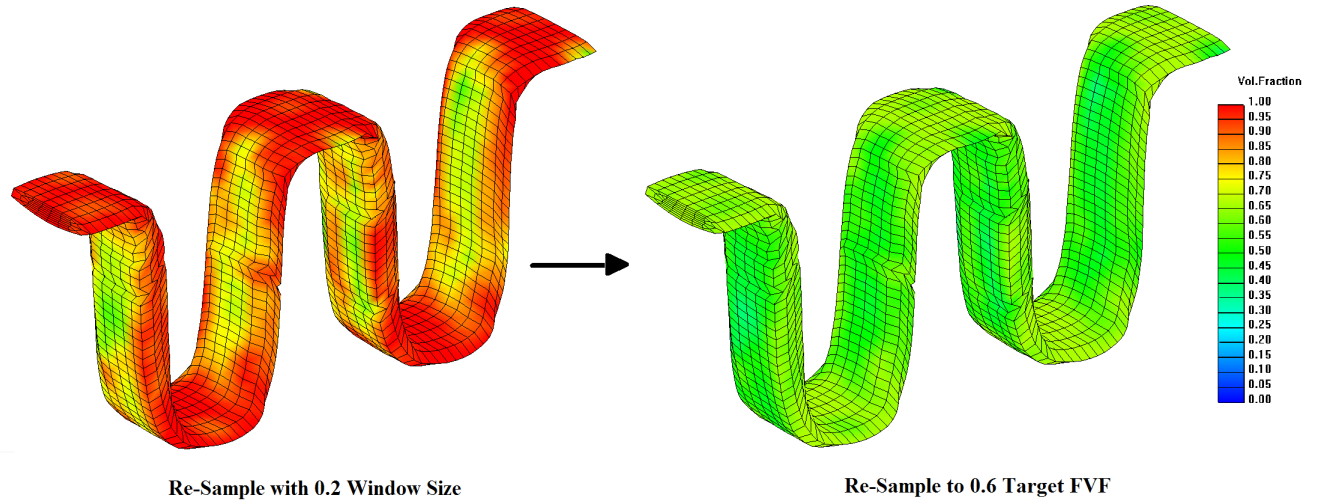


Figure 7.5: Re-Sampling of Binder Fiber Volume Fraction

Although the re-sampling methods described can be effective in eliminating some of the unrealistic results obtained from VTMS, these methods are somewhat unsatisfactory in the sense that user data manipulation is required. Ideally, VTMS would be able to produce accurate fiber volume fraction estimates with little to no manual data manipulation. Furthermore, the window re-sampling technique eliminates variability from the model without considering the original fiber model. The effect of modeling individual fibers is essentially eliminated if the fiber volume fraction estimation is going to be smoothed with window re-sampling.

7.2 Manchester Study

In a study conducted in conjunction with Professor Prasad Potluri of the University of Manchester, U.K., a 2D plain weave preform was compacted and imaged in an X-ray CT. An image of the compacted preform under 10 KPa of compression (Courtesy of University of Manchester) is shown in Figure 7.6. Parameters of this preform were provided to AFRL/RXCC for digital modeling purposes; parameters included:

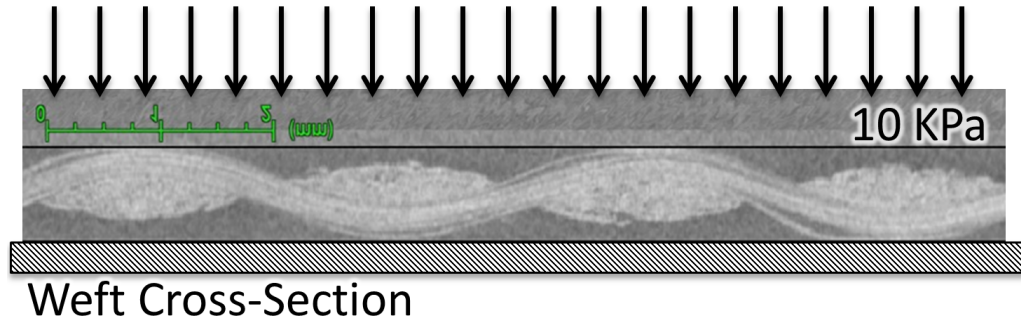


Figure 7.6: Compacted Carbon Fiber Plain Weave Pre-Form

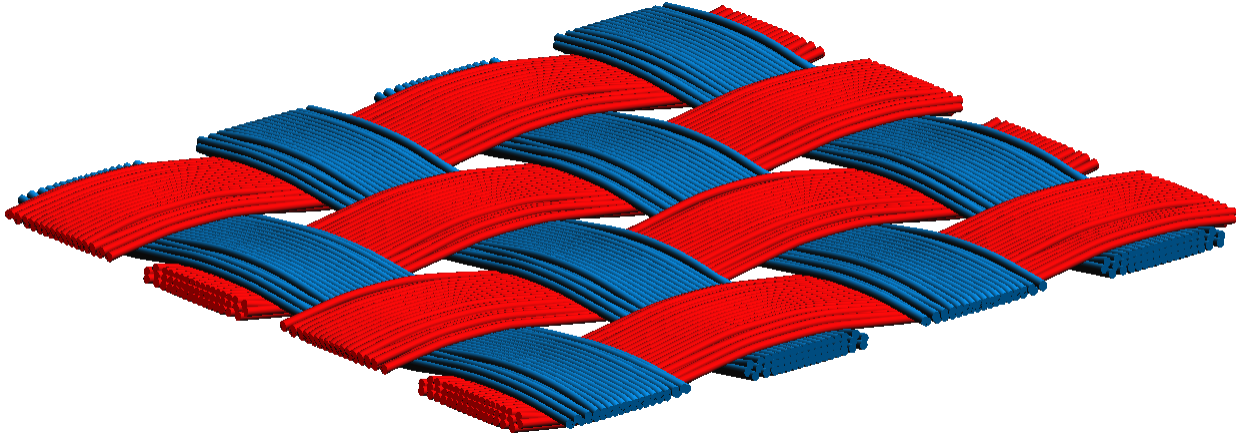


Figure 7.7: Original VTMS Model of Plain Weave Compacted Preform

- Fiber diameter and fiber count in both tows
- Crimp (undulation of tows)
- Tow spacing
- Tow cross-sectional height and width

Originally, an exact match of parameters was attempted which is shown in Figure 7.7. In general, it was found that an exact matching of all parameters led to a model that was not indicative of the preform. First of all, as shown in Figure 7.7, the tow spacing in the model led to large pockets of open spacing that are not typically seen in plain weave fabrics. Furthermore, crimp undulation

was significantly smaller than the defined crimp parameters. VTMS does not have a user-defined parameter for crimp; instead, the model undulation is defined by the end solution of the relaxation algorithm. Consequently, undulation in the model is primarily due to packing of the fibers and forces imposed on the model. Finally, tow cross-sections did not properly match the geometries shown in the original micro-CT image. In general, it was found that the cross-sections of the tows too closely resembled their original hexagonally packed geometry.

To resolve this issue, the diameter of the digital fibers was incrementally increased. The issue with the original VTMS model was that the model started with an idealized distribution of digital fibers. This led to closely packed fibers that occupied limited volume while increasing fiber volume fraction to an unrealistically high value. By simply increasing the diameter of the digital fibers, the tows occupied more space while decreasing fiber volume fraction. To match experimental values, it was found that the scaling factor should be approximately 1.4 times larger than the original dimension. The final digital model generated by VTMS based on modified fiber diameter (model made with the assistance of Dr. David Mollenhauer) as well as a comparison of the VTMS model to the original preform are shown in Figures 7.8 and 7.9, respectively. As shown in these figures, the digital fibers are generally indicative of the tow geometry and morphology shown in the micro-CT images. Furthermore, crimp undulation is relatively equivalent to what is shown in the micro-CT. In the original model, the average tow fiber volume fraction was approximately 90%; however, with the modified fiber diameter, the new fiber volume fraction was 64%.

In summary, to best attain a model that is generally indicative of experimental results, it is likely that the input parameters need to be modified. In practice, it has been found that the digital fiber diameters should be 1.4 times larger than their experimental physical dimensions.

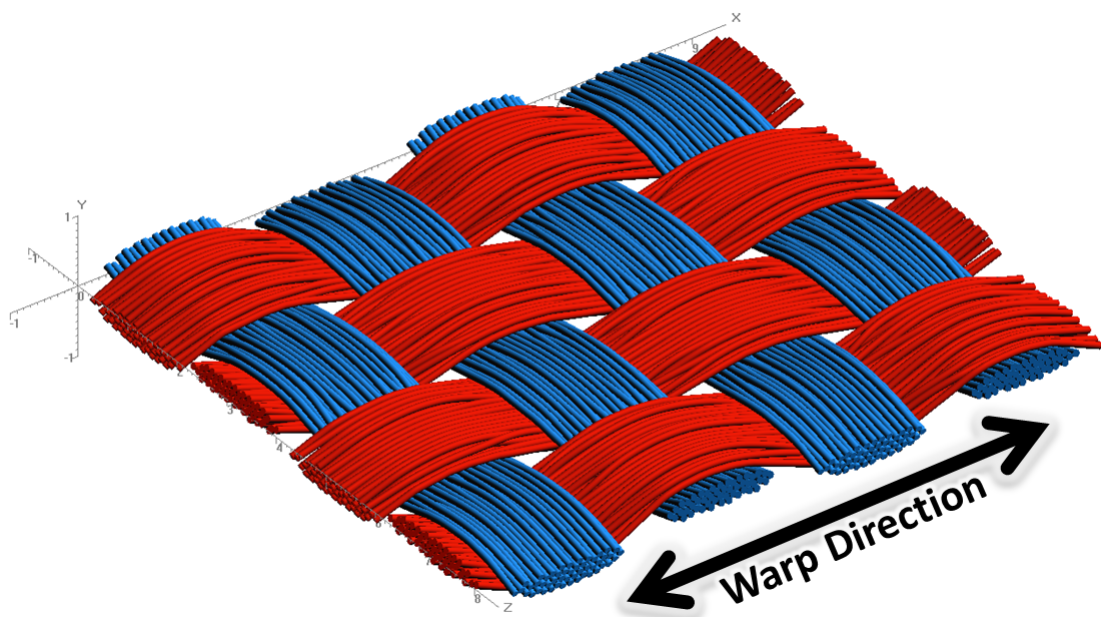


Figure 7.8: VTMS Model of Manchester Plain Weave Compacted Preform

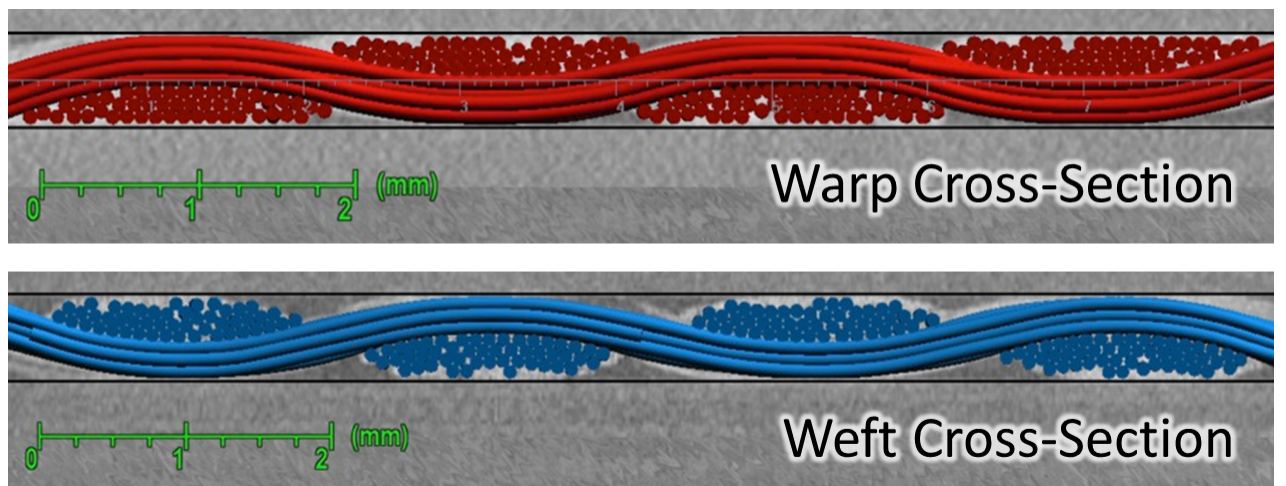


Figure 7.9: VTMS Model Compared to Micro-CT Results

7.3 Direct Image to Model Relation Method

One of the primary goals of the study was to directly relate experimental fiber volume fraction variation data to the computational models generated by VTMS. This goal had two different objectives, the first of which was to directly implement the FVF variation data within the model itself. The second goal was to improve the FVF prediction capabilities of VTMS such that the prediction more closely resembles experimental findings without actually utilizing any experimental FVF data to generate the model. This section will discuss the methodology used to directly implement fiber volume fraction data obtained from serial sectioning. Section 7.4 will discuss a possible means of modifying the VTMS prediction to more accurately reflect results obtained from experimental data without necessitating the use of experimentation.

The overall goal of directly relating experimental fiber volume fraction data to the VTMS computational model is to create a model that is the closest possible representation of the experimental data. Geometrically speaking, VTMS can easily accomplish this with its built-in tools. From a fiber volume fraction variation standpoint, however, a methodology must be developed to implement the experimental data within the model. The first obstacle in accomplishing this is an issue caused by the angle of the cut and the subsequent angled serially sectioned imaging. The serial sectioning performed on the final specimen was at a 45 degree angle. Note that at this angle, fiber volume fraction data cannot be obtained for the binder tows.

Since each image slice was taken at a 45 degree angle, this meant that the imaging did not directly correspond to the typical tow finite element mesh. In a tow finite element mesh generated by VTMS, the cross-sectional face is extruded as stacks along the length of the tow; each stack is aligned with the zero degree cross-sectional face. To solve this issue, a coordinate system was defined for each image slice. The center-point of each sampling window in the FVF variation algorithm was then determined in this coordinate system. Next, these coordinates were transformed

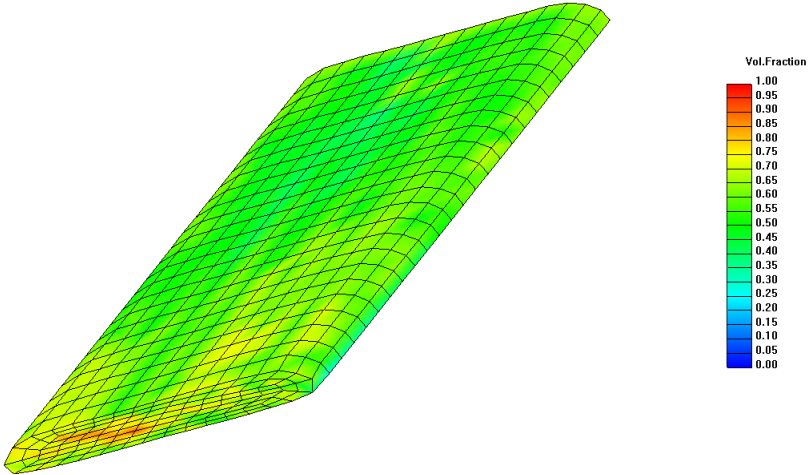


Figure 7.10: Direct Image to Model Fiber Volume Fraction Relation

to the model coordinate system and then data points from the image slices were defined to the closest node coordinates in the model space. An example of the implementation of this methodology is shown in Figure 7.10. As seen in this figure, fiber volume fraction variation is consistently in the range of 50 - 70% which was to be expected. In addition, areas of extreme fiber volume fraction values are localized in only a few areas; this is consistent with what has been seen in the image slices of the textile.

The primary issue with this approach was that the coordinates of the node data were frequently not close to the coordinates of the nodes in the model. Ostensibly, the data sampling of the specimen was not indicative of the relative placement of the nodes in the model. For clarity, consider Figure 7.11. In this figure, the blue lines represent image slices, with the red dots showing the consistent sampling coordinates for fiber volume fraction. The black lines represent the cross-sectional slices in the computational model; all nodes in the model appear on these lines. Nodes in the model will be given a fiber volume fraction value from the closest image sampling coordinate (red dots). Obviously, there are many instances in which points on the black lines have no red dot near them.

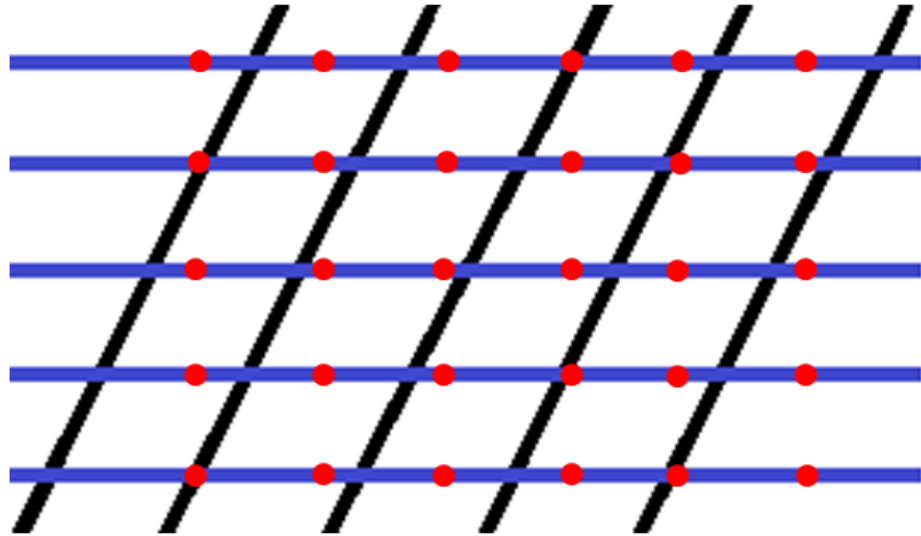


Figure 7.11: Image Sampling to Model Coordinate System Transformation Error

Therefore certain nodes in the model will be given a fiber volume fraction value that doesn't accurately represent physical reality.

7.4 Hierarchical Weibull Fit Redistribution Method

One of the primary obstacles from a computational modeling standpoint is how to effectively implement experimental fiber volume fraction values within VTMS. Ideally VTMS would have the ability to accurately predict an element by element FVF without any sort of experimental input data. But given the computational limitations of VTMS, this goal is somewhat unrealistic. One possible solution is to have an hybrid approach which utilizes both VTMS predictions and experimental data. Obviously the drawback of this is that one does not want to have to perform experimental tests every time they make a model; doing so would defeat the purpose of modeling. Instead, it is proposed that VTMS utilize a “look-up table” of experimental values to modify VTMS prediction data. After sufficient data has been obtained, VTMS could have a table of parameterized distributions for a target mean. VTMS would predict the mean fiber volume fraction, look up the parameters for the

fabric with that mean fiber volume fraction, and then assign the FVF values from that distribution to the model.

Utilizing a “look-up table” is a viable option since it utilizes experimental data to predict the fiber volume fraction. However, the next issue that arises is— how does one assign the values from the distribution to the computational model? It could be possible to directly correlate experimental FVF values from the image stack with their relative positions in the computational model. However, this once again would defeat the purpose of the model since one would have to collect experimental data for every specimen. A possible solution would be to utilize a hierarchical node redistribution method. With the proposed method, fiber volume fraction values calculated by VTMS will be used as a predictor of locations for values from the look-up table distribution. Nodes would simply be ordered from in lowest FVF to highest and then the look-up table distribution would be scaled to the number of nodes in the model. The node with the lowest FVF from the VTMS prediction would receive the lowest FVF value from the scaled distribution. Likewise, the node with the highest FVF from the VTMS would receive the highest FVF value from the scaled distribution. Once all nodes have been assigned a new FVF value, the nodes would return to their original respective ordering. Figure 7.12 shows how this methodology would work for a tow that exhibits an experimental Weibull distribution.

Figure 7.12a shows experimental values on a Weibull probability plot. Given that these experimental values are fairly closely scattered about a line, we can conclude that this is approximately a Weibull distribution. Weibull fit parameters are then obtained from the experimental data. Part c shows the original VTMS fiber volume fraction prediction. The number of nodes in this model are then counted and the parameters obtained from part a are scaled to the number of nodes in the model. The new Weibull fit distribution is shown in a probability plot in part b. Part d shows the final output of the methodology; the new model has the fiber volume fraction values from part b

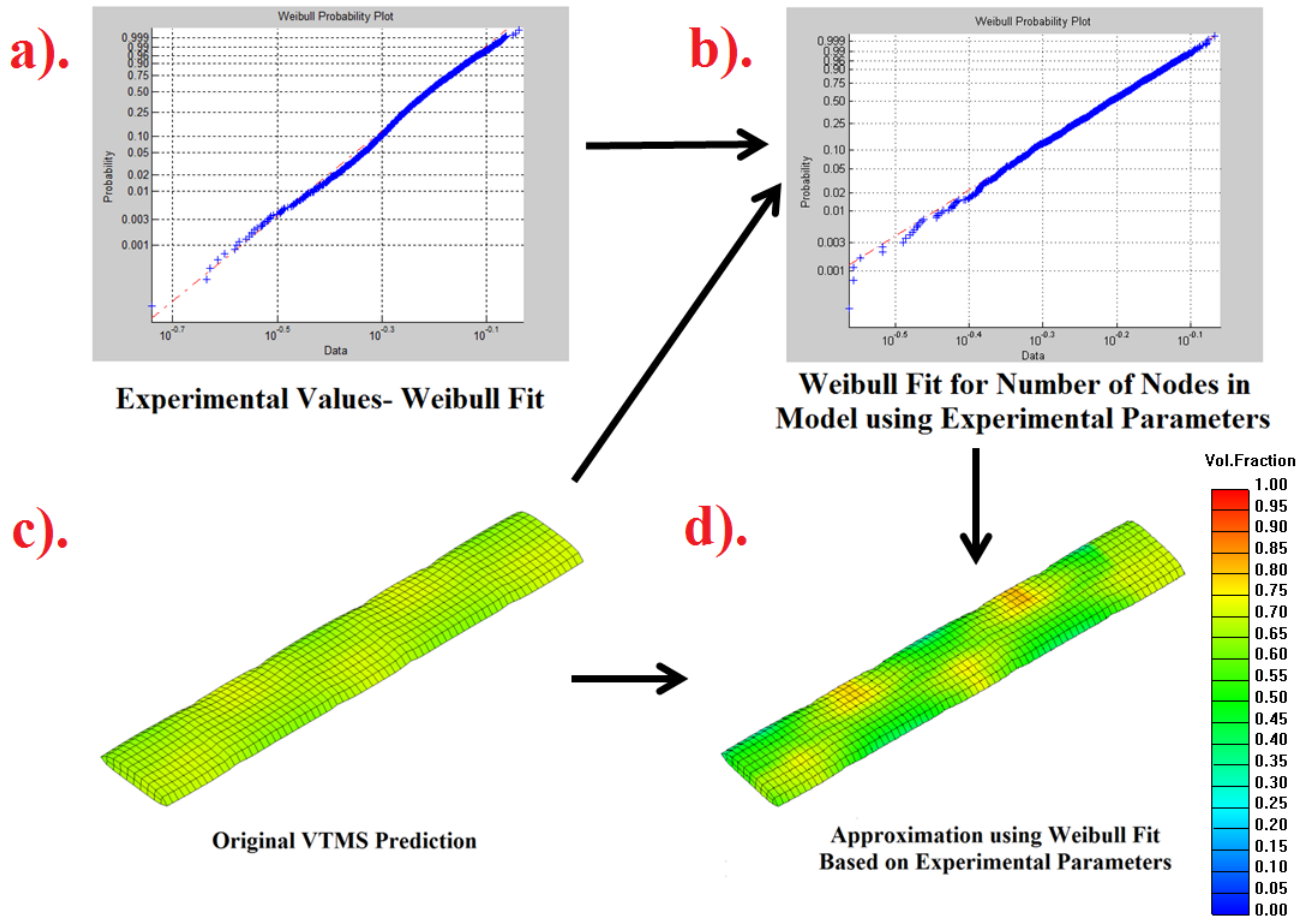


Figure 7.12: VTMS FVF Approximation Based on Experimental Weibull Parameters

with the ordering scheme of part c. As shown in Figure 7.12d, the model has a reasonable average fiber volume fraction as well as fairly limited areas of extreme values. Furthermore, the sections of higher fiber volume fraction directly relate to the original VTMS prediction, but are now more pronounced. In addition, it makes sense that these areas have a higher FVF since these are areas of cross over of neighboring tows.

CHAPTER VIII

RESULTS AND DISCUSSION

8.1 Digital Volume Correlation Results

The results from the digital volume correlation test conducted in Section 3.3 are shown in Figures 8.1, 8.2, 8.3, 8.4, and 8.5. Figure 8.1 depicts a slice from the digital volume correlation. This particular image shows the w direction displacement superimposed upon the corresponding image slice. As can be seen from this image, the warp tows clearly have a larger displacement in this direction than the weft fibers. This was to be expected since the z direction is the direction of the load; therefore the warp tows should bear the majority of load and consequently displace more than the other tows. It is important to note that the correlated region is adjacent to a binder tow. Upon close inspection of Figure 8.1, the correlated region is aligned at the edge of the warp tow cross-section; in other words, at the boundary of the warp tows and the binder tow. Although the binder tow is not within the correlated region, it may still have an effect on the DVC results.

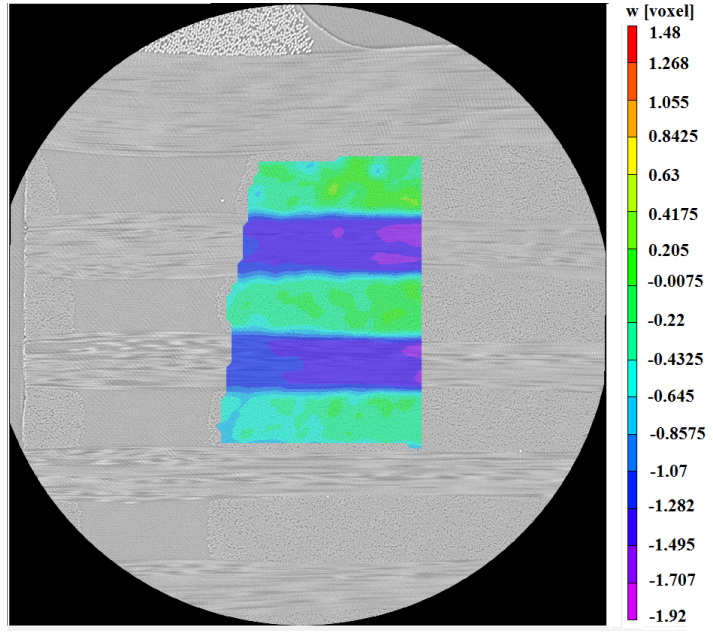


Figure 8.1: DVC- w Displacement Superimposed on Corresponding Image Slice

Figures 8.2, 8.3, 8.4 show three dimensional representations of the DVC results for the u , v , and w displacements, respectively. These figures show the stitched results of the DVC slices and are represented by a three dimensional volume.

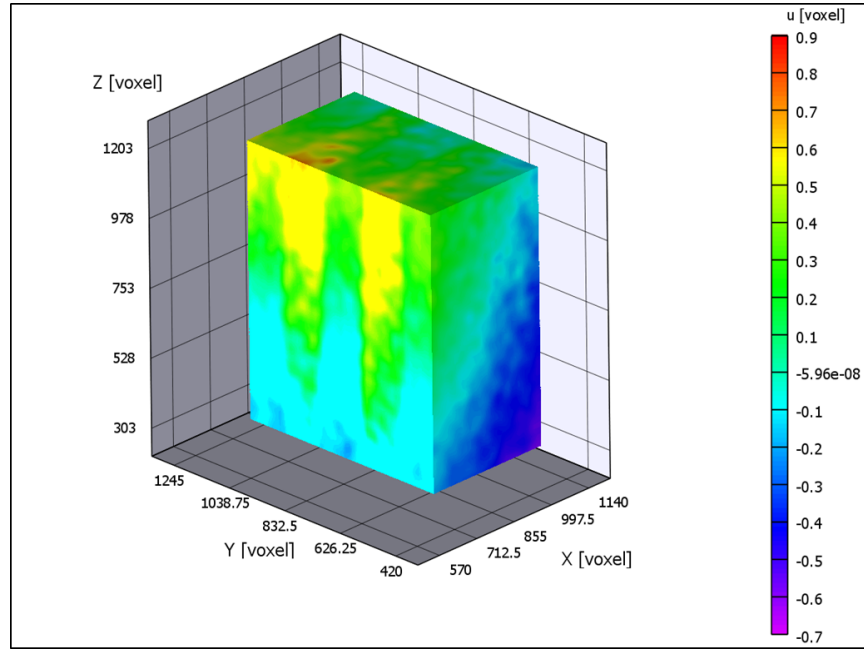


Figure 8.2: DVC- u Displacement

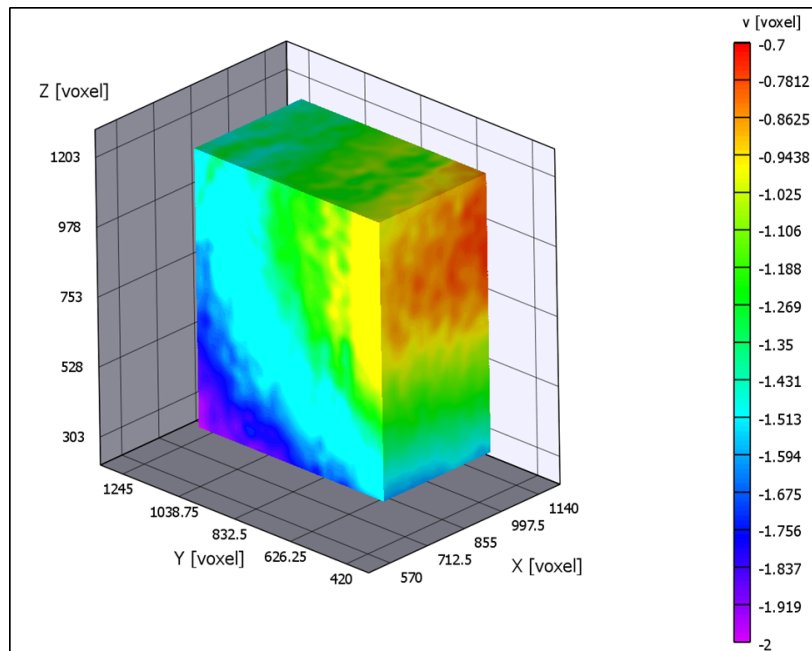


Figure 8.3: DVC- v Displacement

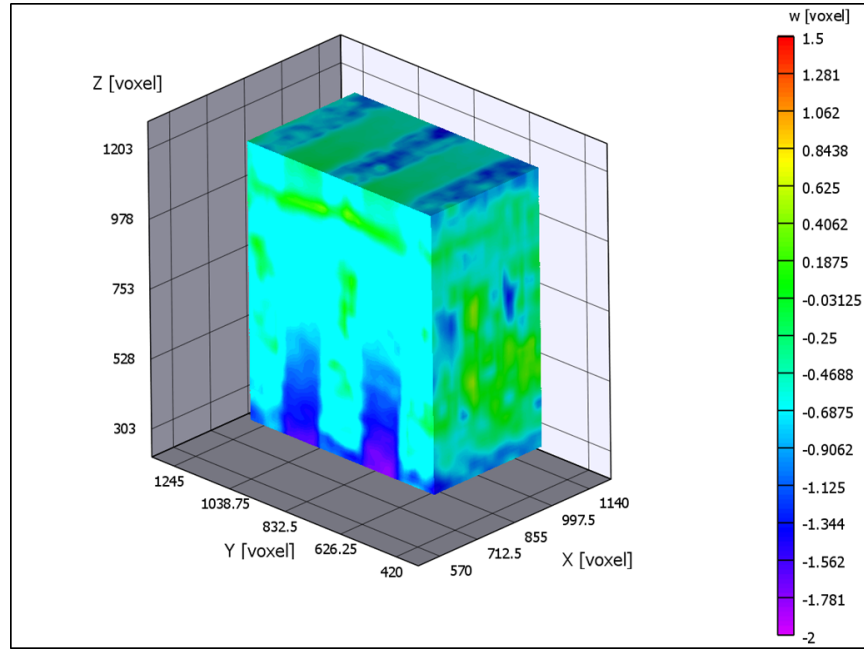


Figure 8.4: DVC- w Displacement

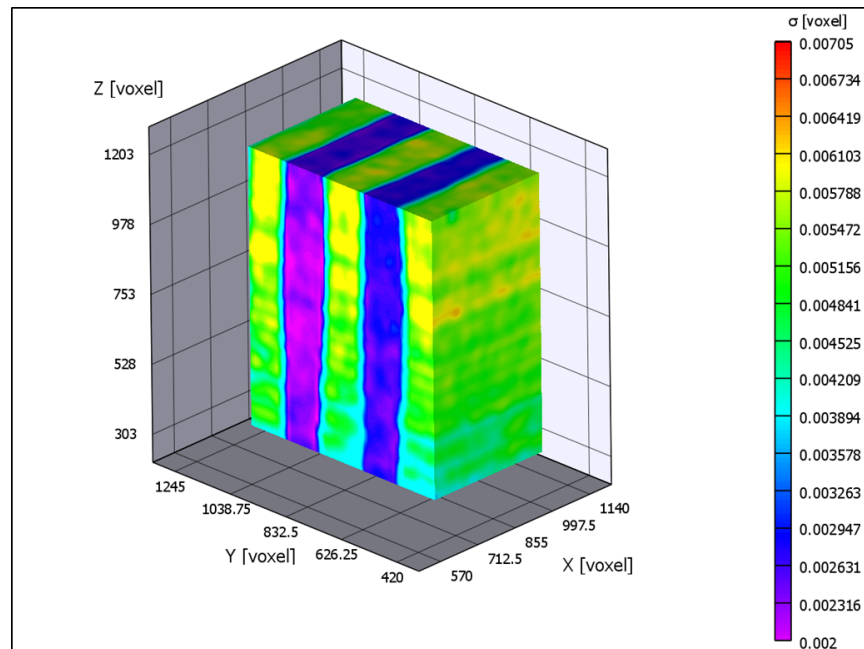


Figure 8.5: DVC- Stress

Once again, as shown in Figure 8.5, the warp tows clearly exhibit the highest amount of stress. This was to be expected and validates that the correlation was effective in this instance. However, when examining Figure 8.2 there is an unusually high degree of u displacement in both warp and weft tows near the binder region. Considering the specimen was loaded in the z direction, this could be due to Poisson's contractions. However, this seems unlikely since the lower end exhibits a negative u displacement. It is possible that the binder tows are pulling these tows in some fashion or that the correlation is simply incorrect. This issue appears again in Figure 8.4; the weft tows near the binder region have an unusually high degree of w displacement near the binder region. This would support the theory that the binder tows are pulling on the weft tows, which would cause a higher displacement in the z direction.

Ultimately, results from the digital volume correlation did not provide enough information to determine the effects of fiber volume fraction on the properties of the composite. Firstly, the micro-CT images were simply not taken at a high enough resolution to determine fiber volume fraction variation. Secondly, the accuracy of the DVC results was questionable considering the issues regarding the tows near the binder region. Stress variations were also largely tow dominated and there was not enough inter-tow stress variation to determine if fiber volume fraction variation within the tows had an effect on the stress.

8.2 BSAM Tensile Test Results

The results of the tensile test outlined in Section 6.6 are shown in Figures 8.6, 8.7, and 8.8. As shown in Figure 8.6, displacement appears as consistent bands throughout the composite. The largest displacement is observed at the face where the tensile load was applied, and the smallest is observed at the face that was held fixed. This showcases proper connection between tows and the matrix and performs comparably to a physical composite. Figure 8.7 shows that the warp direction strain is the lowest at regions where the binder tows cross-over the weft stacks. This was due to a

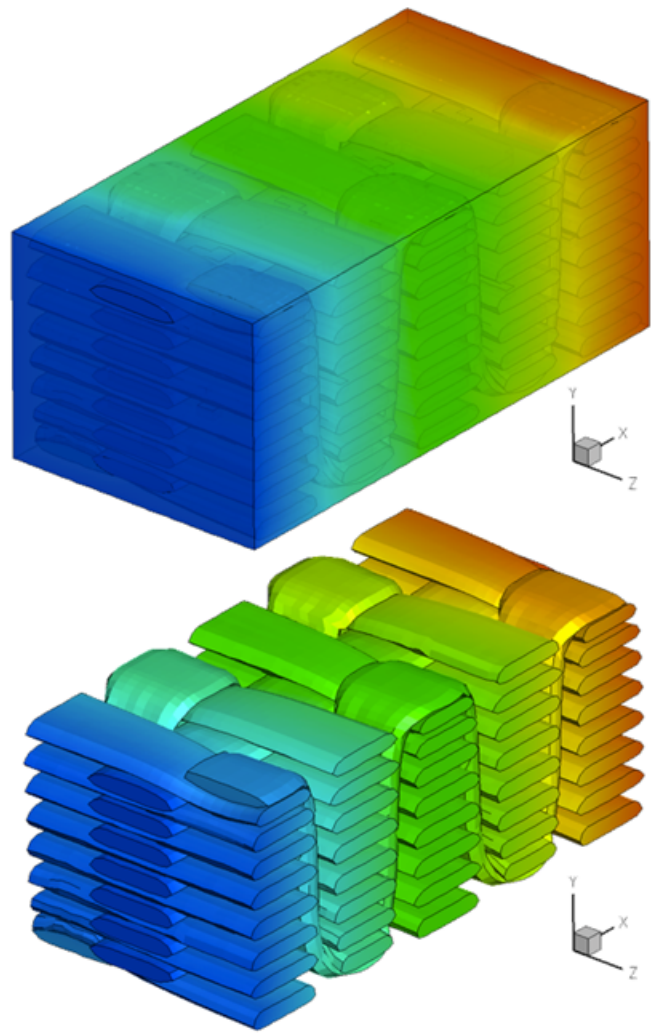


Figure 8.6: BSAM Tensile Test- Warp Direction Displacement

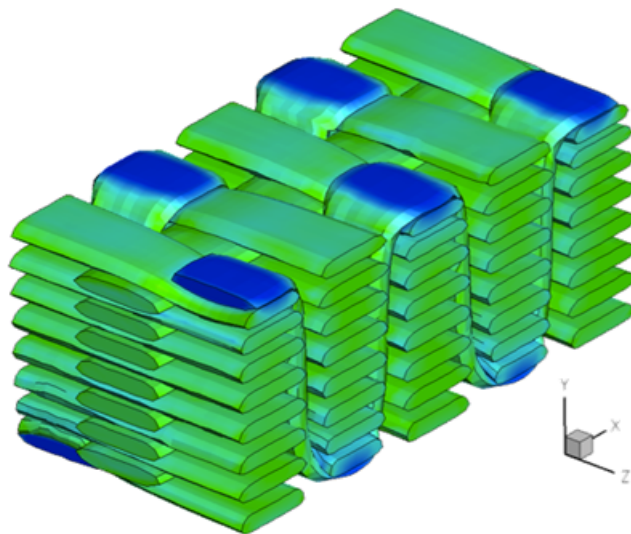


Figure 8.7: BSAM Tensile Test- Warp Direction Strain

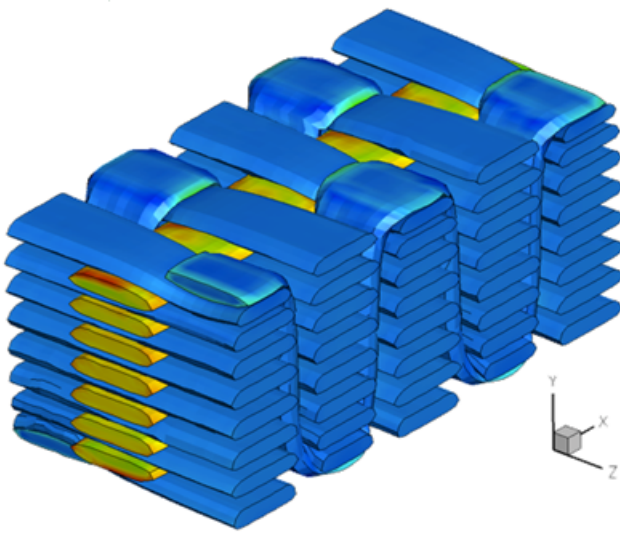


Figure 8.8: BSAM Tensile Test- Warp Direction Stress

bending effect; the cross-over regions exhibit compression as would be typical of a beam bending problem. Also, the regions of the binder tows oriented in the out of plane direction exhibit a much larger strain. It is likely that the binders are deforming in the warp direction for these regions, but remaining seemingly constant at the cross-over regions. This makes sense since the binder tows should deform most in regions where the fibers are not oriented in the direction of the load. Figure 8.8 shows that the greatest stress in the warp direction is observed in the warp tows. This was to be expected since the warp tows are oriented in the direction of the load and should therefore bear the majority of the load. Stress should possibly be higher in the cross-over regions in the binder tows, but this is not enough to invalidate the results.

Overall, the results verified the use of BSAM for analysis of 3D PMC textiles. Not only did the results match the typical behavior of this type of composite, but they also were mostly consistent with the DVC results observed in Section 3.3. Most discrepancies between BSAM and DVC results were likely due to errors in the DVC and not the computational model.

8.3 Fiber Volume Fraction Distribution Tests

Fiber volume fraction distribution tests were conducted to determine if the fiber volume fraction variation for different tows exhibited a consistent distribution. Ideally, if a consistent distribution was found, then this distribution could be implemented in future computational models in VTMS. Distribution tests were conducted on fiber volume fraction data obtained from 24 serially sectioned image slices taken at an approximate resolution of 1.40 microns/pixel. These images were obtained during the preliminary serial sectioning discussed in Section 4.2. A depiction of one of these image slices is shown in Figure 8.9. Please note that these images were taken at a considerably lower resolution than was desired for this study. Unfortunately, distribution tests had to be performed on these images given time constraints.

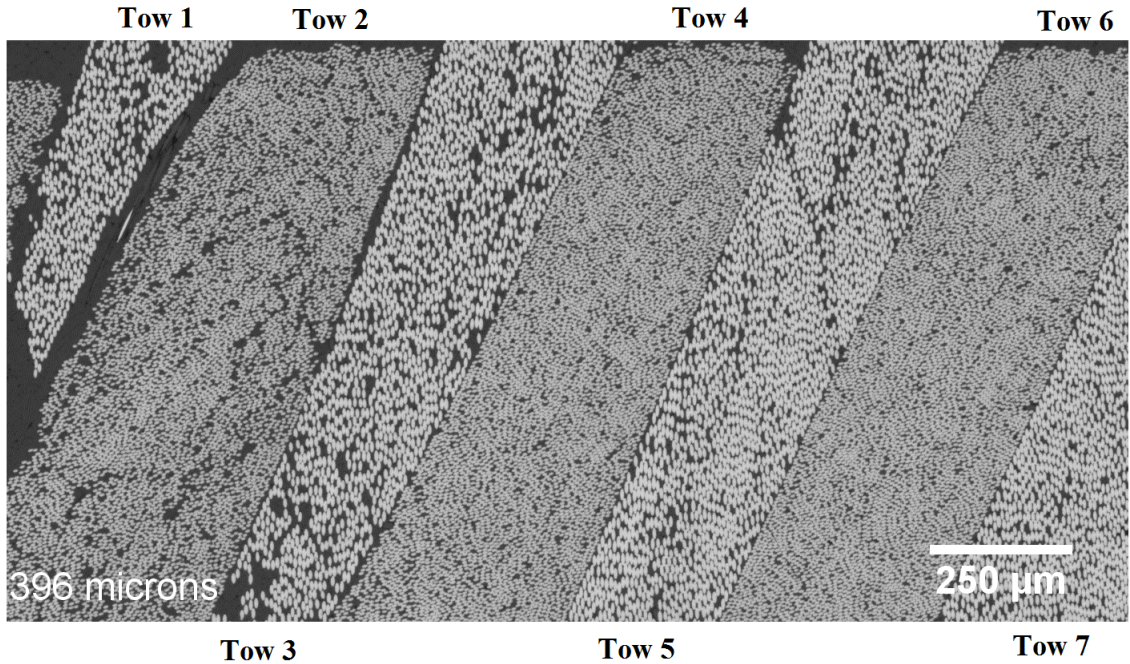


Figure 8.9: Image Slice Utilized for Distribution Tests

First, fiber volume fraction variation was obtained for each individual tow in the serially sectioned images. After data acquisition, the second tow was chosen to perform preliminary distribution tests upon. This tow was chosen due to the fact that it consistently appeared in all 24 image slices. The cropped second tow and its corresponding fiber volume fraction variation histogram are depicted in Figure 8.10.

Preliminary testing was performed on the second tow by generating probability plots for common distributions. A probability plot consists of a straight line based on calculated parameters of the distribution, and every data point in the sample set. If the data points appear approximately linear and are scattered about the line, then the data can be adequately represented by that distribution function. These plots were generated for the six available distributions in MATLAB and are shown in Figure 8.11. As seen in this figure, the Weibull probability plot clearly shows an approximately linear data set scattered about the line. The Rayleigh, exponential, extreme value, and logonormal

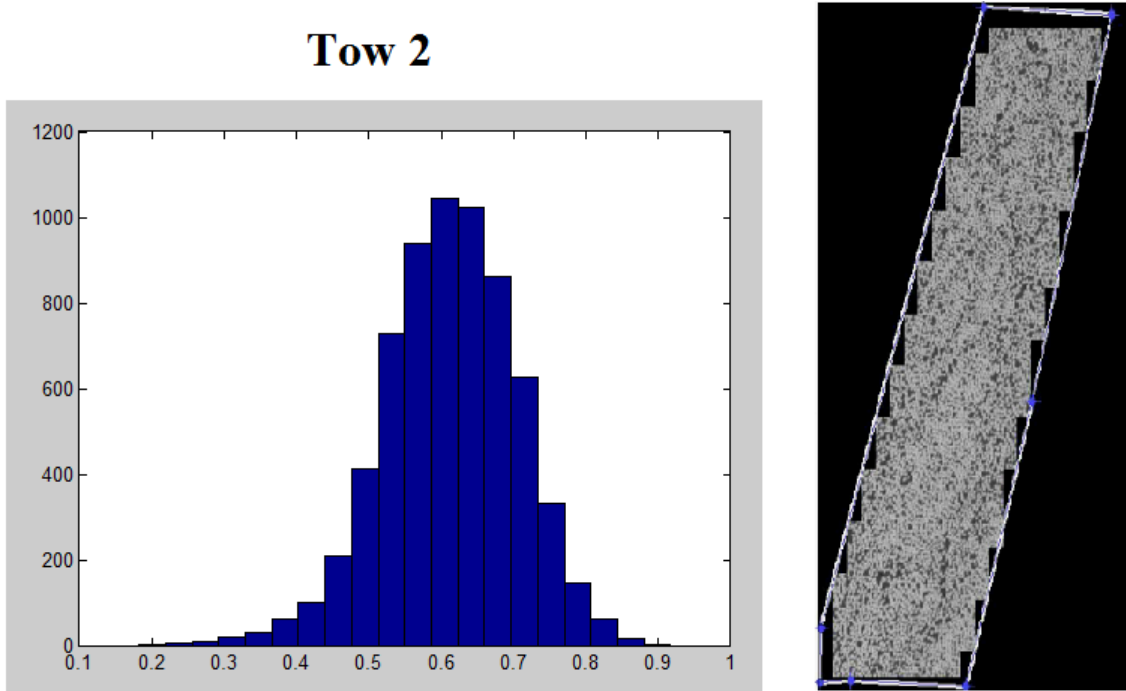


Figure 8.10: Tow 2- Cropped Tow and Fiber Volume Fraction Variation Histogram

distributions do not appear to correlate with the data whatsoever. Because of this, it was determined that these distributions should not be used to describe the fiber volume fraction variation in these tows. An argument could be made that the data may exhibit the behavior of a normal distribution, but the Weibull distribution is clearly a better fit.

After the preliminary testing was performed on the second tow, Weibull probability plots were generated for the other tows in the image slices. These Weibull probability plots for other tows in the image slices are shown in Figure 8.12. As shown in this figure, Tows 4, 5, 6, and 7 all exhibit the behavior of a Weibull distribution. Tows 1 and 3 however, appear to have a significant portion of the data that does not behave in a linear fashion about the line. Judging from the plots, it appears that there is a higher probability for a low fiber volume fraction than was expected for these two tows. This could possibly be due to the fact that both of these tows consist of AS4C 3k fibers; the larger

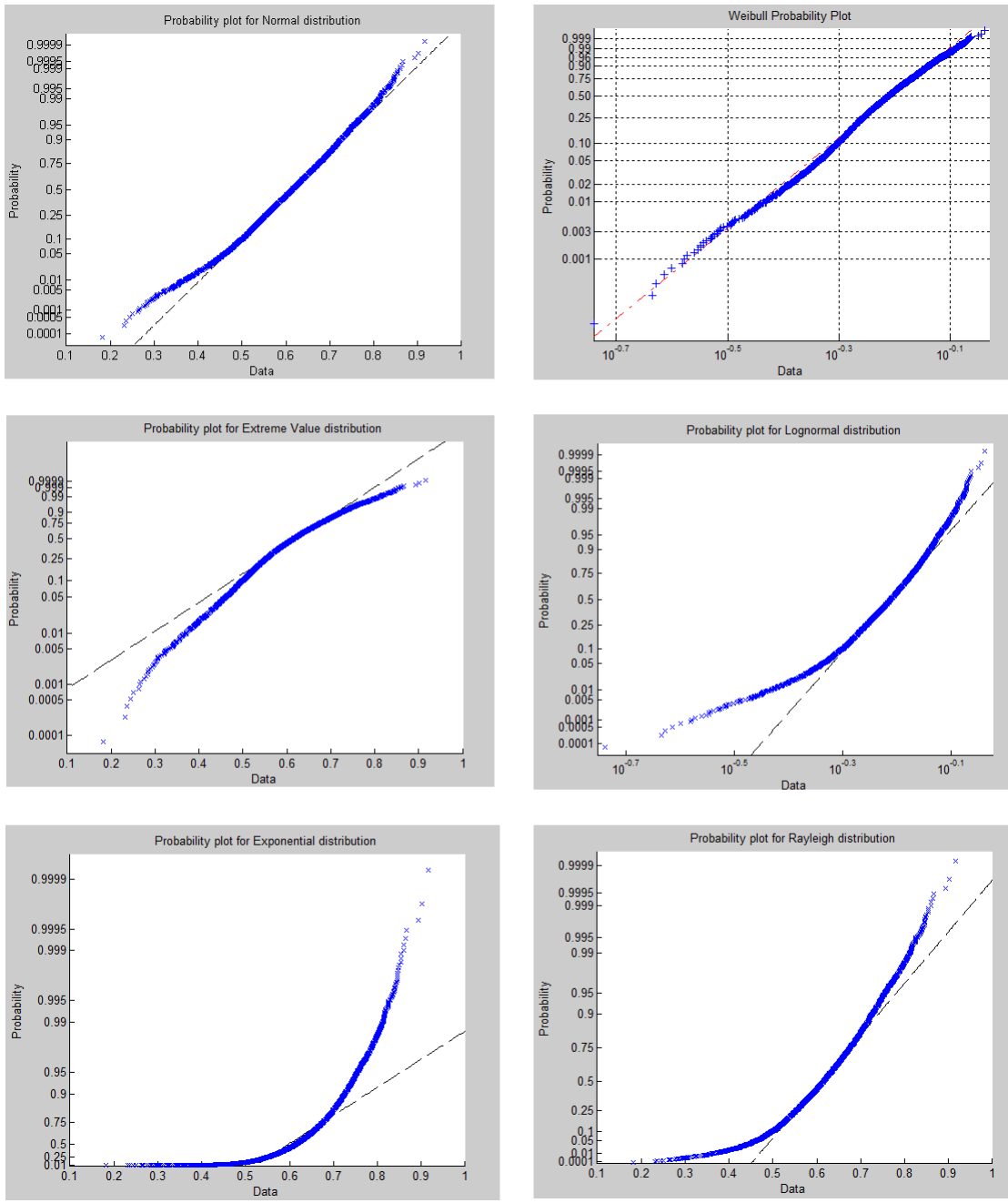


Figure 8.11: Tow 2- Probability Plots for Common Distributions

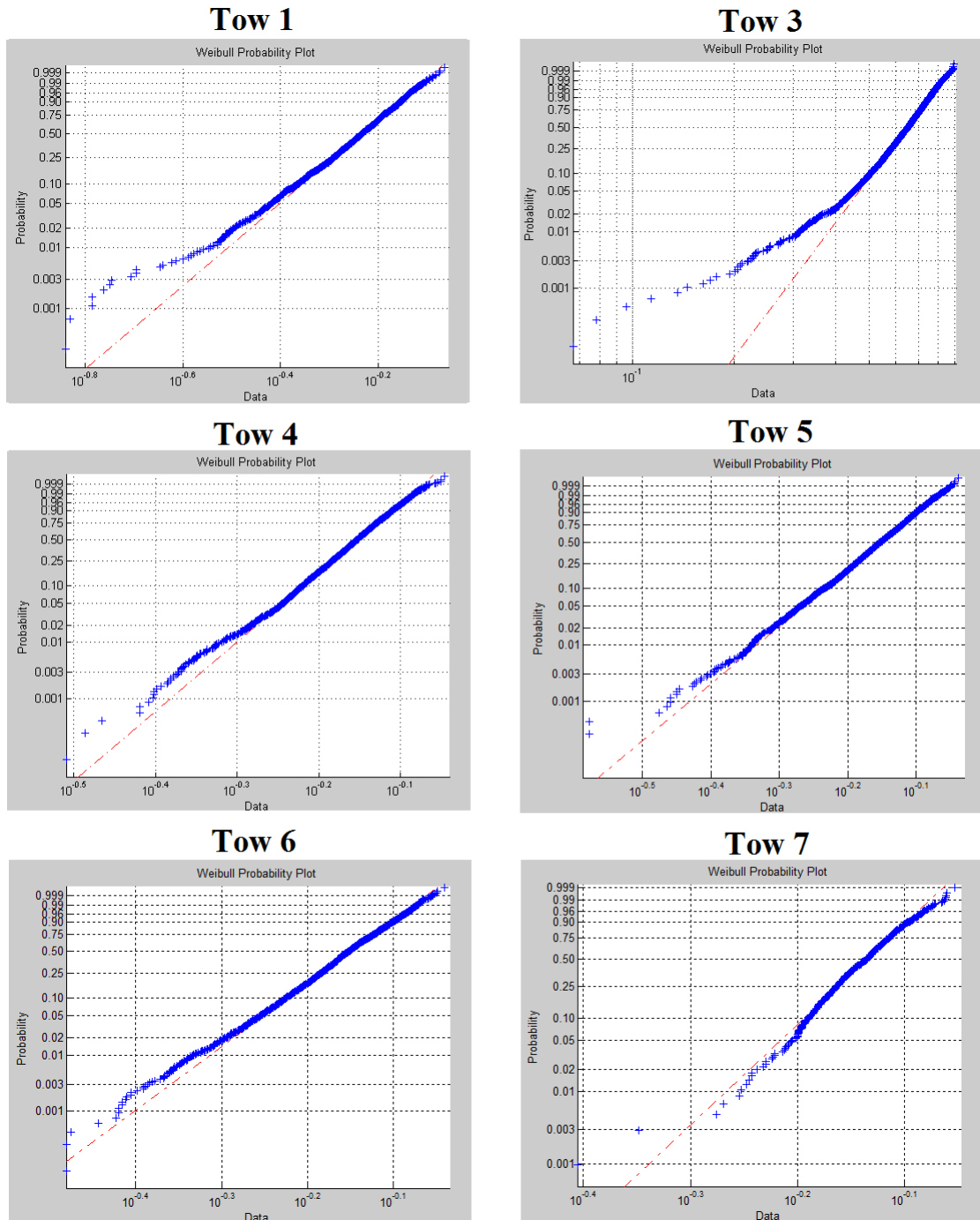


Figure 8.12: Weibull Probability Plots for Tows 1, 3, 4, 5, 6, and 7

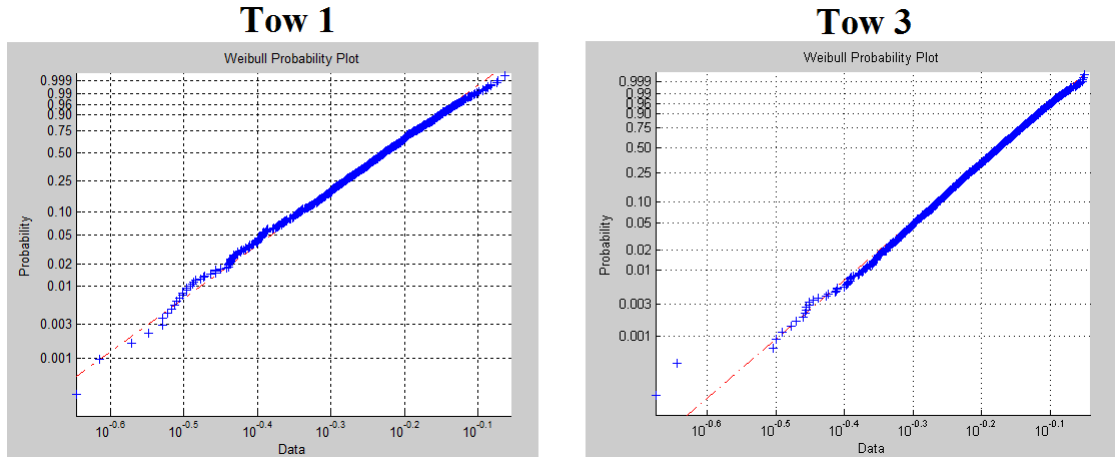


Figure 8.13: Weibull Probability Plots for Tows 1 and 3- Adjusted for Edge Effects

size of the fibers and the lower tow fiber density could have an effect on the fiber volume fraction distribution. This hypothesis is supported by the fact that all of the warp IM7 12k fiber tows appear to exhibit a Weibull distribution. Therefore, a higher fiber density coupled with a small fiber size could be indicative of a more consistent Weibull distribution.

It was also observed that some of the later images slices showed the edges of both Tows 1 and 3. It was hypothesized that these edges might have a lower fiber volume fraction that is inconsistent with the majority of the tow. Therefore, this inconsistency could lead to a distribution that is not indicative of the tow as a whole. To test this, new Weibull probability plots were generated for Tows 1 and 3 with all edge data eliminated. The cut-off image slices for Tows 1 and 3, the image slices where the edge of the tow first appeared, were the twelfth and sixteenth image slices, respectively. The results of this adjusted Weibull distribution test are shown in Figure 8.13. As can be seen from these adjusted plots, the data for both Tows 1 and 3 show a linear behavior about the line. This would seem to indicate that the edges of the tows skew the fiber volume fraction distribution of the overall tow due to the low fiber volume fractions in these regions. Fiber volume fraction variation in tows can therefore be modeled as approximately a Weibull distribution if the edge regions aren't

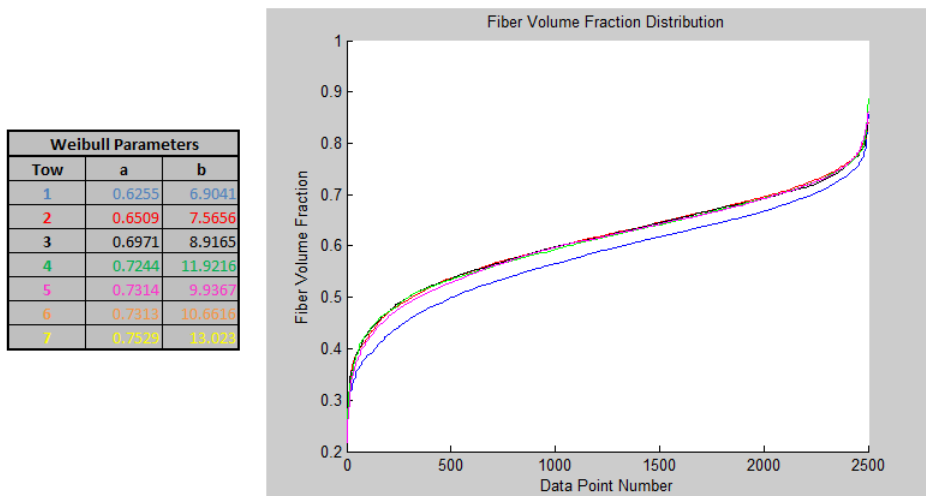


Figure 8.14: FVF Tows 1-7: Parameterized Weibull Distribution

considered. However, these results should be verified on additional image slices taken at a much higher resolution.

The shape of Weibull distributions vary greatly depending upon how the function is parameterized. The probability density function for a Weibull distribution is commonly written as Equation 8.1:

$$y = ba^{-b}x^{b-1}e^{-(\frac{x}{a})^b} \quad (8.1)$$

where x is a data point, y is the corresponding fiber volume fraction, a is the scale parameter, and b is the shape parameter. Using the *wblfit* command in MATLAB, the fiber volume fraction variation obtained from the serially sectioned images can be parameterized. With these parameters, the distribution can then be plotted by creating a random data set using the *wblrnd* command. The Weibull distribution scale and shape parameters and their corresponding plots are shown in Figure 8.14. As can be seen in this figure, the seven tows all exhibit a very consistent distribution shape. However, Tow 1 appears to be lower than the other tows. This was possibly due to the fact that this tow had the lowest amount of data collected after adjusting for edge effects. However, Tow 1's

shape is still consistent with the others; its mean fiber volume fraction is just lower than the other tows. This suggests that the fiber volume fraction distribution shape could remain approximately constant from tow to tow; adjustments simply need to be made to achieve a target fiber volume fraction mean.

CHAPTER IX

RECOMMENDATIONS AND CONCLUDING REMARKS

9.1 Recommended Research Plan

Unfortunately, at this time, full serial sectioning of the specimen has yet to be completed. Considering serial sectioning of the entire specimen required seven complete days, the Robo-Met 3D technician was unable to image the specimen for this study. In addition, it was determined that image processing and fiber volume fraction analysis would take approximately three weeks to conduct. Because of this, experimental verification of the modeling methodology was not obtained for this study. This section will thoroughly outline the recommended research plan to execute after serially sectioned data is obtained.

First, due to the extremely high resolution of each image slice, it is recommended that each image is cropped into smaller images so that the data is simpler to analyze. It was noted that at the recommended input parameters for the EM/MPM software, one entire image would take approximately 3.125 hours to segment. Meanwhile an image of a single tow using the same EM/MPM input parameters takes less than ten minutes to segment. It is therefore recommended that the images are batch cropped around individual tows using an image analysis tool such as FIJI. Figure 9.1 shows an example of a tow that has been batch cropped from the original image and then segmented. In addition to making it easier to obtain segmented images of individual tows, the batch cropping

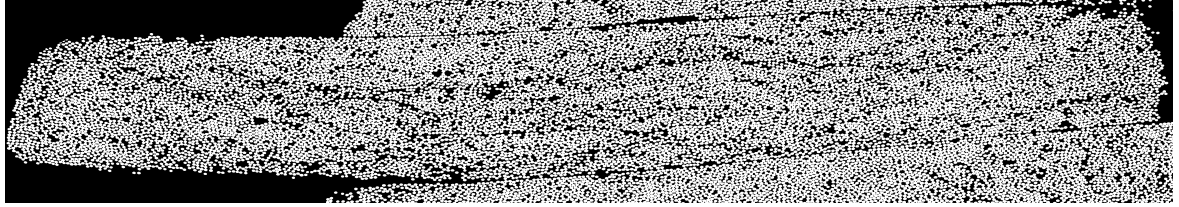


Figure 9.1: Batch Cropped and Segmented Tow

makes determining the bounding polygons in the tow cropping MATLAB algorithm a relatively trivial process.

After fiber volume fraction variation data is obtained for a tow, it is recommended that the data is applied to the model using both the direct relation and hierarchical Weibull fit redistribution methods discussed in Sections 7.3 and 7.4, respectively. Once these models are obtained, they can be compared to a model that exhibits no fiber volume fraction variation and to a model with FVF variation that has been generated exclusively in VTMS without any experimental data implemented. With these four models, a simple simulation should be run in BSAM with a small tensile load in the direction of the fibers. For this comparison to be accomplished, varying material data parameters must be implemented in BSAM. At present, BSAM assumes consistent material properties at every node and integration point in the tow. Varying properties have been implemented in an ABAQUS plug-in known as COMPRO. Using methods from COMPRO has shown promise for utilizing varying properties in a BSAM model.

Once varying properties are implemented within BSAM, the next challenge is to determine how to relate the fiber volume fraction variation to elastic properties. For this, the recommendations are as follows:

- E_1 Elastic Modulus-

$$E_1 = V_f E_f + (1 - V_f) E_m$$

- E_2 Transverse Elastic Modulus-

$$E_2 = (1 - \sqrt{v_f})E_m + \frac{\sqrt{v_f}E_mE_{f2}}{v_fE_m + \sqrt{v_f}(1 - \sqrt{v_f})E_{f2}}$$

- G_{12} In-Plane Shear Modulus-

$$G_{12} = \frac{G_f G_m}{V_m G_f + V_f G_m}$$

- ν_{12} Poisson Ratio-

$$\nu_{12} = \nu_m v_m + \nu_f v_f$$

Note that the parallel-series model was chosen for the E_2 model instead of the Tsai and Hahn equation; it was determined that the parallel-series model was desirable since a stress partitioning parameter was not necessary as it is in the Tsai and Hahn equation. Although all of these equations are not often used for 3D textile composites, they should theoretically be accurate if the definition of the local fiber orientations is also accurate. For orientation purposes, the orientation definition automatically generated by VTMS should suffice. However, it is recommended that in the future a more thorough study of orientation is conducted such that fiber volume fraction variation and orientations can be examined simultaneously.

At present, VTMS assigns a fiber volume fraction value at each node within the finite element mesh; this causes another issue worth noting. The algorithm within BSAM solves the given problem at the integration points of each element within the mesh. These integration points do not have the same coordinates as the nodal points. Therefore, since material properties are assigned to the nodal points, these properties would have to be interpolated to the integration points. Considering the close proximity of the nodal points to the integration points, there is likely not a large enough property difference to have a significant effect on the outcome; however, for greater accuracy, this is an issue that should be resolved.

9.2 Conclusion

A 3D textile polymer matrix composite was fabricated using a 3TEX eight layer orthogonal weave preform. Specimens were examined in a Zeiss XRM-530 X-ray micro-CT with in-situ loading. Micro-CT images were used to perform digital volume correlation utilizing Correlated Solutions software. Micro-CT images were deemed insufficient for the examination of fiber volume fraction variation in 3D PMC textiles. Preliminary serial sectioning was performed using Robo-Met 3D on a fabricated specimen to assess the viability of obtaining fiber volume fraction variation data from higher fidelity images. Analysis tools were developed using a binary pixel ratio algorithm to estimate local fiber volume fractions. Tools were also developed for examining fiber volume fraction in individual tows in each image slice. The adequacy of these tools was assessed and deemed acceptable for implementation in a computational model of the 3D textile PMC specimen.

Methodologies were shown for generating high fidelity and accurate models of 3D textile polymer matrix composites. The current process for computational fiber volume fraction in VTMS was examined and its accuracy was assessed. Techniques for implementing experimental fiber volume fraction variation data within the computational model were suggested. Although high fidelity serial sectioning data for the entire gage section of the specimen was not obtained given the time constraints, fiber volume fraction variation distribution tests were carried out on lower resolution images. Results from these tests suggested that the fiber volume fraction distribution could be represented by a Weibull distribution function if the edge regions of the tow were not considered. Furthermore, a thorough plan was laid out to be utilized upon acquisition of the high resolution data.

At this point, no determination can be made as to the effect fiber volume fraction variation has on damage evolution on 3D textile polymer matrix composites. However, this study succeeded in generating an effective means of examining this variation in serially sectioned images. Further

research must be conducted to observe the effects local fiber volume fraction has on 3D textile polymer matrix composites on both a computational and experimental level.

BIBLIOGRAPHY

- [1] R. M. Jones, *Mechanics of composite materials*. Crc Press, 1998.
- [2] M. El Messiry, “Theoretical analysis of natural fiber volume fraction of reinforced composites,” *Alexandria Engineering Journal*, vol. 52, no. 3, pp. 301–306, 2013.
- [3] C. Soutis, “Fibre reinforced composites in aircraft construction,” *Progress in Aerospace Sciences*, vol. 41, no. 2, pp. 143–151, 2005.
- [4] A. R. Horrocks and S. C. Anand, *Handbook of technical textiles*. Elsevier, 2000.
- [5] B. Griffiths, “Boeing sets pace for composite usage in large civil aircraft,” *High Performance Composites*, vol. 5, no. 1, 2005.
- [6] R. M. Jones, *Mechanics of composite materials*. Crc Press, 1998.
- [7] S. R. Hallett, W.-G. Jiang, B. Khan, and M. R. Wisnom, “Modelling the interaction between matrix cracks and delamination damage in scaled quasi-isotropic specimens,” *Composites Science and Technology*, vol. 68, no. 1, pp. 80–89, 2008.
- [8] D. Mollenhauer, E. V. Iarve, R. Kim, and B. Langley, “Examination of ply cracking in composite laminates with open holes: a moiré interferometric and numerical study,” *Composites Part A: Applied Science and Manufacturing*, vol. 37, no. 2, pp. 282–294, 2006.
- [9] F. Stig, “An introduction to the mechanics of 3d-woven fibre reinforced composites,” 2009.
- [10] L. Tong, A. P. Mouritz, and M. Bannister, *3D fibre reinforced polymer composites*. Elsevier, 2002.
- [11] W. Gu, H. Wu, S. Kampe, and G.-Q. Lu, “Volume fraction effects on interfacial adhesion strength of glass-fiber-reinforced polymer composites,” *Materials Science and Engineering: A*, vol. 277, no. 1, pp. 237–243, 2000.
- [12] F. Desplentere, S. V. Lomov, D. Woerdeman, I. Verpoest, M. Wevers, and A. Bogdanovich, “Micro-ct characterization of variability in 3d textile architecture,” *Composites Science and Technology*, vol. 65, no. 13, pp. 1920–1930, 2005.

- [13] F. Guo-dong, L. Jun, W. Yu, and W. Bao-lai, “The effect of yarn distortion on the mechanical properties of 3d four-directional braided composites,” *Composites Part A: Applied Science and Manufacturing*, vol. 40, no. 4, pp. 343–350, 2009.
- [14] A. Esnaola, I. Tena, J. Aurrekoetxea, I. Gallego, and I. Ulacia, “Effect of fibre volume fraction on energy absorption capabilities of e-glass/polyester automotive crash structures,” *Composites Part B: Engineering*, vol. 85, pp. 1–7, 2016.
- [15] Y. Xue, X. Zhong, L. Wang, Q. Fan, L. Zhu, B. Fan, H. Zhang, and H. Fu, “Effect of w volume fraction on dynamic mechanical behaviors of w fiber/zr-based bulk metallic glass composites,” *Materials Science and Engineering: A*, vol. 639, pp. 417–424, 2015.
- [16] W. Liu, L. Luo, S. Xu, and H. Zhao, “Effect of fiber volume fraction on crack propagation rate of ultra-high toughness cementitious composites,” *Engineering Fracture Mechanics*, vol. 124, pp. 52–63, 2014.
- [17] R. F. Gibson, *Principles of composite material mechanics*. McGraw-Hill, 1994.
- [18] C. A. Dostal and T. J. Reinhart, *Engineered materials handbook*. ASM International, 1987, vol. 2.
- [19] L. Warnet, *Composites Course 2008-2009, University of Twente, Eng. and Tech.*
- [20] S. W. Tsai, *Theory of composites design*. Think Composites Dayton, 1992.
- [21] I. Verpoest and S. V. Lomov, “Virtual textile composites software wisetex: Integration with micro-mechanical, permeability and structural analysis,” *Composites Science and Technology*, vol. 65, no. 15, pp. 2563–2574, 2005.
- [22] M. Sherburn, “Geometric and mechanical modelling of textiles,” Ph.D. dissertation, University of Nottingham, 2007.
- [23] X. Zeng, L. P. Brown, A. Endruweit, and A. C. Long, “Advanced geometry modelling of 3d woven reinforcements in polymer composites: processing and performance analysis,” 2012.
- [24] A. Long and L. Brown, “Modelling the geometry of textile reinforcements for composites: Texgen,” *Composite reinforcements for optimum performance. Cambridge: Woodhead Publishing Ltd*, pp. 239–64, 2011.
- [25] H. Lin, A. C. Long, M. Sherburn, and M. Clifford, “Modelling of mechanical behaviour for woven fabrics under combined loading,” *International Journal of material forming*, vol. 1, no. 1, pp. 899–902, 2008.
- [26] G. Zhou, X. Sun, and Y. Wang, “Multi-chain digital element analysis in textile mechanics,” *Composites science and Technology*, vol. 64, no. 2, pp. 239–244, 2004.
- [27] J.-L. Chaboche, “Continuum damage mechanics: Part ii damage growth, crack initiation, and crack growth,” *Journal of applied mechanics*, vol. 55, no. 1, pp. 65–72, 1988.

- [28] J. J. Crookston, S. Kari, N. A. Warrior, I. A. Jones, and A. C. Long, “3d textile composite mechanical properties prediction using automated fea of the unit cell,” in *Proc. of the 16th Int. Conf. on Composite Materials*, 2007, pp. 1–7.
- [29] H. J. Kim and C. C. Swan, “Voxel-based meshing and unit-cell analysis of textile composites,” *International Journal for Numerical Methods in Engineering*, vol. 56, no. 7, pp. 977–1006, 2003.
- [30] D. Goyal, J. D. Whitcomb, and J. Varghese, “Analysis of load flow and stress concentrations in textile composites,” in *International Conference on Composite Materials*, 2007, pp. 1–3.
- [31] S. V. Lomov, D. S. Ivanov, I. Verpoest, M. Zako, T. Kurashiki, H. Nakai, and S. Hirosawa, “Meso-fe modelling of textile composites: Road map, data flow and algorithms,” *Composites Science and Technology*, vol. 67, no. 9, pp. 1870–1891, 2007.
- [32] J. Whitcomb *et al.*, “Three-dimensional stress analysis of plain weave composites,” *Composite materials: Fatigue and fracture.*, vol. 3, pp. 417–438, 1991.
- [33] B. Cox, W. Carter, and N. Fleck, “A binary model of textile composites”, vol. 42, no. 10, pp. 3463 – 3479, 1994. [Online]. Available: <http://www.sciencedirect.com/science/article/pii/0956715194904790>
- [34] W.-G. Jiang, S. R. Hallett, and M. R. Wisnom, “Development of domain superposition technique for the modelling of woven fabric composites,” in *Mechanical response of composites*. Springer, 2008, pp. 281–291.
- [35] W. Jiang, C. Yu, Y. Zhang, X. Huo, and L. Yanb, “Domain superposition technique for free vibration analysis of textile composite structures.”
- [36] E. V. Iarve, D. H. Mollenhauer, E. G. Zhou, T. Breitzman, and T. J. Whitney, “Independent mesh method-based prediction of local and volume average fields in textile composites,” *Composites Part A: Applied Science and Manufacturing*, vol. 40, no. 12, pp. 1880–1890, 2009.
- [37] Y. Wang and X. Sun, “Digital-element simulation of textile processes,” *Composites science and technology*, vol. 61, no. 2, pp. 311–319, 2001.
- [38] ——, “Determining the geometry of textile preforms using finite element analysis,” in *PROCEEDINGS-AMERICAN SOCIETY FOR COMPOSITES*, 2000, pp. 485–492.
- [39] Y. Miao, E. Zhou, Y. Wang, and B. A. Cheeseman, “Mechanics of textile composites: Micro-geometry,” *Composites Science and Technology*, vol. 68, no. 7, pp. 1671–1678, 2008.
- [40] C. Przybyla, T. Godar, J. Simmons, M. Jackson, L. Zawada, and J. Pearce, “Statistical characterization of sic/sic ceramic matrix composites at the filament scale with bayesian segmentation hough transform feature extraction, and pair correlation statistics,” in *International SAMPE Technical Conference*, 2013, pp. 859–878.

- [41] M. L. Comer and E. J. Delp, “The em/mpm algorithm for segmentation of textured images: analysis and further experimental results,” *Image Processing, IEEE Transactions on*, vol. 9, no. 10, pp. 1731–1744, 2000.
- [42] M. Comer, C. A. Bouman, M. De Graef, and J. P. Simmons, “Bayesian methods for image segmentation,” *JOM Journal of the Minerals, Metals and Materials Society*, vol. 63, no. 7, pp. 55–57, 2011.
- [43] J. Simmons, P. Chuang, M. Comer, J. Spowart, M. Uchic, and M. De Graef, “Application and further development of advanced image processing algorithms for automated analysis of serial section image data,” *Modelling and Simulation in Materials Science and Engineering*, vol. 17, no. 2, p. 025002, 2009.
- [44] D. H. Ballard, “Generalizing the hough transform to detect arbitrary shapes,” *Pattern recognition*, vol. 13, no. 2, pp. 111–122, 1981.
- [45] P. V. Hough, “Method and means for recognizing complex patterns,” Tech. Rep., 1962.
- [46] J. E. Spowart, H. E. Mullens, and B. T. Puchala, “Collecting and analyzing microstructures in three dimensions: a fully automated approach,” *Jom*, vol. 55, no. 10, pp. 35–37, 2003.
- [47] J. Simmons, P. Chuang, M. Comer, J. Spowart, M. Uchic, and M. De Graef, “Application and further development of advanced image processing algorithms for automated analysis of serial section image data,” *Modelling and Simulation in Materials Science and Engineering*, vol. 17, no. 2, p. 025002, 2008.
- [48] J. E. Spowart, “The 3-d analysis of discontinuously reinforced aluminum composite microstructures,” *JOM*, vol. 58, no. 12, pp. 29–33, 2006.

APPENDICES

APPENDIX A

Fiber Volume Fraction Tow Extraction

```
%% Fiber Volume Fraction Tow Extraction
% Solomon Duning
% duningsl@udayton.edu
% University of Dayton
%
% The code thresholds an image to a binary black and white image. Total
% number of white pixels is summed and then utilized to determine the FVF
% of the image. FVF is also calculated on a tow basis. Locations of all
% FVF sampling is also saved.
clear all; close all; clc;

%% Define Input File Parameters

fig_name = 'MAT_132_S2'; %Main name of image sequence
delim = '-'; %delimiter for image sequence
fig_type = '.tif';
ntows = 1; %number of tows in image
nfig = 1; %number of images
%fig = ReadTowCrop([fig_name,'- TowCrop.txt']);
load([fig_name,'- TowCrop.mat'])

%% Define Window and Tolerance Parameters

window = 50;
tol = .99; %tolerance of what percent of the window must be within the
% cropped region

% if non-square window and varying movement is desired, manually alter
% these values

window = window - 1;
x_density = window; %determines how many pixels to move the window each step
```

```

y_density = window; %a lower value will increase the sample density

x_window = window; %the amount of pixels in the window
y_window = window;

for ii = 1:nfig
    for jj = 1:ntows
        %% Read and Threshold the Image

        I = imread([fig_name,delim,num2str(ii),fig_type]); %read file
        I = I(:,:,1);
        level = graythresh(I); %threshold image
        %imshow(I);
        BWI= im2bw(I,level);
        %fig(1).BWI = BWI; %adds black and white image data to structure

        %% Threshold and FVF Calculation

        xp = 1; %coordinates of start pixel
        xc = 1; %counter for FVF matrix
        FVF = zeros(floor(size(BWI,1)/(window+1)),...
            floor(size(BWI,2)/(window+1))); %preallocate for speed

        for kk = 1:floor(size(I,2)/(window+1))
            yp = 1;
            yc = 1;

            for mm = 1:floor(size(I,1)/(window+1))

                rect = [xp,yp,x_window,y_window];
                I2 = imcrop(BWI,rect); %crop image
                %The line below adds cropped image data to the structure.
                %This is saved so specific FVF values can be related back
                %to their corresponding image.
                fig(ii).I(mm,kk).BWimage = I2;
                %Fiber volume fraction calculation
                FVF(mm,kk) = sum(sum(I2))/ (size(I2,1)*size(I2,2));

                yp = yp + y_density;
                yc = yc + 1;
            end
            xp = xp + x_density;
            xc = xc + 1;
        end

        fig(ii).FVF = FVF; %adds FVF data to the structure
    end
end

```

```

%% Tow Extraction

ctrl_x = fig(ii).tow(jj).pos(:,1);
ctrl_y = fig(ii).tow(jj).pos(:,2);

tc = 1; %tow matrix counter
p_startx = 0; %starting pixel value

for kk = 1:size(FVF,1)
    p_starty = 0;
    for mm = 1:size(FVF,2)

        xpix = (p_startx):p_startx + x_window;
        ypix = (p_starty):p_starty + y_window;
        [XPIX, YPIX] = meshgrid(xpix,ypix);

        if sum(sum(inpolygon(XPIX,YPIX,ctrl_y,ctrl_x)))...
           < tol*(x_window*y_window)

            else
                fig(ii).tow(jj).FVF_tow(1:3,tc) = [FVF(kk,mm);kk;mm];
                %the kk and mm is added to show location of values
                %within the FVF matrix
                tc = tc+1;
            end
            p_starty = p_starty + y_density;
        end
        p_startx = p_startx + x_density;
    end
end
end

save([fig_name, ' Data'], 'fig')

```

APPENDIX B

Fiber Volume Fraction Variation Map

```
%% FVF Map
% Solomon Duning
% duningsl@udayton.edu
% University of Dayton
%
% This code thresholds an image to a binary black and white image. Total
% number of white pixels is summed and then utilized to determine the FVF
% of the image. A representation of the FVF of each window is then
% outputted as a colormapped image.
clear all; close all; clc;

%% Define Input File Parameters

fig_name = 'MAT_149_S2'; %Main name of image sequence
delim = '-'; %delimiter for image sequence
fig_type = '.tif';
ntows = 1; %number of tows in image
nfig = 1; %number of images
load([fig_name,' Data.mat'])

fig_num = 1;

%% Generate FVF Representation Image

FVF2 = 250*fig(fig_num).FVF;
FVF2 = round(FVF2);
image(FVF2);

title('Fiber Volume Fraction Intensity Map','FontSize',15)

%% Generate colormap and colorbar
```

```
colormap(hsv(250));
%colormap('gray');
colormap('jet');
axis off
axis equal
ax_label = [0.20;0.40;0.60;0.80;1.0];
colorbar('YTickLabel',{ax_label(1,:),ax_label(2,:),ax_label(3,:),
ax_label(4,:),ax_label(5,:)});
```

APPENDIX C

Image Tow Cropper

```
%% Image Sequence Tow Cropper
% Solomon Duning
% duningsl@udayton.edu
% University of Dayton
%
% The code is meant to semi automatically crop out tows from multiple images.
% Tows are first manually defined. These bounding polygons are saved and
% then adjustments to them are allowed on subsequent images. The vertexes
% of the bounding polygons are then saved to a MATLAB file that can be used
% for analysis of individual tows
clear all; close all; clc;

%% Add File Path

ex_path = 'D:\Towl_Segmented\' ;
addpath(ex_path);

%% Manually Defined Parameters

fig_name = 'T1_Seg'; %Main name of image sequence
delim = '_'; %delimiter for image sequence
start_num = 149;
fig_type = '.tif';
ntows = 1; %number of tows in image
nfig = 4; %number of images

%% Read in Picture
I = imread([fig_name,delim,num2str(start_num),fig_type]); %read file
I = I*255;
imshow(I);
fig_num = start_num + 1;
```

```

%% Manually Define Bounding Polygons
for ii = 1:ntows
    h(ii) = impoly(gca); %gca is a function that stands for get current axes.
    %gca is an acceptable hparent for the impoly function
end
menu('Press OK When Ready to Continue', 'OK');
for ii = 1:ntows
    fig(1).tow(ii).pos = getPosition(h(ii));
end

%% Adjust Polygons for Following Images

for ii = 2:nfig
    I = imread([fig_name,delim,num2str(fig_num),fig_type]);
    I = I*255;
    imshow(I)

    for jj = 1:ntows
        h(jj) = impoly(gca,fig(ii-1).tow(jj).pos);
    end
    menu('Press OK When Ready to Continue', 'OK');
    for jj = 1:ntows
        fig(ii).tow(jj).pos = getPosition(h(jj));
    end

    fig_num = fig_num + 1;
end

%% Save Data

save([ex_path,fig_name,'- TowCrop.mat'],'fig');

```

APPENDIX D

Hierarchical Weibull Fit VTMS Redistribution

```
%% Hierarchical Weibull Fit VTMS Redistribution
% Solomon Duning
% duningsl@udayton.edu
% University of Dayton
%
% This code redistributes VTMS fiber volume fraction to match an
% experimental Weibull fit. This will modify the FVF of a tow from
% an input file and create a new input file with the Weibull distribution.
% Weibull distribution is assigned based on VTMS FVF prediction
% (node with the highest FVF from VTMS prediction will receive the highest
% FVF from the Weibull distribution)
% At present, there can only be 1 tow in the input file.
clear all; close all; clc;

%% Load Experimental Data
load('3D Textile Flythru DataV5.mat') %loaded FVF Matlab variable

tow = 2; %the tow number (in the image) we are modifying
newc = 0;
oldc = 1;
for ii = 1:size(fig,2)
    newc = newc + size(fig(ii).tow(tow).FVF_tow(1,:),2);
    FVF(1,oldc:newc) = fig(ii).tow(tow).FVF_tow(1,:);
    oldc = newc + 1;
end

figure(1)
wblplot(FVF)

%figure(2)

EXP_FVF = sort(FVF,'ascend');
```

```

%plot(EXP_FVF,'r.')

%% Read VTMS Values
InputFile = 'test3.in';
fid = fopen(InputFile, 'r');

%% Find FVF values
search = '*ORIENTATION, name=Ori'; %line we are searching for
line = 'null'; %placeholder character string

while strcmp(line,search) == 0
    line = fgetl(fid);
end
position = ftell(fid); %save position for later use
ori = textscan(fid,'%f','delimiter','','');

for ii = 1:length(ori{1})/8
    VTMS_FVF(ii) = ori{1}(ii*8);
end
fclose(fid);

%% For a Weibull fit of data with random values

parmhat = wblfit(FVF);
R = wblrnd(parmhat(1),parmhat(2),size(VTMS_FVF,1),size(VTMS_FVF,2));
R = sort(R,'ascend');
figure(3)
wblplot(R)

%% Create New Values from Weibull Distribution

VTMS_FVF = VTMS_FVF';
VTMS_FVF(:,2) = [1:length(VTMS_FVF)];
VTMS_FVF = sortrows(VTMS_FVF,1);
VTMS_FVF(:,3) = R;
VTMS_FVF = sortrows(VTMS_FVF,2);

%% Write New Values into New Input File

copyfile(InputFile,[InputFile(1:end-3),'_WBL.in']); %create a new file
fid = fopen([InputFile(1:end-3),'_WBL.in'], 'r+'); %open new file
fseek(fid,position,'bof'); %Go to orientation position
%fprintf(fid,'This is a test to see if i am overwriting complete lines')
count = 1;
for ii = 1:length(ori{1,1})
    if floor((ii-1)/8) == (ii-1)/8

```

```

        fprintf(fid,'%i,\t',ori{1,1}(ii));
elseif floor(ii/8) == ii/8
    fprintf(fid,'%0.8f\r\n',VTMS_FVF(ii-7*count,3));
    count = count + 1;
else
    fprintf(fid,'%0.8f,\t',ori{1,1}(ii));
end

end

%%

position = ftell(fid); %position where nodes end
skip = 0;
while skip == 0
    skip = isempty(str2num(fgets(fid))); %skip extra data
end
B_data = fread(fid); % Data from the end of the file

rewind(fid); %rewind the file to the beginning
A_data = fread(fid,position); % Data from the beginning of the file
fclose(fid);
fid = fopen([InputFile(1:end-3),'_WBL.in'],'w');
fwrite(fid,[A_data;B_data]);

fclose(fid);

```